University of Stavanger

FACULTY OF SCIENCE AND TECHNOLOGY

MASTER'S THESIS

Study programme/specialisation: Petroleum Geoscience Engineering – Master's Degree Programme	Spring semester, 2020 Open
Author: Sylwia Wasilewska	…… (signature of author)
Supervisors: Wiktor Waldemar Weibull, Ivan Gutierrez	
Title of master's thesis: Acquisition, Processing and Interpretation of Ground Penetrating Radar (GPR) Data in Aidonia, Greece	
Credits: 30	
Keywords: Ground penetrating radar Geology Archaeology Near-surface geophysics Geological mapping	Number of pages: 90 + supplemental material/other: 32 Stavanger, 15.07.2020

Acquisition, Processing and Interpretation of Ground Penetrating Radar (GPR) Data in Aidonia, Greece

by

Sylwia Wasilewska

MSc Thesis

Presented to the Faculty of Science and Technology

The University of Stavanger

The University of Stavanger

July 2020

Abstract

Acquisition, Processing and Interpretation of Ground Penetrating Radar (GPR) Data in Aidonia, Greece

Sylwia Wasilewska, Master of Science degree (M.Sc.)

University of Stavanger, 2020

Supervisors: Wiktor Waldemar Weibull, Ivan Gutierrez

The Mycenaean Cemetery of Aidonia, Greece, is located about 10 km west of the town of New Nemea on the Peloponnese peninsula. In this cemetery, a number of chamber tombs dating from 1600-1100 B.C. was discovered in the late 1970s and excavated after many of the tombs were plundered by looters.

The Aidonia Cemetery is still being excavated today, but the area has not been thoroughly investigated geologically. This study uses ground penetrating radar (GPR) to investigate the shallow subsurface of the cemetery, as well as investigating any archaeological artefacts. In addition to GPR, geological field mapping was done correlate with the GPR data and ultimately provide a better understanding of the local geology in the cemetery and its vicinity.

In this study, a complete workflow that encompasses acquisition, processing, and interpretation of GPR data is provided. The final GPR dataset consisted of 89 lines in the Middle and Upper Cemetery, where nine areas (features) were interpreted in the data. In addition to this, over 400 small-scale faults in individual lines, and 33 wipeout zones were interpreted throughout the data. The main challenges in this study were the high absorption of electromagnetic waves in the GPR survey, as well as inaccurate GPS coordinates. A geological field map of the study area was created, with focus on the Aidonia Cemetery; it was found that four units with six different lithologies were observed in the study area.

It was found that wipeout zones could indicate a higher water saturation or an infill, both of either natural or anthropogenic origins. Some wipeouts correlated with already excavated tombs. Individual faults can possibly be combined and interpreted as fracture planes. Features can correlate to a harder, more consolidated lithology, as indicated on the geological map of the study area.

Future studies in this area would require an external GPS antenna and can be conducted with a higher-frequency GPR antenna for better resolution, as well as collection of samples to study the petrophysical properties of the rocks in the study area.

Acknowledgements

First, I would like to thank my supervisor, Wiktor Waldemar Weibull, for continued support during the process of working on this thesis. Without his tips and help, the work would have taken many times longer and would yield lower quality results.

I would like to thank my co-supervisor Ivan Gutierrez for inviting me to do this project, which is part of his PhD research, and allowing me to work on such a big part of it.

I would like to thank all the professors in the Institute of Energy Resources for guiding me over the five years I have been studying here, especially Alejandro Escalona for leading the department and being open to communication with us students.

A big thank you to Paul Nadeau, who inspired me to study geology all those years ago with the words, “Every rock has a story.”

Thank you to Andreas Habel for putting up with continuous emails from me about IT issues, that ended up being quickly resolvable thanks to his help, especially during home office work during the coronavirus quarantine.

Thank you to the University of Stavanger for providing the necessary equipment, software licenses, as well as financial support.

I would like to thank my classmates over these years, for discussions about different subjects and help during our studies.

I finally thank my friends and family, for continuous and unwavering support during the months of working on this thesis, as well as throughout my time studying. Without their constant support, I would not have been able to be where I am today.

Without the encouragement of countless people, the completion of this thesis would not have been possible. Their help and support are greatly appreciated.

Sylwia Wasilewska

Table of Contents

List of Figures

List of Tables

1 Introduction

1.1 Ground penetrating radar (GPR)

Non-destructive geophysical exploration methods are growing in popularity in several industries, including construction, ecology, archaeology, engineering, and more. One of the methods, ground penetrating radar (GPR), is widely used due to its availability and efficient acquisition. Modern GPR antennas are lightweight and small, and numerous companies create equipment that allows for immediate viewing and basic processing of data during or directly after acquisition.

GPR has its origin in the year 1910, only six years after the patent for the radar. Two German scientists, Gotthelf Leimbach and Heinrich Löwy, used electromagnetic (EM) waves to detect buried objects. They did this using buried dipole antennas, that were positioned in an array of vertical boreholes. The magnitude of signals received was compared, and using this method they were able to observe a crude image of the subsurface in the form of an area in which the EM signal was absorbed compared to surrounding areas (Gizzi and Leucci, 2018). This method used a continuous-wave radar, but in 1926 Hülsenbeck introduced the pulse radar, improving the depth resolution (Borchert, 2019).

The first recorded GPR survey conducted in the world was done by Austrian scientists in 1929, where GPR was used to determine the depth of a glacier (Gizzi and Leucci, 2018). This work demonstrated that EM waves can be transmitted in other media than air, but it did not receive much attention at the time. Until after the Second World War, GPR was not used even though traditional radar was used widely. Different uses of radar and GPR were published in the 1950s and 1960s (Steenson, 1951; Evans, 1963), where the main focus of using GPR was for investigating glaciers on Greenland and in polar regions (Annan, 2002). In the 1970s, the first commercial device was available on the market, and the use of GPR was also investigated in coal and other mineral deposits (Holser et al., 1972; Cook, 1976). In 1972, NASA built a prototype GPR antenna that was sent to the

Moon in the Apollo 17 mission to study geological and electrical properties of the Moon's crust (Annan, 2002; Gizzi and Leucci, 2018) (Figure 1.1).

Figure 1.1: The surface electrical properties experiment carried out on Apollo 17 used a 3-component vector receiver mounted on the lunar rover on a dual axis multi-frequency dipolar antenna laid out on the surface to sound the subsurface (from Annan, 2002).

In the late 1970s and early 1980s, the applications of the GPR increased as new technology became more readily available. It became widely used in archaeology (Dolphin et al., 1978), the mining industry, especially for coal (Coon et al., 1981), and more. These methods have been improved over time, at the same time as equipment bulkiness was decreased to allow for better accessibility and easier use. The integration of global positioning system (GPS) equipment has also allowed for higher accuracy of measurements and allows for positioning of subsurface reflections (Conyers, 2013). In the late 1990s to early 2000s, the evolution of computers had a significant impact on the development of GPR technology. This allowed for faster acquisition and processing of

data, especially 3D data that could now be used to make maps and grids for practical uses (Annan, 2002). In the late 1990s, ultra-shallow, high-resolution seismic has been compared to GPR data, but it was found that the comparison was only possible when a similar wavelength was achieved (Bachrach and Rickett, 1999).

Currently GPR is being used in many fields, including Earth sciences (Davis and Annan, 1989; Gizzi et al., 2010; Mustasaar et al., 2012; Booth et al., 2013; Leucci et al., 2017; Xie et al., 2018), archaeology (Goodman, 1994; Conyers, 2013; Zhao et al., 2013; GuidelineGeo, 2017), water management studies (Haaken et al., 2016; Anbazhagan et al., 2020; Yu et al., 2020), environmental engineering (Čermák et al., 2000; Huisman et al., 2003), civil engineering (Abouhamad et al., 2017; Dawood et al., 2020), and more.

GPR uses EM waves to create an image of the subsurface, the same way seismic imaging uses acoustic waves to create reflection profiles. GPR reflection profiles, or radargrams, have a higher resolution than seismograms, but they have a lower depth penetration, meaning that most GPR studies reach a depth of maximum tens of metres in the subsurface (GeoModel, 2014).

When an EM pulse is transmitted into the ground, the variations of electrical conductivity and dielectric permittivity of different minerals in the subsurface cause the energy to be reflected and refracted, similarly to acoustic seismic waves. Bedrock contact, groundwater level, mineralogy, organic-rich sediments, and changes in sediment grain size are all factors that can characterise the interface between layers in the subsurface. The rate of attenuation of energy passing through the subsurface can also be affected by a change in the dielectric constant (Jol, 2009). These subsurface layers are imaged similarly to seismic imaging, with a horizontal position and a two-way travel time.

To mathematically describe EM energy, one must utilise Maxwell's equations and constitutive relationships. Combining these sets the foundation for quantitative description of GPR signals (Jol, 2009).

Maxwell's equations are as follows:

$$\nabla \times \boldsymbol{e} = -\frac{\partial \boldsymbol{b}}{\partial t} \quad (1.1)$$

$$\nabla \times \boldsymbol{h} = \boldsymbol{j} + \frac{\partial \boldsymbol{d}}{\partial t} \quad (1.2)$$

$$\nabla \cdot \boldsymbol{d} = \rho \quad (1.3)$$

$$\nabla \cdot \boldsymbol{b} = 0 \quad (1.4)$$

Where:

- $\boldsymbol{e}$ = Electric field strength vector (V/m);
- $\boldsymbol{b}$ = Magnetic flux density vector (T);
- $\boldsymbol{d}$ = Electric displacement vector (C/m^2);
- $\boldsymbol{h}$ = Magnetic field intensity (A/m);
- $\boldsymbol{j}$ = Electric current density vector (A/m^2);
- ρ = Electric charge density (C/m^2); and
- t = Time (s).

Constitutive relationships are used to quantify material properties, and here will be used to relate material physics to EM energy. Three quantities are necessary for understanding GPR:

Electrical conductivity $\tilde{\sigma}$, dielectric permittivity $\tilde{\varepsilon}$, and magnetic permeability $\tilde{\mu}$.

$$\boldsymbol{j} = \tilde{\sigma}\boldsymbol{e} \quad (1.5)$$

$$\boldsymbol{d} = \tilde{\varepsilon}\boldsymbol{e} \quad (1.6)$$

$$\boldsymbol{b} = \tilde{\mu}\boldsymbol{h} \quad (1.7)$$

Electrical conductivity describes how a current is formed by free charges when an electric field is present. Dielectric permittivity describes how, in an electric field, constrained charges are displaced. Magnetic permeability describes how, in the presence of a magnetic field, intrinsic molecular and atomic magnetic moments respond (Karczewski et al., 2011).

These three quantities are tensors, often non-linear, but in relation to GPR they are treated as scalars. This means that the response is independent of field strength and in the same direction as the existing field (Annan, 2005; Karczewski et al., 2011).

There are some assumptions that must be made to use the Maxwell equations in GPR interpretation and modelling: 1) the medium must be infinite; the medium must be linear, isotropic, and homogeneous; 2) the medium must be lossy (when $\tilde{\sigma} > 0$); and 3) the medium does not create any electric or magnetic currents. Not all geological media fit these assumptions, the subsurface is simplified to fit these assumptions (Karczewski et al., 2011). It is possible to solve Maxwell's equations for anisotropic, heterogeneous media with dielectric permittivity and magnetic permeability, but one must know the parameters for each tensor; these parameters are generally not known, which is often why the assumptions are made.

The spread and attenuation of electromagnetic fields in a geological medium is controlled by how electromagnetic fields interact with natural materials. Electrical displacement properties are dominant over conductive properties in most geological media, which means that radar velocity (v) can be approximated as:

$$v = \frac{c}{\sqrt{K}} = s^{-1} \qquad (1.8)$$

Where:

c = Speed of light in air (0.3 m/ns);

K = The rock's dielectric constant; and

s = Slowness, the reciprocal of velocity (Fisher et al., 1996).

Whether electrical displacement properties are dominant over conductive properties is dependent on the magnitude of the conductivity, frequency, and dielectric permittivity. If the product of the frequency and dielectric permittivity is much larger than the conductivity, only then can the conduction currents be neglected in favour of

displacement currents. GPR works with relatively high frequencies, which means it is possible to neglect conduction currents in most geological media.

The variation of physical properties generates the subsurface reflections acquired by GPR technology (Annan, 2005). Most materials are a combination of components from other materials, so it is crucial to understand physical properties of combined materials to interpret a GPR response (Jol, 2009). Ice and water are examples of the exception, where primarily a single component is present.

Radar-wave velocity is primarily affected by pore fluid velocities and rock matrix porosity (Φ). Most geological materials are assumed to have the same matrix velocity. A summary of relative permittivity and conductivity for common materials encountered during GPR surveys can be found in Table 1. In this table, K is the relative dielectric constant, σ is the electrical conductivity (mS/m), v is the velocity (m/ns), and a is the attenuation (dB/m). The presence of water affects the behaviour of the geological medium (Fisher et al., 1996).

Table 1: A list of common geological materials and their typical relative permittivity (K), electrical conductivity (σ), velocity (v), and attenuation (a) (from Fisher et al., 1996).

Material	K	σ (mS/m)	v (m/ns)	a (dB/m)
Air	1	0	0.30	0
Distilled water	80	0.01	0.033	2×10^{-3}
Fresh water	80	0.5	0.033	0.1
Sea water	80	3000	0.01	10^{3}
Dry sand	3-5	0.01	0.15	0.01
Saturated sand	20-30	1-10	0.06	0.03-0.3
Limestone	4-8	0.5-2	0.12	0.4-1
Shale	5-15	1-100	0.09	1-100
Silts	5-30	1-100	0.07	1-100
Clay	5-40	2-1000	0.06	1-300
Granite	4-6	0.01-1	0.13	0.01-1
Dry salt	5-6	0.01-1	0.13	0.01-1
Ice	3-4	0.01	0.16	0.01

From the values in Table 1, it is possible to deduce that aggregates and bulk minerals in mixtures are generally good dielectric insulators with a relative permittivity in the range of 3 to 8. They are also usually insulating and have almost no conductivity. As water is the most polarizable naturally occurring material, water conductivity is the dominant factor in determining bulk material conductivity due to the frequent presence of water in pore space (Annan, 2005).

The interpretation technique used in radargrams is usually the same as in seismograms, which is by use of interface mapping and horizon interpretation. If the radargram has preserved amplitude fidelity, it is possible to identify zones of high attenuation, which indicates areas of high conductivity that can be produced by the accumulation of clay (Kearey, 2002). However, this does not mean that every band of a radargram is a different lithology and interpreting as such would be incorrect. Multiples and other interference from previously reflected waves can cause disruptive noise in the radargram. Deconvolution as a processing technique allows for easier differentiation of primary events, which makes interpretation of these simpler. Migration is another processing technique that usually removes diffraction hyperbolae and restores correct dips (Kearey, 2002). An example of migration is the Kirchhoff migration, which is also called diffraction stack. This type of migration treats every point as a diffractor and calculates its amplitude using Kirchhoff summation (Robein, 2010).

1.2 Study area

The study area is located in and around the Mycenaean Cemetery of Aidonia in Greece. It is located in the Nemea Valley, approximately 10 km west of the town of New Nemea, in the Peloponnese Peninsula. The cemetery was discovered in an olive grove on the outskirts of the village of Aidonia in the mid-1970s. The study area can be seen in Figure 1.2.

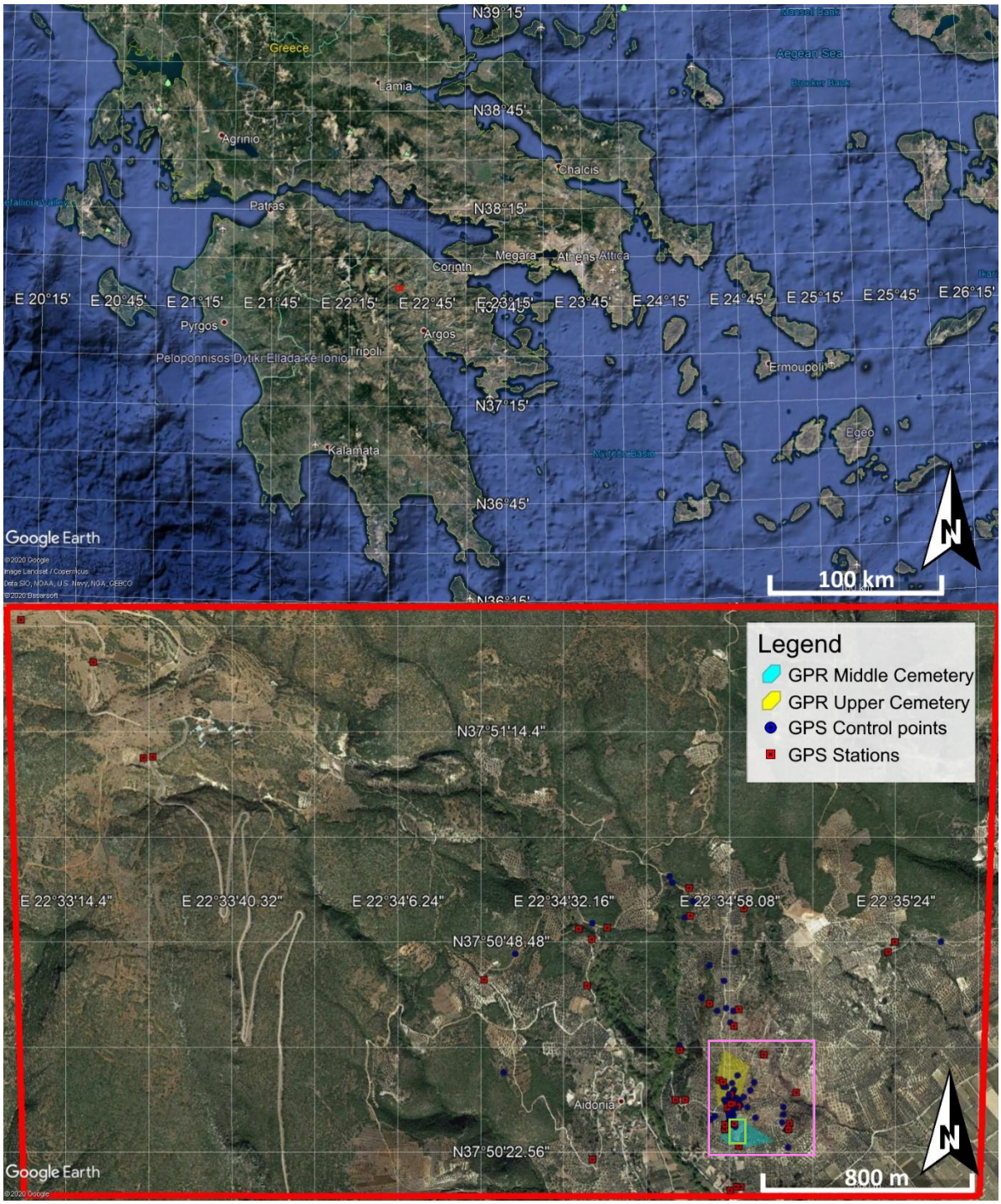

Figure 1.2: The study area. Satellite imagery from Google Earth, 2013.

1.2.1 Archaeology

The Mycenaean Cemetery of Aidonia in Greece consists of several tombs from approximately 1600-1100 B.C. As of 2014 there have been 151 features discovered (Shelton, personal communication), of which a number of features was credited to looters that invaded the area in the 1970s and 1980s. After looting first happened in the winter of 1976-1977, Dr Stephen G. Miller of the University of California at Berkeley conducted a rescue excavation in 1978-1980 (Archaeology Wiki, 2019). When Dr Stephen G. Miller first excavated the cemetery in 1978-1980, his team discovered 20 tombs, 18 of which were plundered by looters (GTP Headlines, 2019).

His work is being continued by Dr Kim Shelton of the University of California at Berkeley, who has conducted four seasons of excavation work in the area (Archaeology Wiki, 2019). Since Dr Kim Shelton took over the project in 2014, there have been features such as quarries discovered in the area, indicating that the bedrock in the area was strong enough to use for construction purposes. Dr Shelton's team has made multiple new discoveries in the cemetery in recent years (Chrysopoulos, 2018; Archaeology Wiki, 2019; GTP Headlines, 2019).

The cemetery is divided into three areas on a hillside: the Middle Cemetery was the first to be discovered (Figure 1.3); the Upper Cemetery, located upslope from the Middle cemetery; and the Lower Cemetery, located downslope from the Middle cemetery and very close to the modern village of Aidonia. The greatest concentration of tombs and other mortuary features is located in the Middle Cemetery, where new discoveries from 2018 and 2019 took place. The aerial photo in Figure 1.4 shows part of the Middle Cemetery, including the newly discovered tombs.

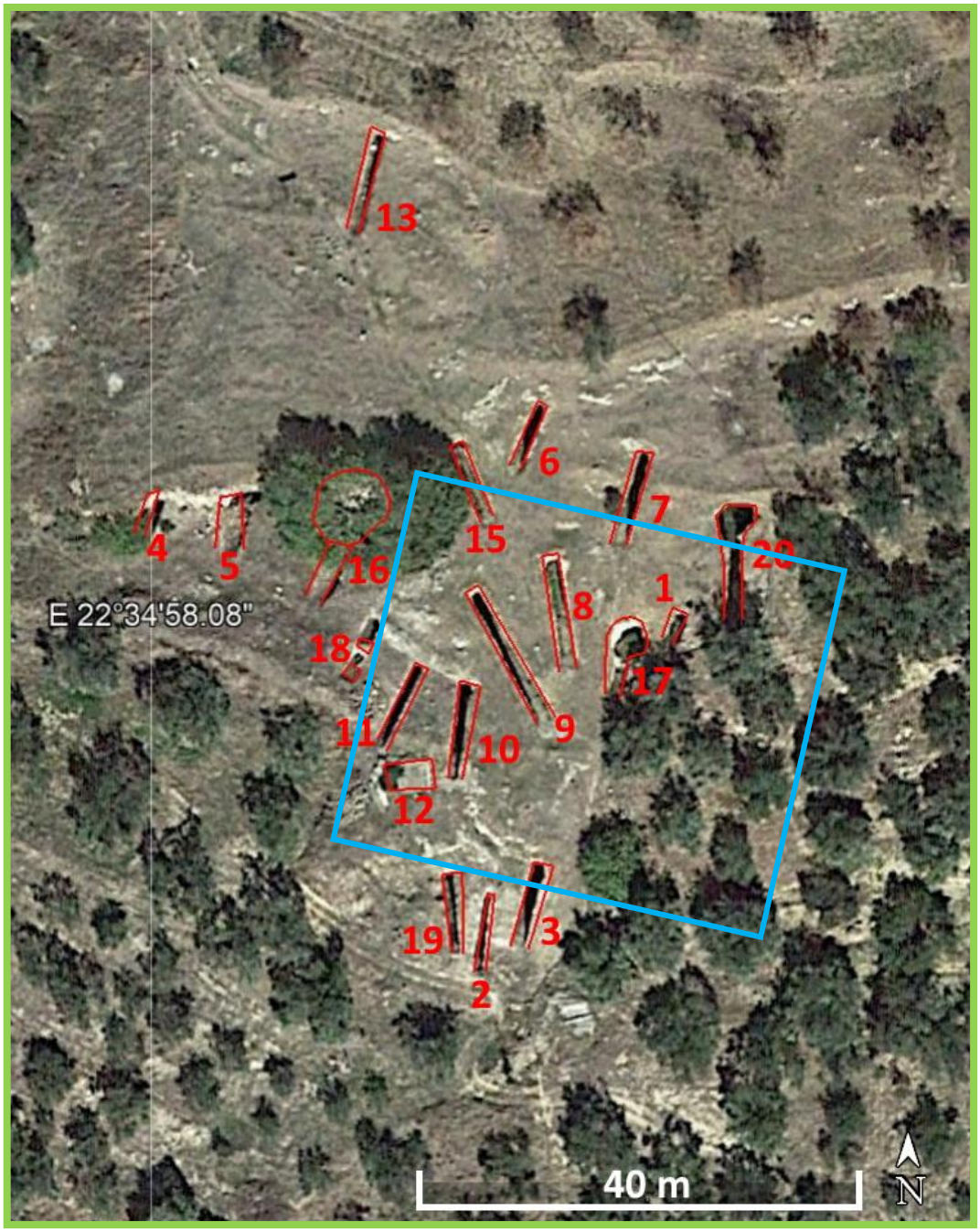

Figure 1.3: Location of the tombs in the Middle Cemetery. Satellite imagery from Google Earth, 2013.

Figure 1.4: An aerial photo showing part of the Middle Cemetery in the Mycenaean Cemetery of Aidonia, including the newest discoveries from 2018 (red, backfilled) and 2019 (yellow, excavated) (from ArchaeologyWiki, 2019).

The tombs found in the Mycenaean Cemetery of Aidonia are predominantly chamber tombs, that consist of three sections: a narrow passageway called the dromos; the entryway, called the stomion; and the burial chamber (Karkanas et al., 2012) (Figure 1.5). The top of the roof of the chamber tombs tends to be at least a metre below the surface, when not collapsed. In the western part of the cemetery, it is possible to observe multiple intact tombs, while in the eastern part of the cemetery, almost all chamber tombs have collapsed. This could be caused by illegal looters digging carelessly while plundering, geological reasons like tectonic activity or a softer facies, or the olive grove planted in the area.

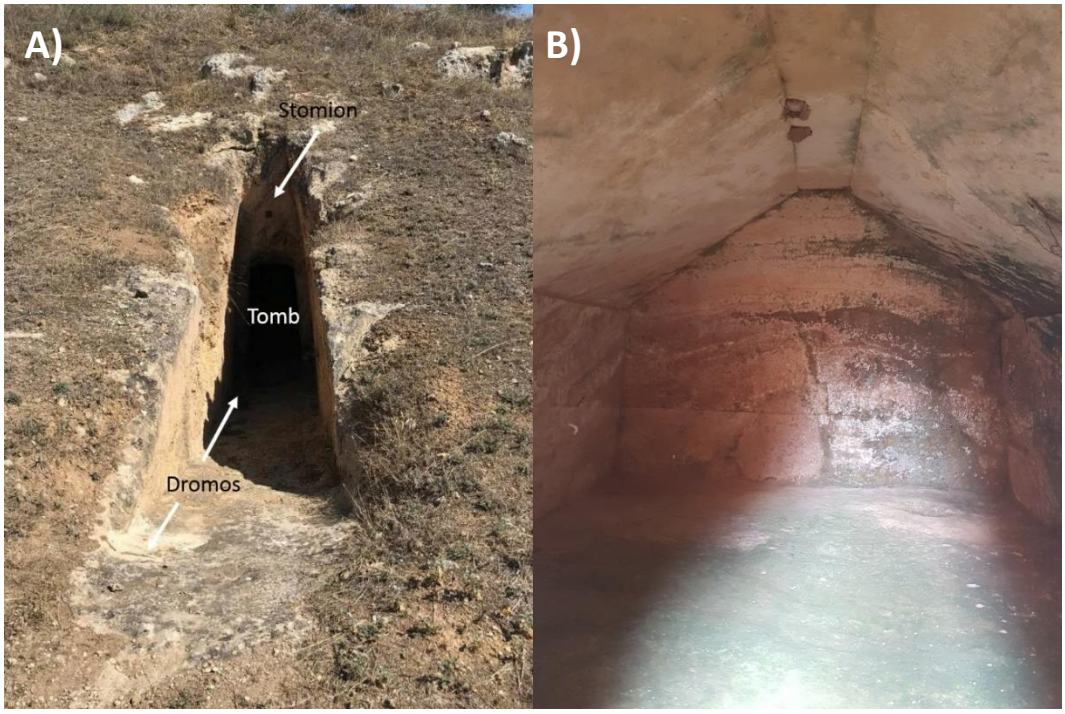

Figure 1.5: photos of A) the dromos and stomion from outside, and B) the interior of a well preserved chamber.

1.2.2 Geology

The study area has not been studied in detail geologically, so there is limited information about this geology. Gawthorpe et al. (2018) studied the evolution of the Corinth Rift, which is a regional scale study. Tataris et al. (1970) created a series of geological maps of Greece with the scale 1:50 000, one of which encompasses the study area and the surrounding areas. Paraskevopoulos (1990) investigated the sedimentology between two local towns, encompassing the study area of this project.

The geological units where the tombs were dug were deposited in a marginal onshore area of the active Corinth Rift. The rifting started between 5.0-3.6 Ma and currently the extension rate can reach up to 15 mm per year (Gawthorpe et al., 2018). The rifting causes faulting and fracturing in the area, normal faults being most common. Faults can vary in size, from km to cm scale. The study area is located in the Trikala-Kefalari fault block,

where the estimated maximum throw is >3 km (Gawthorpe et al., 2018). The beds in this fault block dip southwards towards the major Kyllini-Trikala-Kefalari fault, and consist of a thick succession of marlstones, siltstones, sandstones and conglomerates called the Rethi-Dendro Formation and Riza Member (Gawthorpe et al., 2018). The Rethi-Dendro Formation is of Plio-Pleistocene age and is possibly over 3 km thick in this fault block where the facies alternate repeatedly (Gawthorpe et al., 2018).

Closer to the study area, the dominating facies are calcareous conglomerates and marly limestones, as seen in the geological map by Tataris et al. (1970) (Figure 1.6). This geological map shows that there are older rocks, from Eocene to Jurassic age, to the south of the study area, as well as Quaternary infill in the Nemea Valley. In 1990, Paraskevopoulos (1990) studied the sedimentology of the Argolis basin, in the area between Stymfalia and Nemea. In this work, several formations were documented, including the Psari and Kefalari formations. These formations can be correlated with the Rethi-Dendro Formation reported by Gawthorpe et al. (2018). The Psari Formation is located in the study area and consists of three calcareous members: Member A, Member B, and Member C. This formation has a depositional environment between fluvial-lacustrine and alluvial, indicating some uplift that may have been caused by the rifting in the Gulf of Corinth, i.e. rift-flank uplift (Gawthorpe et al., 2018). The stratigraphic framework from Paraskevopoulos (1990) is more relevant and will be used in this project.

Member A mostly consists of a clast-supported, well cemented conglomerate with poor sorting and angular clasts with a size up to 50 cm. The member is between 500-700 m thick and is in direct as well as fault contact with Member B (Paraskevopoulos et al., 1990). Member B is an approximately 600 m thick package consisting of an alternation between conglomeratic and marly packages with a fining-upwards trend; there are conglomeratic packages with different directions of gradation that are more concentrated lower in the member. The thickness of these conglomeratic packages varies between <50-80 cm and are poorly to moderately poorly sorted, with sub-angular to sub-rounded clasts and different degrees of cementation; clasts vary in size between on average <0.5-12 cm, and

in some cases there are lenses of calcareous, fine- to medium-grained sandstone. The conglomerates also vary between clast-supported and matrix-supported and often are overlain by a thin layer of calcareous sandstone (Paraskevopoulos et al., 1990). The marl makes up approximately 66 % of the member and consists mostly of fine calcareous materials with occasional silt and sand grain size. The marly packages can reach a thickness of 4 metres and show plane-parallel lamination at the top and bottom of each package. There are occasional rudite interbeddings up to 3 cm thick with clasts of up to 0.5 cm size. The grain size of the marl increases to sand when close to a contact with conglomerate (Paraskevopoulos et al., 1990). Member C is the smallest member of the Psari formation, with an estimated thickness of 400-500 m, with the thickness decreasing to 100-150 m locally. This member consists of a conglomerate that varies between clast-supported and matrix-supported and is poorly cemented and moderately to poorly sorted. The thickness of individual layers within this member is on average 50-60 cm, with the size of clasts varying between 0.5-15 cm. The clasts are rounded, flattened, and show a similar orientation. There are interbeddings of finer, marly material that decrease towards the top of the member, and contacts between these contain medium-grained sandstone of up to 40 cm thickness (Paraskevopoulos et al., 1990).

As seen on the geological map in Figure 1.6, it is possible to see that there is a collection of faults in and around the study area (Tataris et al., 1970). The faults mostly strike northwest-southeast, which correlates to the faulting in the Gulf of Corinth (Gawthorpe et al., 2018). Because of tectonic activity, it is highly likely that both smaller scale faults and joints, meaning cracks in the subsurface with no offset, are present in the study area.

From Paraskevopoulos (1990), it is possible to determine that the study area is located only on the Psari Formation, as well as some Quaternary infill in the valley. The majority of the study area is located on Member B, including the Mycenaean Cemetery of Aidonia, while some more distant areas are located on members A and C (Figure 1.7).

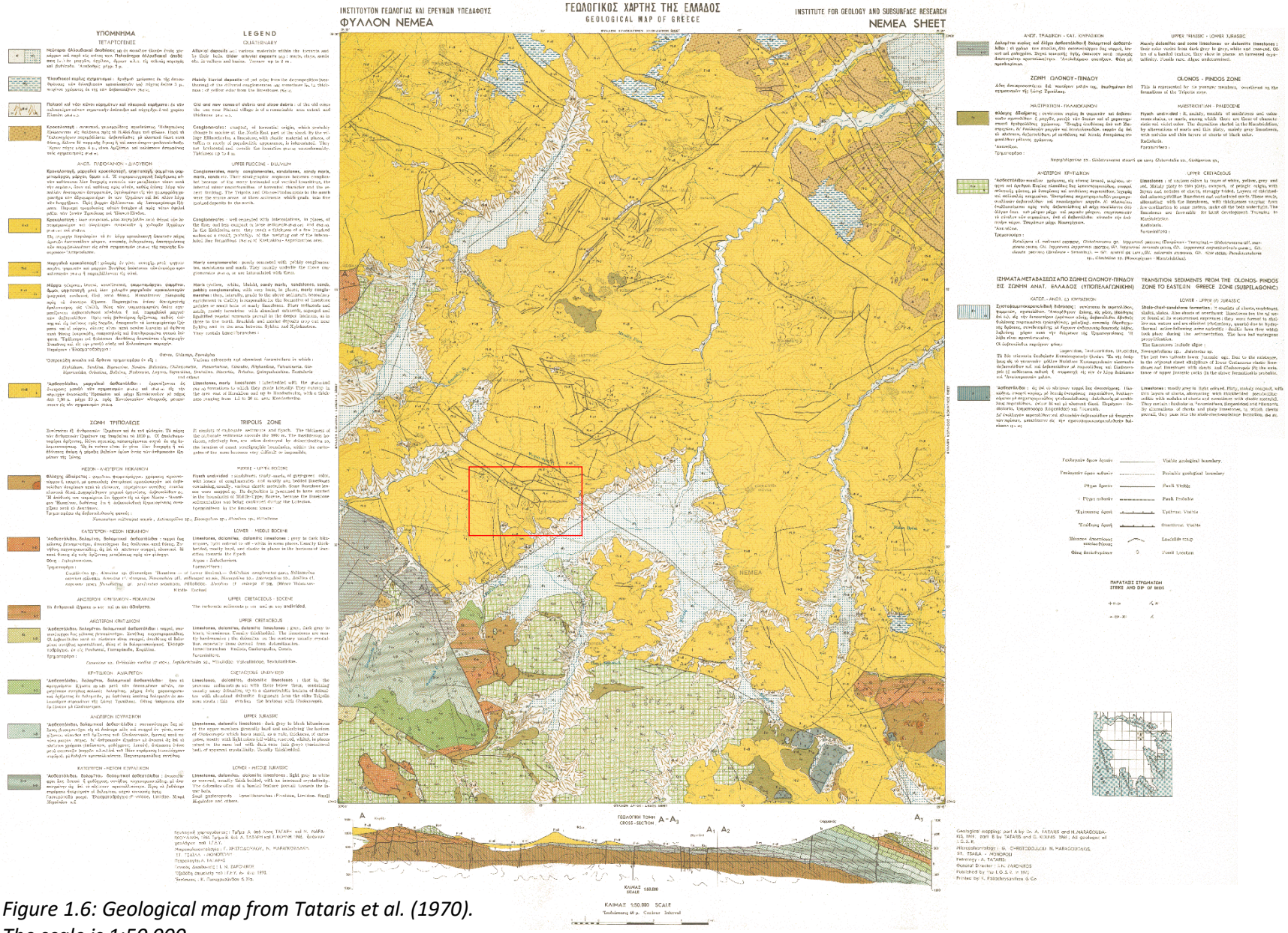

Figure 1.6: Geological map from Tataris et al. (1970). The scale is 1:50 000.

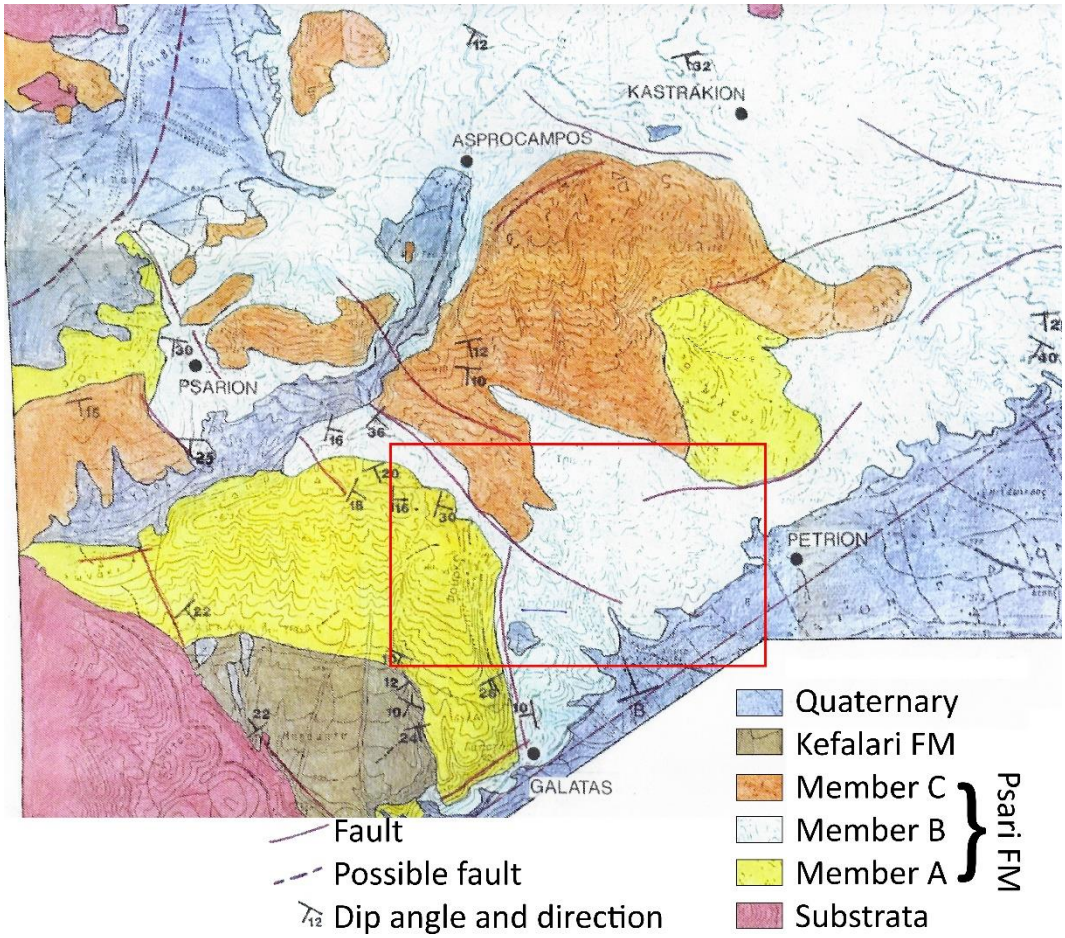

Figure 1.7: Part of a geological map from the thesis from Paraskevopoulos et al. (1990).

1.3 Previous work

There is no recorded work similar to this project in the Mycenaean Cemetery of Aidonia. There is however a mention of a GPR study being used in the exploration and excavation of the Mycenaean Cemetery Ayia Sotira, also located in the Nemea Valley (Smith et al., 2017). Few details are provided about the GPR survey, which does not allow for any insight on the topic.

GPR is a popular tool for archaeological exploration. In many cases, it is used to investigate the buried structures of archaeological finds, like in the ancient Roman town of Aquileia in north-eastern Italy, as described in Zhao et al., 2013. Here, it was known that ruins of

several buildings were buried under a layer of sediments not exceeding 4 m, and GPR was used to provide more information on the buried buildings.

Goodman (1994) describes a successful application of GPR to study burial mounds in Japan. These structures are protected by the Japanese cultural laws and cannot be excavated, a non-destructive exploration method like the GPR is extremely valuable to learn about different burial types and coffin structures in the protected burial mounds.

Ancient Ephesos, which lies in present day Turkey, was investigated using the GPR in the late 1990s (Hruska and Fuchs, 1999). They used GPR for two specific tasks: locating the continuation of a procession road to the temple of Artemis, and mapping the Hellenistic level of the Tetragonos agora, which is beneath the Roman level and not possible to fully excavate. Locating and interconnecting existing parts of the procession road were a success and confirmed by two boreholes, while GPR made it possible to map out remains of Hellenistic buildings as well as discovering previously undiscovered Roman ruins and even older human presence.

A combination of GPR, Lidar, and infrared thermography was used to reconstruct the ancient Roman Site called “Aquis Querquennis” in Bande, Spain (Puente et al., 2018). In this study, GPR was used to detect buried structures of barracks, which was then combined with the surface model created using Lidar, allowing for a reconstruction of the site both above and below the surface. Infrared thermography was then used to inspect the condition of structures and determine whether they were original or subsequent constructions.

GPR is often used in geosciences and has many different uses within this field. An example is a master’s thesis written at the University of Stavanger (Alcantara Rodriguez, 2018). In her thesis Alcantara Rodriguez investigated glacial deposits in Jæren, Norway using GPR and seismic and compared her results to create an interpretation of the glacial deposits and basement rocks.

Mustasaar et al. (2012) investigated GPR responses compared to petrophysical properties. The study area was in Võhmuta limestone quarry in Estonia, where they acquired GPR data and cores for petrophysical testing. Using hyperbola fitting, wide angle reflection and refraction, and topographic methods, a time-depth conversion was implemented to the GPR data. The study resulted in confirming that the strongest reflectors appear in the levels where changes in porosity occur.

1.4 Objectives and approach

The area of interest in this project has not been studied in detail geologically in the past, other than through regional studies. There is also a lack of outcrops that would allow geological measurements of, for example, dip and dip direction. GPR, being a non-invasive exploration method, can give insight into the structure of the subsurface, as well as possibly detect undiscovered tombs.

This study aims to provide understanding into the process of interpreting and modelling chamber tombs in the Aidonia Cemetery from GPR data. It also aims to provide some information on the shallow geology of the study area and compare whether the data collected using GPR correlates to geological data collected through conventional field methods. The area is rich in archaeological finds that can be difficult to discover using conventional methods, for which using GPR can greatly shorten exploration time. Because the area is tectonically active, it is also possible to find any faulting or fractures in the subsurface that could indicate the reason for the collapse of tombs, as well as differentiating between facies of different hardness and composition.

The main objective is to implement a workflow based on the use of GPR to study the subsurface of the Aidonia Cemetery and distinguish shallow geological features versus archaeological artefacts. This will be done by integrating and analysing the data collected using GPR and geological field mapping. This includes GPR data acquisition, processing, and interpretation, as well as the compilation of geological field data into a geological map of the area. Originally, there was equal weight put on geological field data and GPR

data in this study, but it was changed to focus more on the GPR aspect of the study and compliment the findings using geological data. The focus was changed due to time constraints and worse working conditions caused by the Covid-19 pandemic.

Another objective is to observe any possible artefacts in the data and investigate if these could be undiscovered archaeological artefacts that could be investigated in the future. The following tasks must be completed to accomplish the objectives:

- Collect sufficient GPR and geological field data;
- Process and interpret the GPR data;
- Thoroughly analyse results and compare to geological field data; and
- Observe any artefacts.

2 Methodology

This section will discuss the methodology of data collection, processing, and interpretation of both geological field mapping and GPR data. The geological field mapping data collection used conventional methods to gather information about the local geology in and around the cemetery, while the GPR dataset was collected in the Middle and Upper Cemetery, where the focus was tomb characterisation and further exploration of the cemetery. The GPR data was processed in MATLAB. Then, processed data was imported into Petrel where finally the GPR lines were interpreted. ArcMap was used to create a geological field map, courtesy of Ivan Gutierrez. A workflow of the GPR methodology can be seen in Figure 2.1.

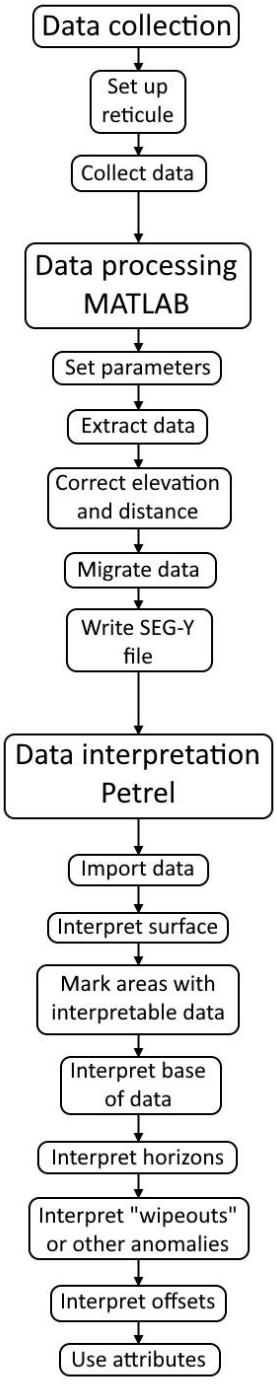

Figure 1.1: Workflow of the methodology used for the GPR survey in this project.

2.1 Geological field mapping

Collection of geological field data was done between 02.08.2019-17.08.2019 in the areas shown in Figure 1.2. The data collected consisted lithological descriptions and structural measurements (dip and dip direction), as well as any contacts that are outcropping in the study area. The geological data was acquired as stations and control points marked using a handheld GPS. Due to a poor exposition of the rock sequence in the cemetery, outcrops farther away were visited to recognise a greater exposition of facies, which reveals more of the geological setting of the area. A greater concentration of stations and control points was collected around the Aidonia Cemetery, to ensure accurate contacts between facies. A total of 36 stations and 65 control points were collected in the area (Figure 1.2). Stations are data points where a new facies has been found, a contact is discovered, or where in-depth information is collected. Control points, on the other hand, are data points where an already known facies or contact is seen and marked on the map for orientation. The georeferenced geological data was input into a GIS software to create a geological map of the area.

2.2 GPR survey

2.2.1 Equipment

The equipment used in this survey consists of a MALÅ GroundExplorer 80 HDR antenna with an encoder wheel attached to measure distance, a built-in GPS, and a connected portable computer. The antenna emits EM waves at a frequency of 80 MHz, and the penetration depth is 40 m in ideal conditions and a velocity of 100 m/µs (GuidelineGeo, 2016). The GPR data was collected with one person pulling or pushing the antenna, depending on the terrain, while another person carried the portable computer and controlled the data collected; however, the equipment is made in a way to allow for a single person to pull the antenna and carry the computer simultaneously. The equipment can be seen in Figure 2.2.

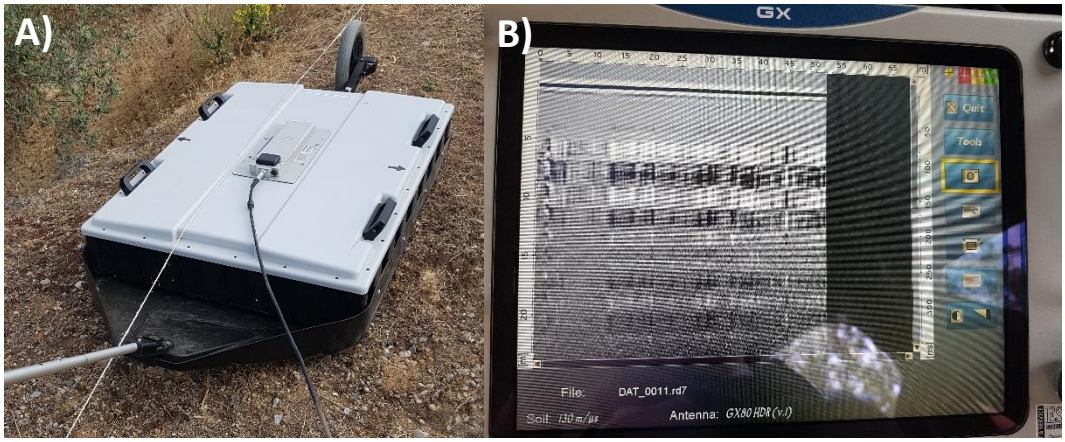

Figure 2.2: Photos of the equipment. A) shows the antenna mounted on the slide with the encoder wheel attached. B) shows the screen of the portable computer that is attached to the antenna.

2.2.2 Data collection

GPR data was collected between 04.08.2019-07.08.2019 and on 11.08.2019. Data was gathered in the Middle Cemetery (04-07.08-2019) and the Upper Cemetery and surrounding areas (11.08.2019) (Figure 1.2). The study area was first examined, and test scans were conducted both on soily ground and outcropping rock on 03.08.2019. The result of these tests showed that the absorption of the radar waves was very high in soil,

to the point where the only data collected was the direct wave. The tests conducted on consolidated rock yielded more data, which was promising for the remainder of the GPR survey. However, the penetration depth was still very shallow (max. 8 metres), meaning there was still a fair amount of absorption of radar waves.

The survey conducted in the Middle Cemetery was divided into two parts: a reticule of 0.8 x 0.8 m around tomb 9 (Figure 2.3), and exploration lines in and around the cemetery. The reticule around tomb 9 was conducted to attempt a geophysical characterisation of the tomb's geometry. This characterisation will provide basis for the detection of anomalies and patterns that might help to differentiate between geological structures and archaeological artefacts. The purpose of the exploration lines was gathering subsurface geological information like layering, while also investigating any anomalies that could indicate undiscovered tombs. The reticule around tomb 9 needed to be adjusted in one point to avoid the dromos of the tomb; therefore, there is one point where there is a distance of 1 metres between lines instead of 0.8 metres. The remaining lines were conducted above tombs 4 and 5, to the east of the cemetery, above dromos 13, through the cemetery oriented both north-south and east-west, as well as arbitrary lines diagonally through the cemetery.

Figure 2.3: A photo of part of the reticule done around tomb 9. The reticule was made using rope and tent pegs.

The reticule and some of the north-south and east-west lines were set up using rope and tent pegs. The tent pegs were hammered into the thin layer of soil covering the rock, and rope was tied around one peg, stretched, and attached to the second peg. When ropes were meant to be east-west or north-south oriented, a compass was used to ensure the second tent peg was in the correct position. This same procedure was used to set up some of the lines in the Upper Cemetery. After the data was collected, all ropes and tent pegs were collected, and all holes were filled to not leave any damage to the soil in the area.

The survey conducted in the Upper Cemetery consisted of lines that followed the asphalt roads going NE-SW and N-S, and the aforementioned lines set up perpendicularly or

parallel to the roads. Some lines were collected twice in different x-increments, like 5 cm and 1 cm, to increase the level of detail.

In both surveys, lines that were set up were collected by placing the antenna on top of one end of the rope, starting the acquisition, and pushing or pulling the antenna along the rope, depending on the terrain. The lines that were not collected using the ropes were collected mainly by pulling the antenna in an arbitrary direction or following the roads in the Upper Cemetery.

A total of 115 lines was collected, including test lines. As mentioned, there were different x-increments the lines were collected at, depending on the level of detail needed in the area: 9 cm for the least detailed, 1 cm for the most detailed, and 5 cm for a moderate level of detail (Figure 2.4).

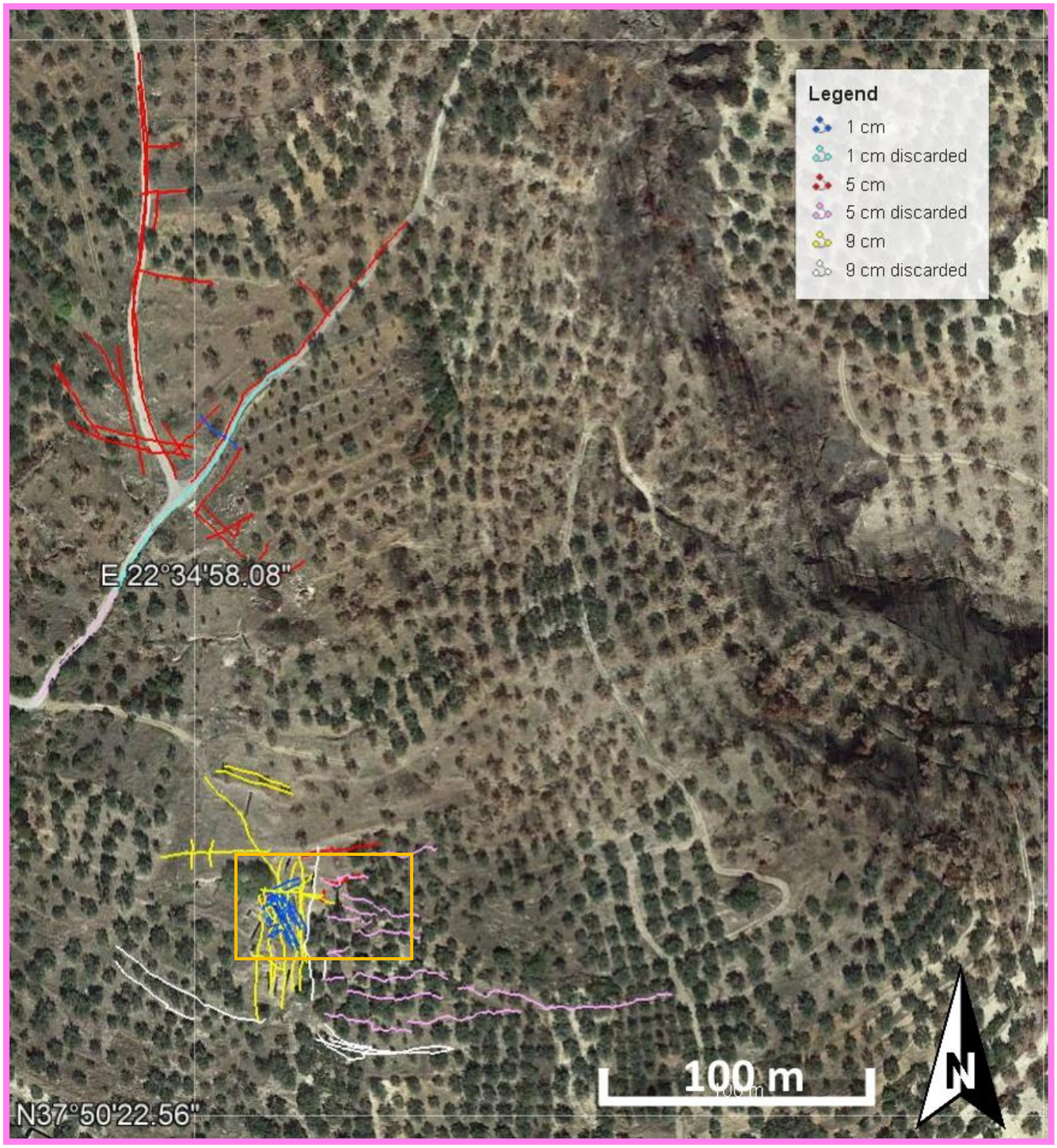

Figure 2.4: A map showing all collected GPR data, distinguishing between used and discarded lines; lighter colours indicate discarded lines. Imagery from Google Earth, 2013.

There were some lines planned originally that were not collected. This was due to three reasons: amount of vegetation, high slope angle, and roughness of the terrain. In some areas, the vegetation was so thick that it wasn't possible to move the antenna, or in other areas there were bushes or trees in the way of acquisition and data collection for those lines had to be terminated early. The slope angle in the Middle Cemetery was surprisingly steep, approximately 11° on average and over 30° in the steepest areas. This caused problems with acquisition, as it was difficult to push or pull the antenna at a steady speed with this kind of inclination. In some areas, it was not possible to acquire data due to the roughness of the terrain; this means that there are obstacles in the form of dromoi from tombs and rapid changes in slope angle.

2.2.3 Data processing

The GPR data was originally supposed to be processed in a software called RadExplorer version 1.42, produced by DecoPhysical and supplied with the MALÅ GPR antenna. However, because the workflow for this software required a lot of manual work and tests yielded poor results, MATLAB, developed by MathWorks, was selected to be used as the final processing software.

MATLAB has many advantages over RadExplorer. This is because it allows scripting and automation of the processing workflow. In addition, it allows processing of multiple lines simultaneously. RadExplorer on the other hand, requires each line to be processed interactively, one by one, which can be very time-consuming. In particular when the processing of the lines requires some trial and error.

A quality check of the data was done in MATLAB, and all lines that were found to show little to no signal due to strong absorption were discarded (Figure 2.5); this resulted in 26 lines being discarded. The final dataset consists of 89 lines (Figure 2.4). After a first round of processing the data, it was input into the interpretation software, Petrel, which showed there were issues with the GPS coordinates acquired by the internal GPS of the antenna. The greatest issue was with elevation, as in most cases, lines that were intersecting had

different elevations at the intersections. In some cases, this difference in elevation could reach up to 15.7 metres. This issue was fixed using data provided by the Nemea Center for Classical Archaeology, which was used to create a digital terrain model (DTM) of the study area. This data, upon testing, revealed a “stepped” elevation, which meant that the DTM had to be smoothed (Figure 2.6). Another issue was the x- and y- GPS coordinates, which can be seen when plotting these coordinates in a map with satellite imaging. In Figure 2.7 it is possible to see that some lines are crossing dromoi of tombs, which is not possible as the data could not be acquired in this way. In other places, the lines appear to be shifted slightly in different directions. This issue cannot be fixed through processing. If the survey was to be repeated, an external GPS like an RTK GPS antenna should be used to guarantee better coordinate accuracy.

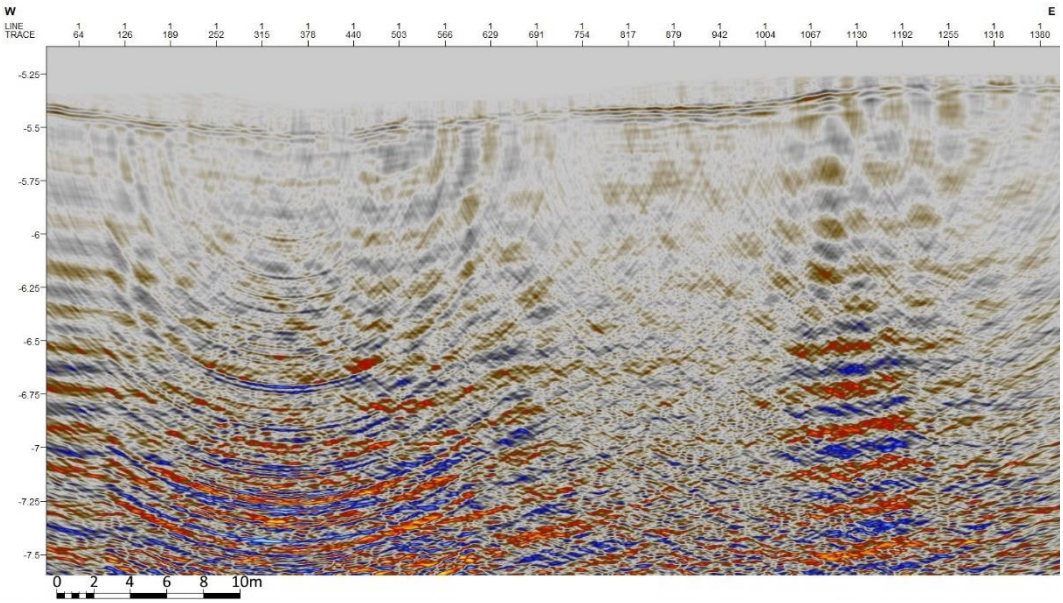

Figure 2.5: A discarded line showing no data other than the surface, with a high amount of noise. Screenshot taken in Petrel.

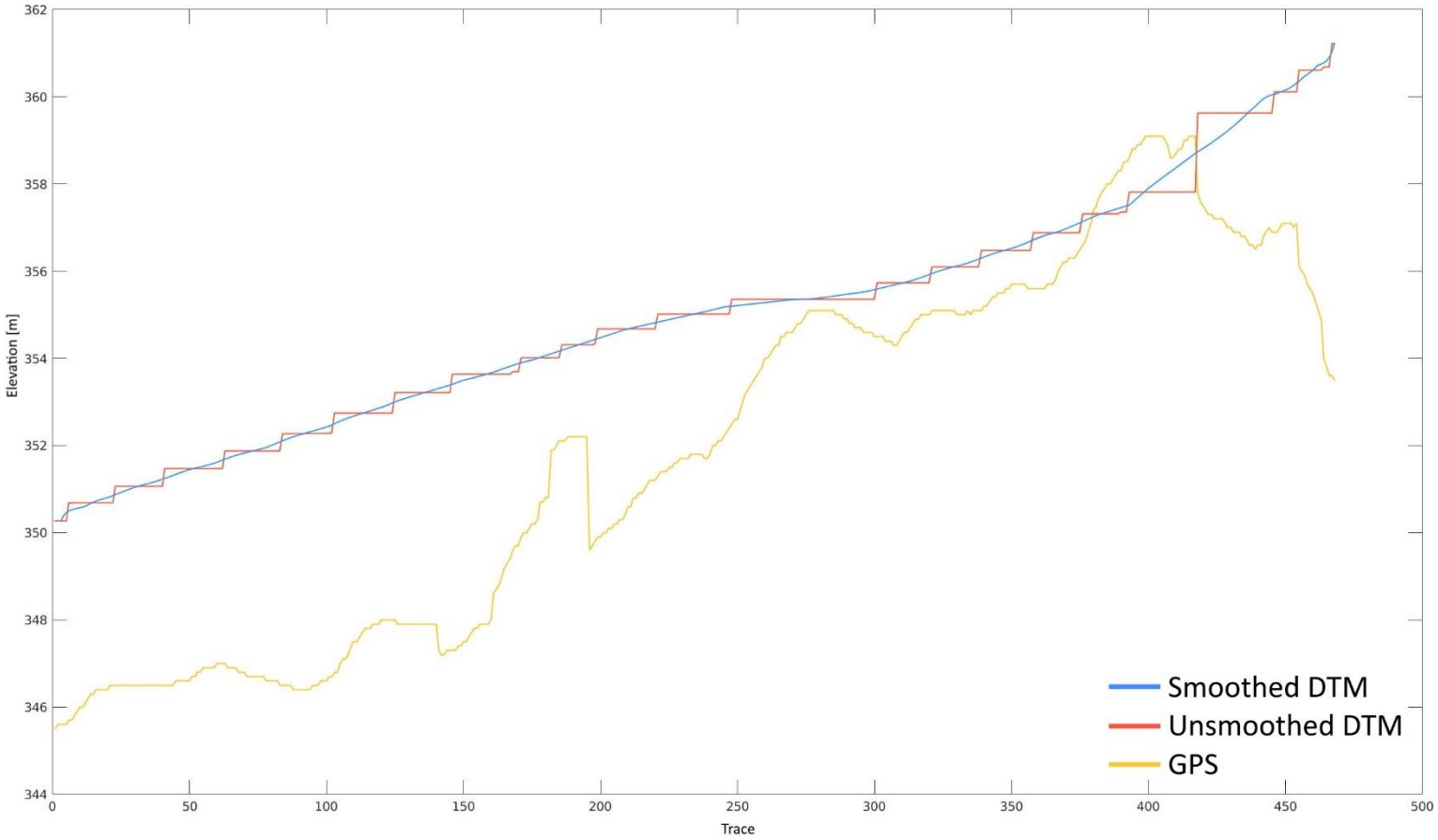

Figure 2.6: Elevation profiles of line DAT_0025. The yellow line is the built-in GPS, the orange is the unsmoothed DTM, and the blue is the smoothed DTM, which was used in the topographic correction. Screenshot from MATLAB.

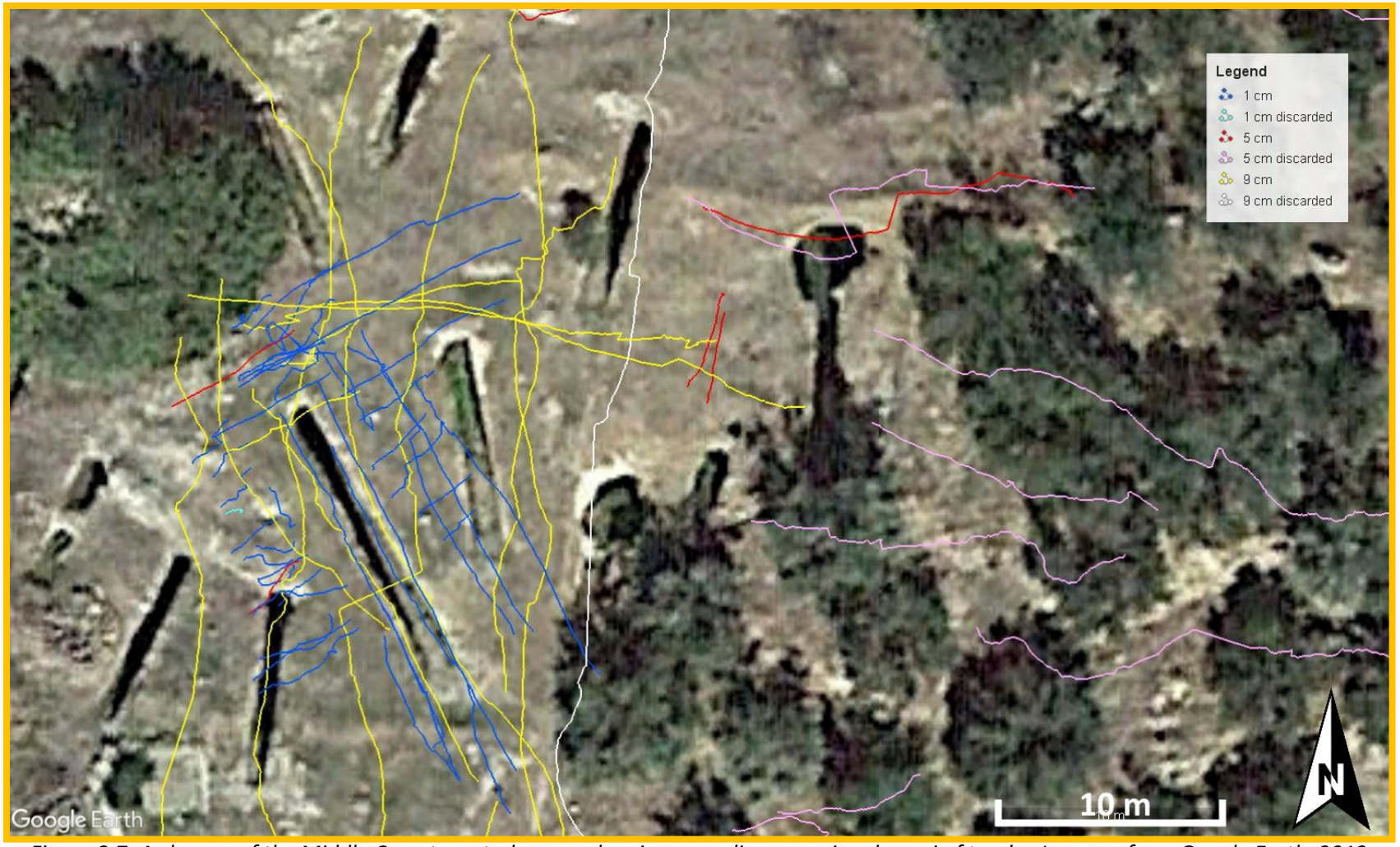

Figure 2.7: A closeup of the Middle Cemetery study area, showing some lines crossing dromoi of tombs. Imagery from Google Earth, 2013.

The code used to process the data can be broken down in different parts, each part serving a different purpose (Figure 2.8). The first part of the code (1) is used to set the location of the files intended for processing, as well as the list of files processed and the text file with coordinates of the DTM. A path is set for the code to use to access the files, and the list of files ensures that only high-quality files are processed. The DTM will be used at a later stage in the code, but as it is used in every line, it is introduced before the data starts looping.

The next part of the code is where the loop commences (2). Each file is selected and using the list of files, and here all constant parameters like velocity, height of the datum, zero-offset time, and the x- and z-increments are set (3); every line has the same parameters to allow for the data to be saved as one dataset to be input into Petrel. All of the constant parameters are set to be in cm, µs, or cm/µs. The height of the datum is set to 40015 cm, the x- and z-increments, dx and dz, are both set to 4 cm, the zero-offset time, t0, is set to 30 µs, and the velocity, V, is set to 6000 cm/µs.

Next, the code reads the .rd3 file to extract the number of traces and frequency for each line, and later the same is repeated with the .cor file to extract the x-, y-, and z- GPS coordinates (4). The latitude and longitude coordinates are transformed into UTM-34N format using a call to maproject from GENERIC MAPPING TOOLS (Wessel and Luis, 2017). The DTM is then used to replace the z-coordinates in each line to ensure correct elevation (5). The DTM data is smoothed by a running average of 50 samples to remove the "stepped" effect. In some places, the difference between original z-coordinate and DTM z-coordinate was up to 22 metres, which shows how inaccurate the built-in GPS of the antenna can be.

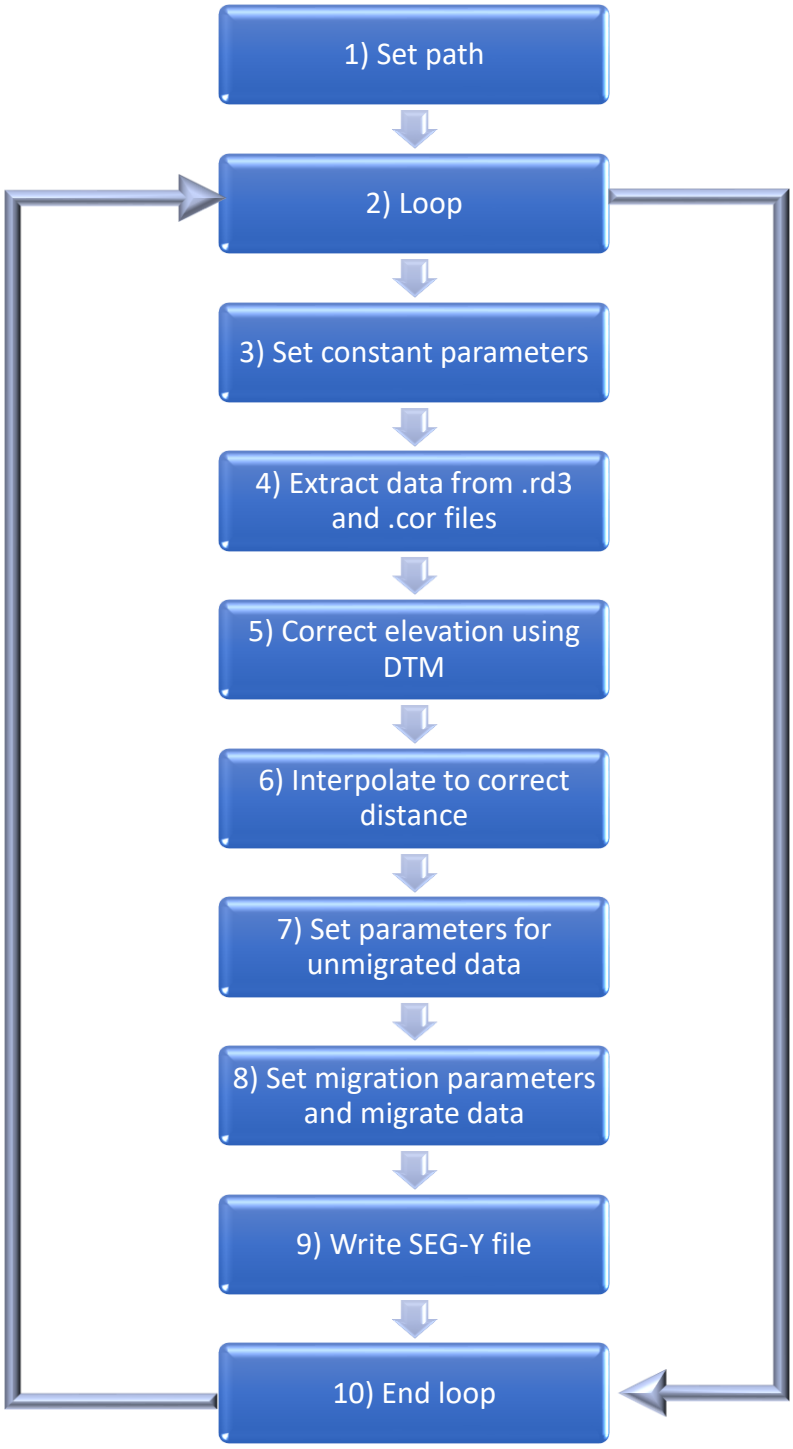

Figure 2.8: A workflow showing the processing steps in MATLAB.

Once the elevation is corrected, the data is interpolated into distance and converted to cm (6). Parameters are set for unmigrated data with no topography (7), and next parameters for migration are set, like height of the data, which was set to 1900 cm. The migration used in this code is the Kirchhoff migration, also known as diffraction stack, which treats every point as a diffractor and calculates its amplitude using Kirchhoff summation. The migration automatically sets the topography, and outputs the results in depth (8). This method creates unwanted background noise in areas where there is pre-existing, which can luckily be easily distinguished from reflectors due to the shape of a "smiling" hyperbola.

The final section of the code converts the migrated data into a SEG-Y file (9). First, a temporary SEG-Y file is created prior to writing headers. The formatting and order of headers is very important, because Petrel requires a very specific set-up of the data included in headers. Once the headers are written, the code uses the "WriteSegyStructure" function from the SEGY-MAT open source package to finalise the SEG-Y file, which is then ready to be loaded in Petrel for interpretation. Once this section is finished for the last file, the loop ends (10).

The entire code can be found in Appendix 1.

2.2.4 Interpretation

The interpretation of the data was done in Petrel, which is the standard software used for seismic interpretation. GPR data looks somewhat like seismic but is focused on the first tens of metres below the surface. The data was imported in depth as a whole project, in the UTM-34N coordinate system in WGS84. When opening a 2D or 3D window, it is possible to see the location of lines with respect to each other, where they intersect, and how great of an area they cover (Figure 2.9). Because the datum was set as a constant in all lines, there are many lines where there is a section where there is no data above the surface (Figure 2.10A). Therefore, the surface was first marked using the "Manual interpretation" tool from the "Seismic interpretation" tool palette (Figure 2.10B). The

purpose of this step was to show the upper boundary of the data. The two areas with the greatest concentration of data were marked with polygons using the “Polygon editing” tool from the “Seismic interpretation” tool palette, and these polygons and the interpreted surface was used to create two surfaces, one for the Middle Cemetery and one for the Upper Cemetery, using the “Make surface” function from the “Seismic Interpretation” ribbon (Figure 2.11).

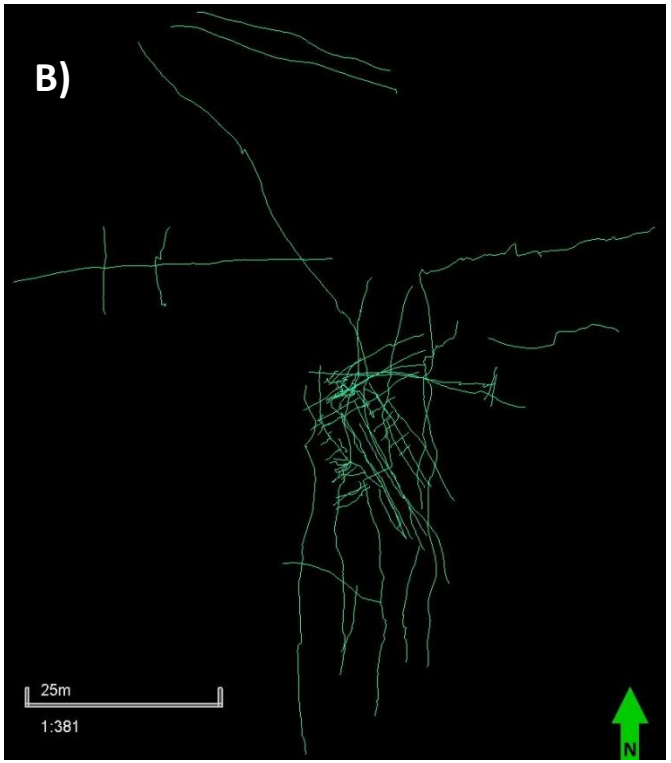

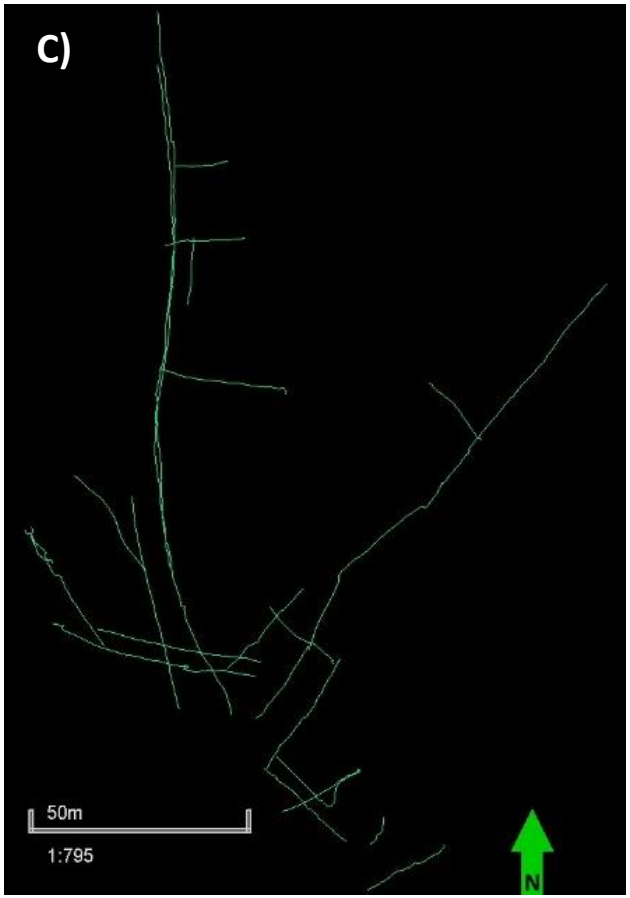

Figure 2.9: The dataset in Petrel. A) is the full dataset, B) is a zoom to only the Middle Cemetery, and C) is a zoom to only the Upper cemetery.

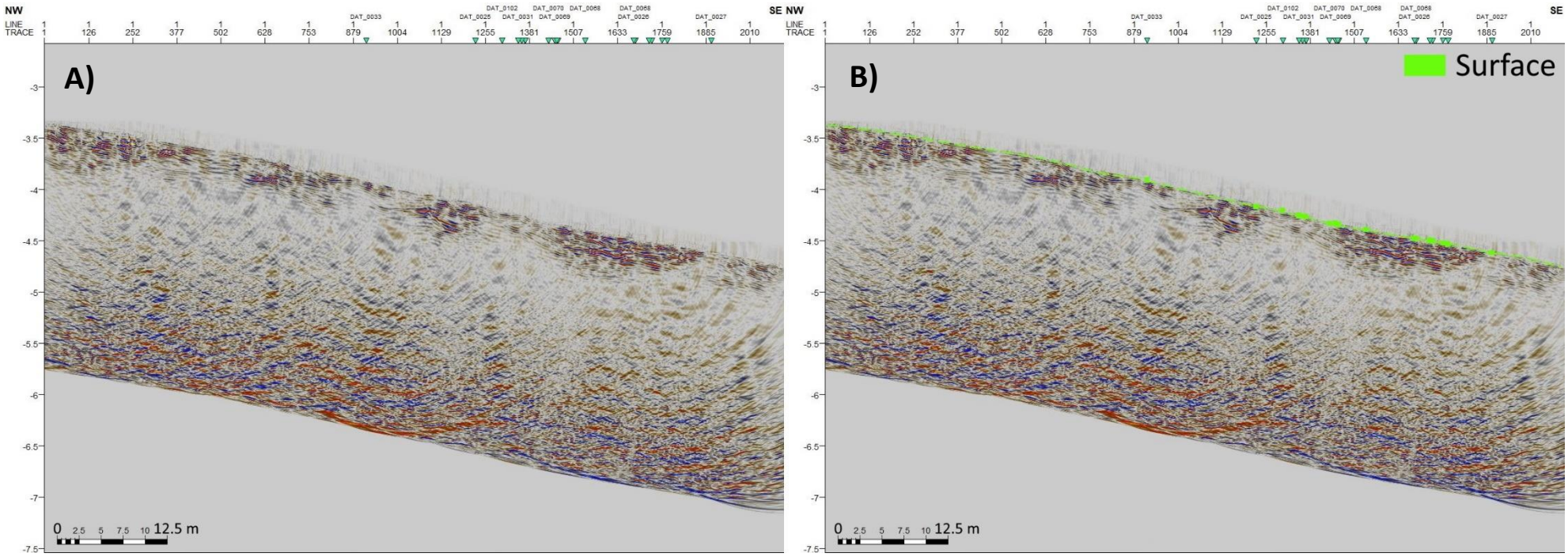

Figure 2.10: Screenshots from Petrel showing line DAT_0038. A) shows the uninterpreted line, with the surface clearly visible. B) shows the surface as interpreted in green.

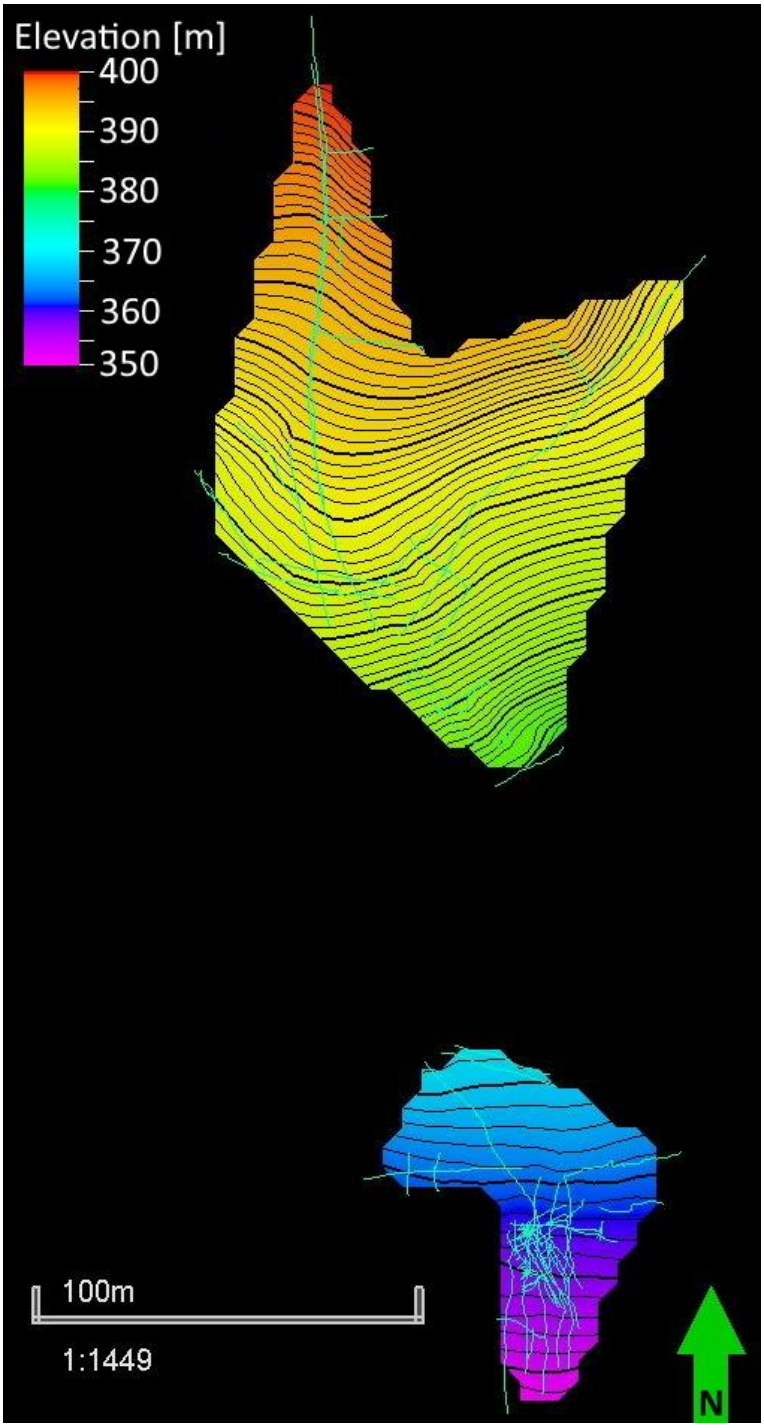

Figure 2.11: The surface, showing topographic lines. Red is the highest elevation while purple is the lowest elevation.

Any areas showing strong, continuous reflectors were marked as “features” and interpreted, first by setting a base, which is an arbitrary horizon that shows the lower boundary of high-quality signal. Identification and digitalisation of reflectors with similar geometry, elevation, and amplitude will suggest the lateral extent of the features, which can span over single or multiple lines. When the base of the feature was interpreted, three horizons within the feature were interpreted (Figure 2.12). This interpretation is done using the “Manual interpretation” tool from the “Seismic interpretation” tool palette. There are two exceptions as there was only one horizon of interest in these two features. The interpretation of horizons clearly shows the dip angle and direction of the layering in the area.

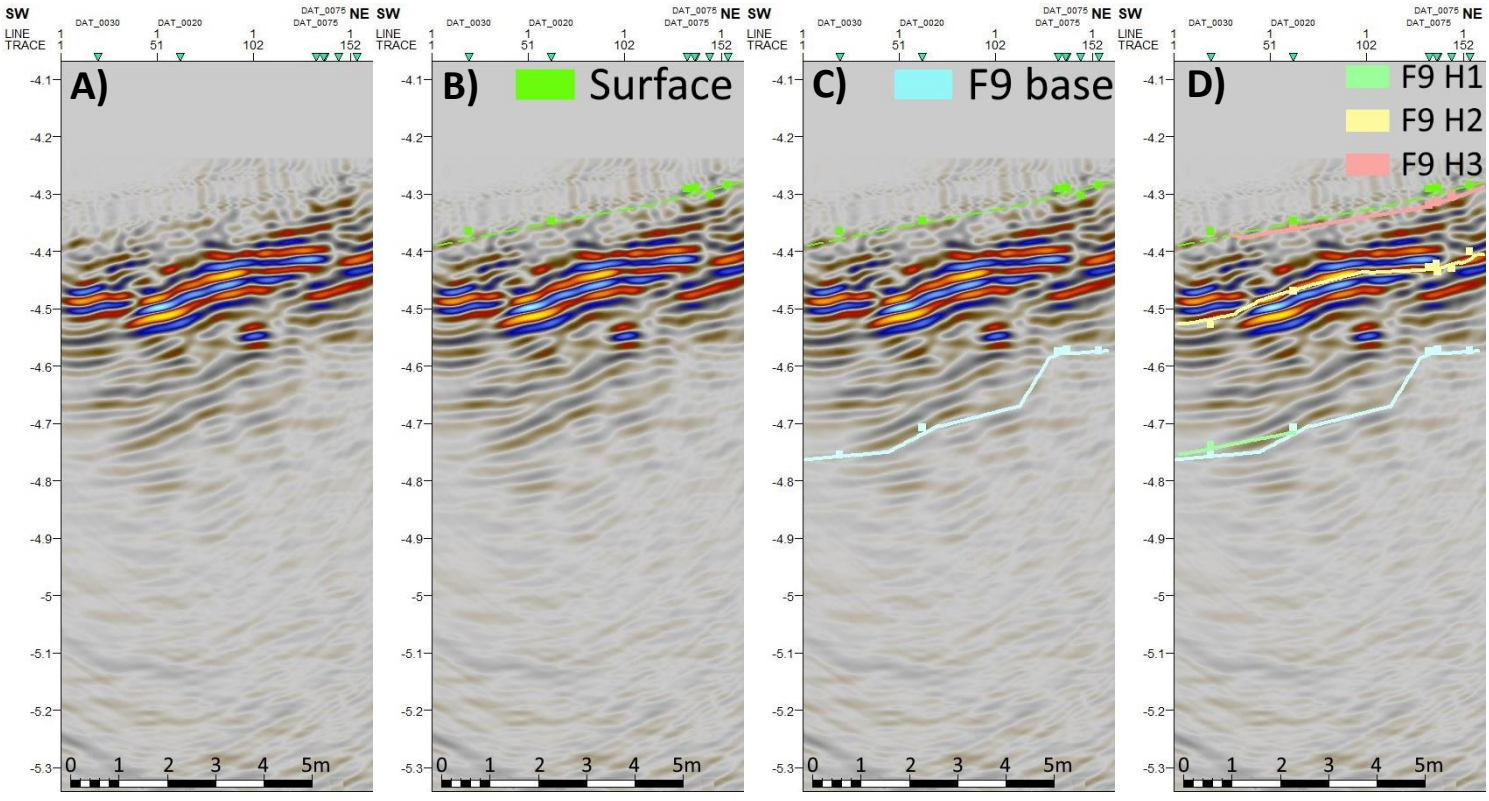

Figure 2.12: Line DAT_0045, showing the different steps of interpretation. A) shows the blank line, B) shows the interpreted surface, C) shows the interpreted base of the data, and D) shows the interpreted horizons.

After features with horizons were interpreted, areas of low amplitude reflectors, or wipeouts, were also interpreted using the “Manual interpretation” tool from the “Seismic interpretation” tool palette. These were marked as boxes showing the depth and lateral extent of the wipeouts (Figure 2.13). Some wipeouts show an area with low amplitude reflectors that are continuous and can be traced across, while others show an area of low amplitude chaotic reflectors. A special case is a feature that looks like a wipeout in one line, but in the perpendicular line it shows a strong signal response; this was marked the same way as a wipeout would, with the lateral extent and depth marked.

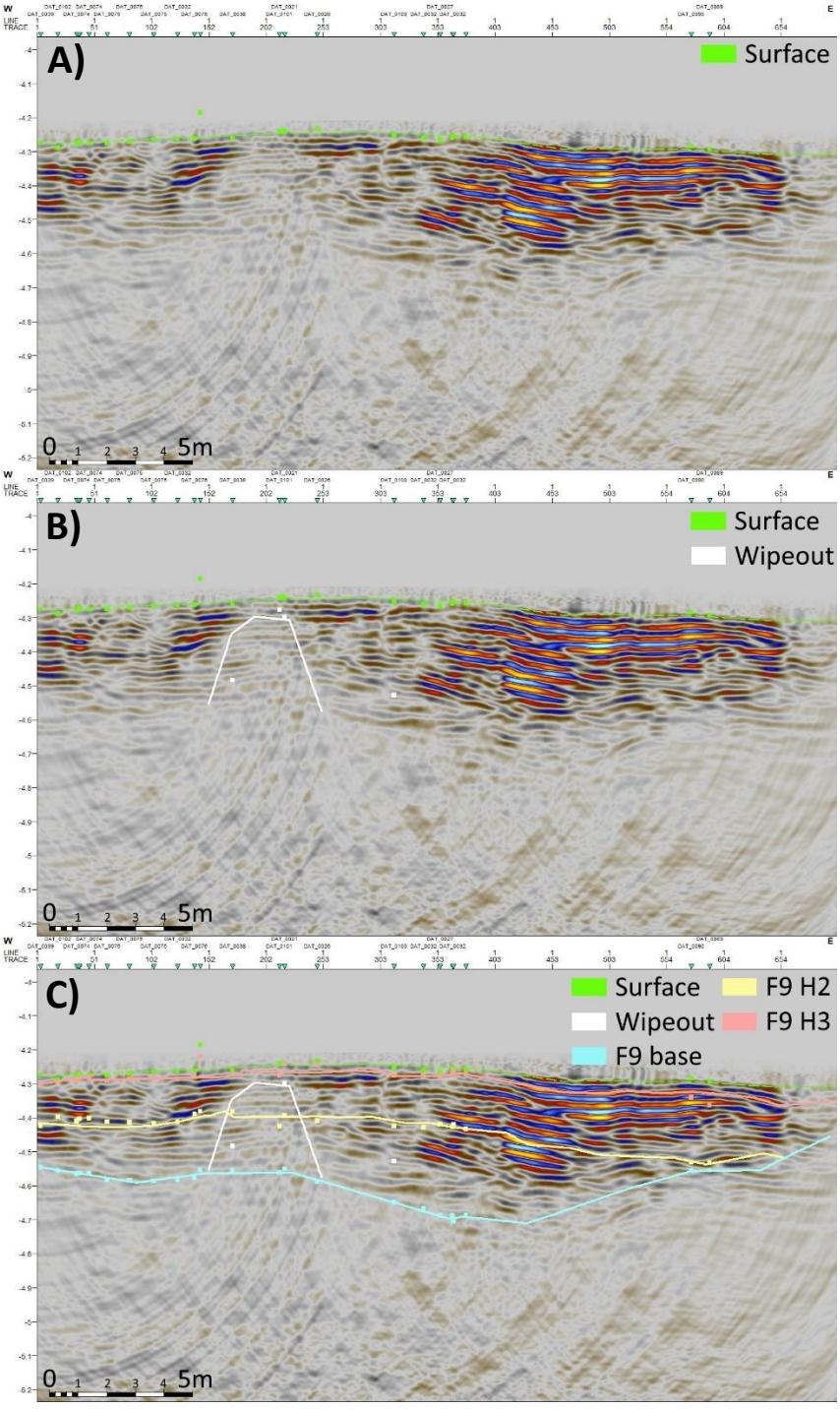

Figure 2.13: The interpretation of a wipeout in line DAT_0031. A) shows the line with the surface interpreted, B) shows the wipeout interpreted, and C) shows all interpretation.

There are some offsets visible in the data, spanning over two or more horizons. These were marked using the “Interpret faults” tool in the “Seismic interpretation” tool palette (Figure 2.14). Interpreting these can give useful information about the lines, and some can likely be traced across multiple lines. Because the data is not a regular grid, each offset was interpreted separately.

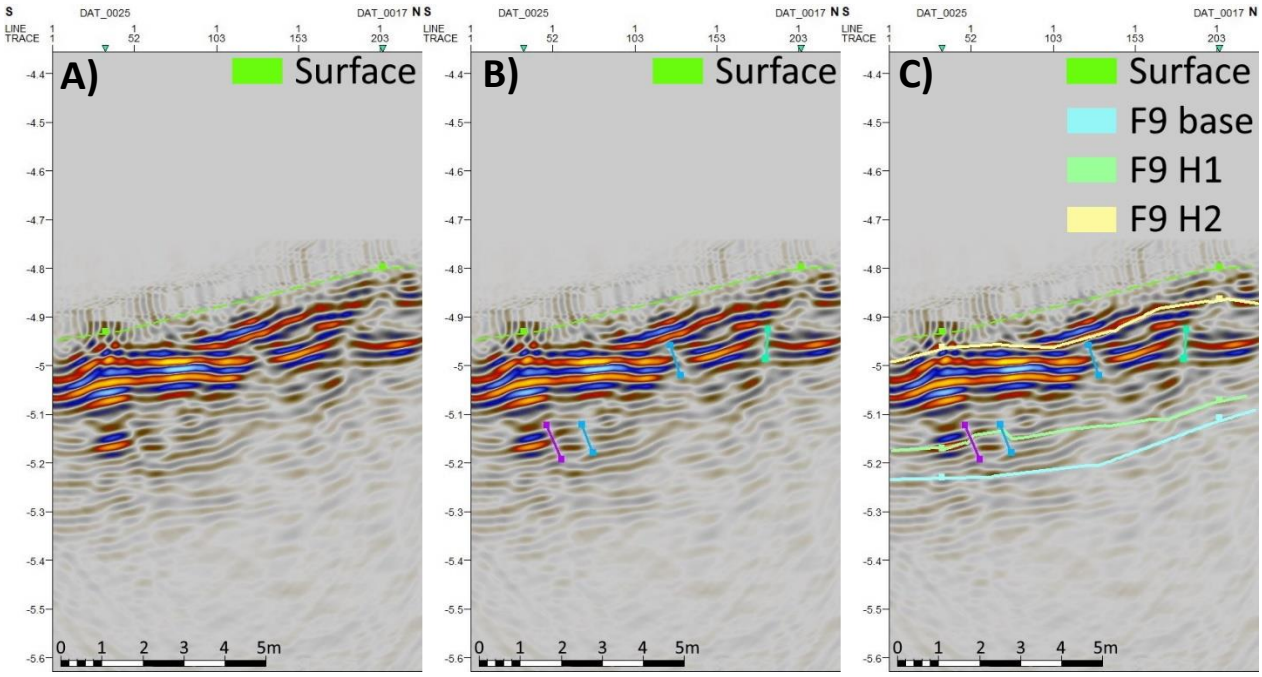

Figure 2.14: Interpretation of offsets, as shown in line DAT_0016. A) shows the line with the surface interpreted, B) shows offsets interpreted, and C) shows all horizons and offsets interpreted.

Some attributes were also used to accentuate features in some lines in the dataset. The attributes used were the instantaneous phase and cosine of phase, which clearly show where there are continuous reflectors versus noise; both attributes have the same function, but cosine of phase is black and white while instantaneous phase is colourful. Figure 2.15 shows an example of a line with no attributes, the cosine of phase attribute, and the instantaneous phase attribute; a wipeout with chaotic low-amplitude reflectors is present in the line, which is emphasised clearly by the attributes.

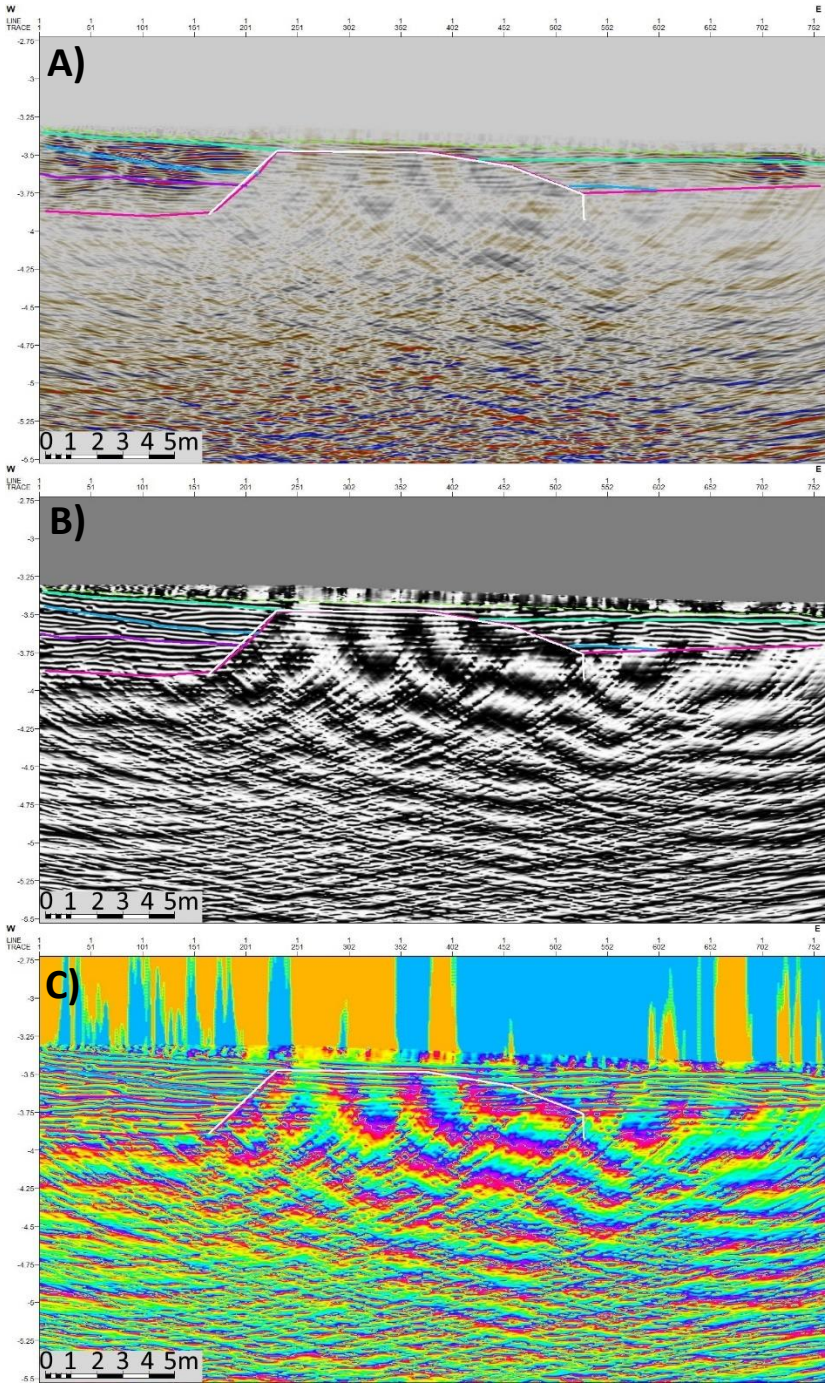

Figure 2.15: Line DAT_0036 showing a large wipeout in the middle. A) shows the line with no attribute, B) shows the cosine of phase attribute, and C) shows the instantaneous phase attribute.

3 Results

The results of this project are split into the geological field map and the GPR data, of which the latter is the main focus. The GPR data is split into features and offsets, and wipeouts and other artefacts.

3.1 Geological field map

The geological field data collected during this project, as well as some information from Paraskevopoulos et al. (1990), was compiled into a geological map using ArcMap. There were limited outcrops that allowed for measurements of dip and dip direction in and around the cemetery, so these measurements were done in more distant stations. The geological field map can be seen in Figure 3.1, and an enlarged version of the same map with focus on the Upper, Middle, and Lower Cemetery in Figure 3.2.

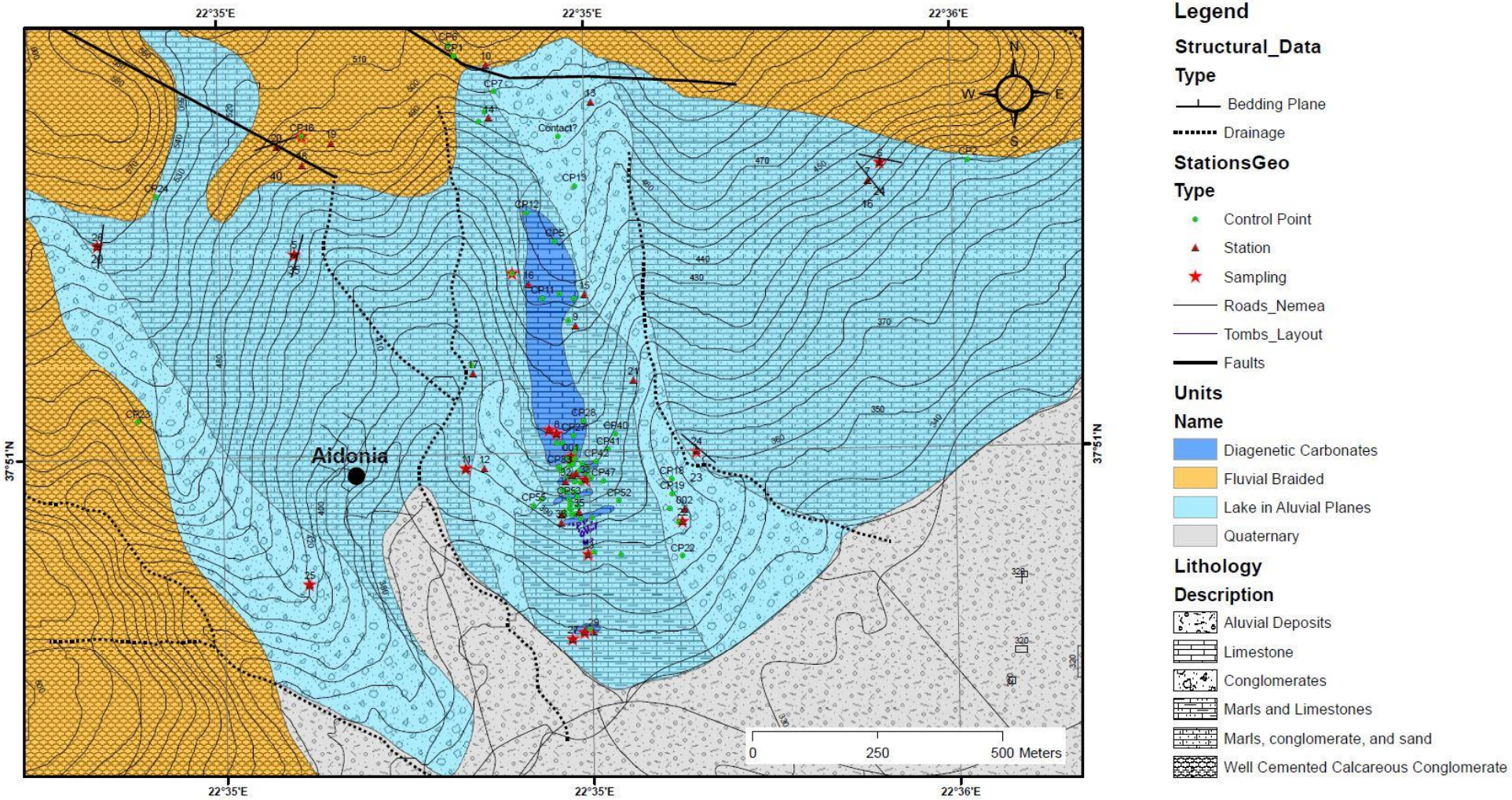

Figure 3.1: Geological map created using data collected during this project, as well as some information from Paraskevopoulos et al. (1990).

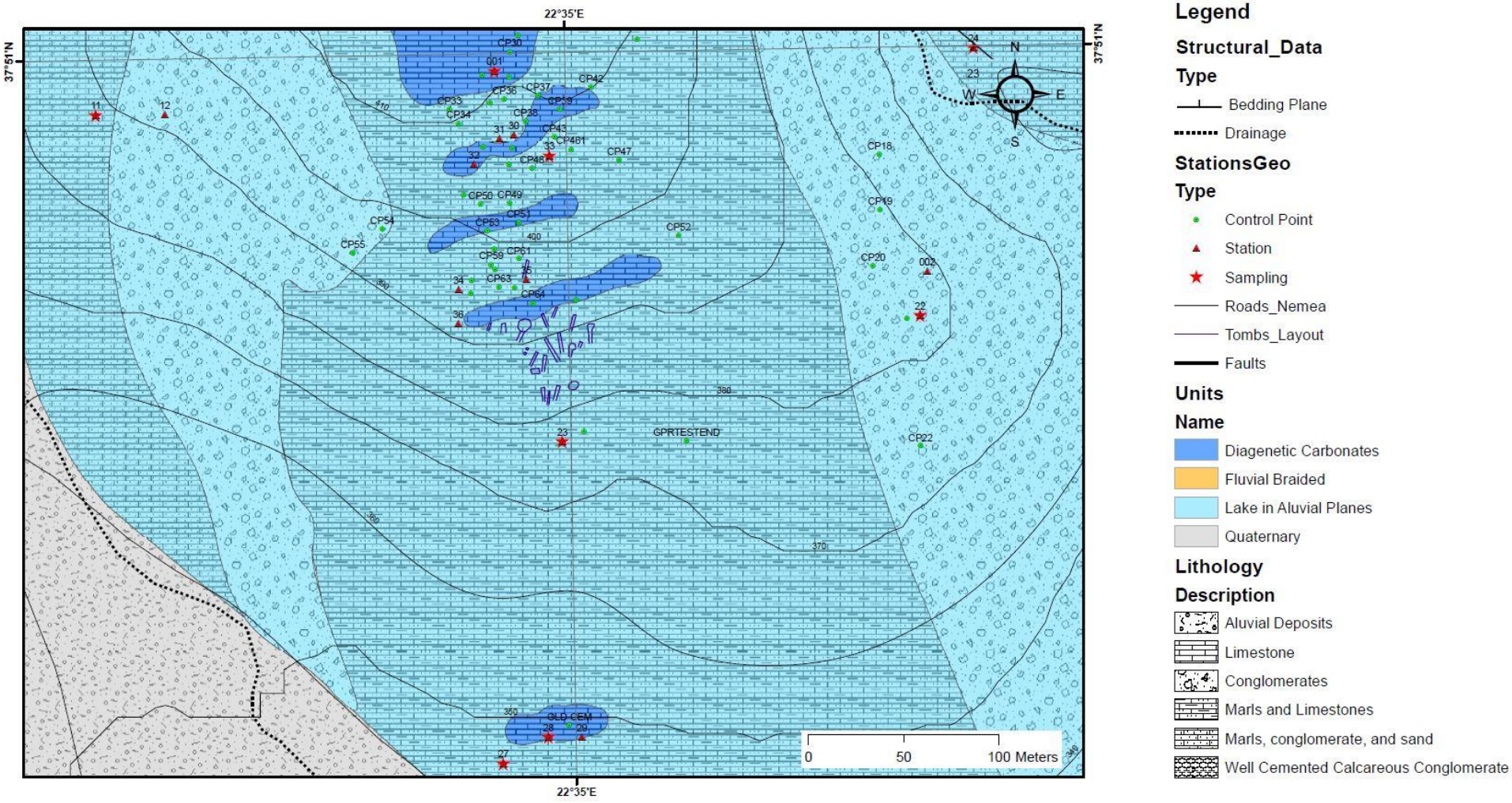

Figure 3.2: An enlarged version of the same map shown in Figure 3.1, with focus on the Upper, Middle, and Lower Cemetery.

The maps show a clear distinction between depositional environments and lithologies. In Figure 3.1 it is possible to see that most of the study area has been deposited in lacustrine environments, surrounded by fluvial units from the north and west. Quaternary infill is present mostly from the southeast, and in one of the drainage systems to the west of the Aidonia Cemetery. The lacustrine unit can be divided into several lithologies: conglomerates, marls and limestones, and marls, conglomerate, and sand. These are all present in and around the Aidonia Cemetery (Figure 3.2), as well as some diagenetic limestones that are harder and more consolidated than the surrounding lacustrine lithologies.

The fluvial units are all well cemented calcareous conglomerate, with some variability in colour, ranging from brown to bluish-grey, hardness, and support type. In some areas, the conglomerate was brown, matrix-supported, and softer, while in other areas it was bluish-grey, more clast-supported, and very hard. This clast-supported conglomerate showed obvious signs of dissolution and karstification, but also layering (Figure 3.3).

Figure 3.3: Clast-supported, bluish-grey conglomerate showing karstification and layering, underlain by a yellow calcareous sandstone. Photo from Station 4.

The marls and limestones vary in hardness and colour. The harder limestones tend to be grey to white, while softer marls tend to be white to beige in colour. Marls in different areas of the study area behave differently, as some are more consolidated while others crumble when lightly touched. Figure 3.4 shows an outcrop of a soft, white marl in contact with a coarser-grained, harder rock.

Figure 3.4: An outcrop of soft, white marl overlain by a harder calcareous sandstone. Photo taken at Station 24.

The geological maps allow for a greater understanding of the facies present in the GPR survey area and can aid in predicting the behaviour of the EM waves. Ideally, the penetration should be good, depending on the grain size of the limestone/marl.

3.2 GPR data

The study area is located on limestones and other calcareous rocks, and the GPR data shows that the penetration of EM waves in this area is very low; the deepest continuous reflectors are at a depth of approximately 8 m, while the average depth of continuous reflectors and useful data is between 3-5 m. This allows for only a limited interpretation of the subsurface. The low penetration is likely due to the fine-grained marls that behave like clay, or possibly due to oversaturation of water caused by ground-water flow or irrigation in the olive grove. Figures 3.5 and 3.6 show the locations of lines in figures in the results and discussion sections.

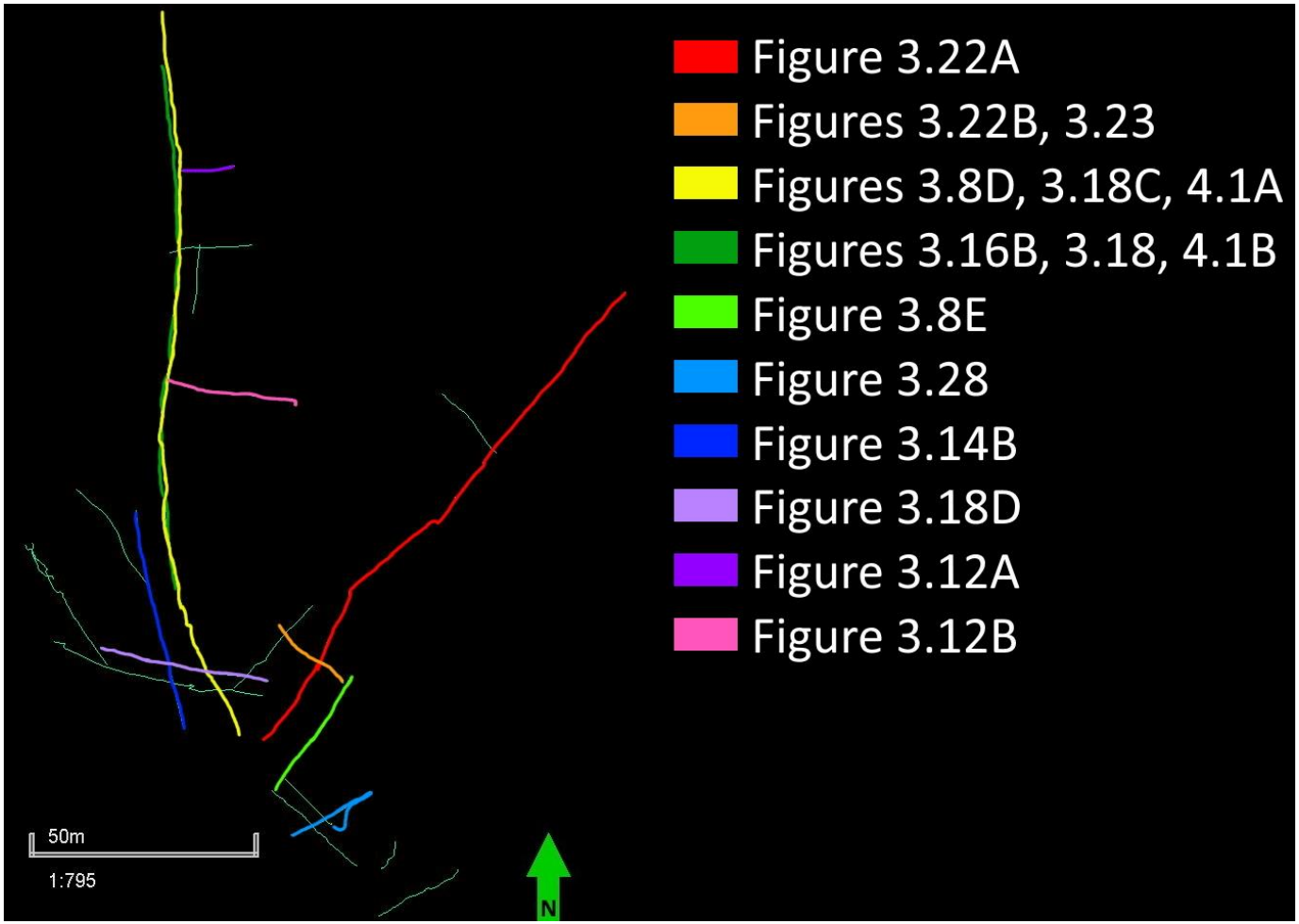

Figure 3.5: The locations of lines in figures in the results and discussion section, Upper Cemetery.

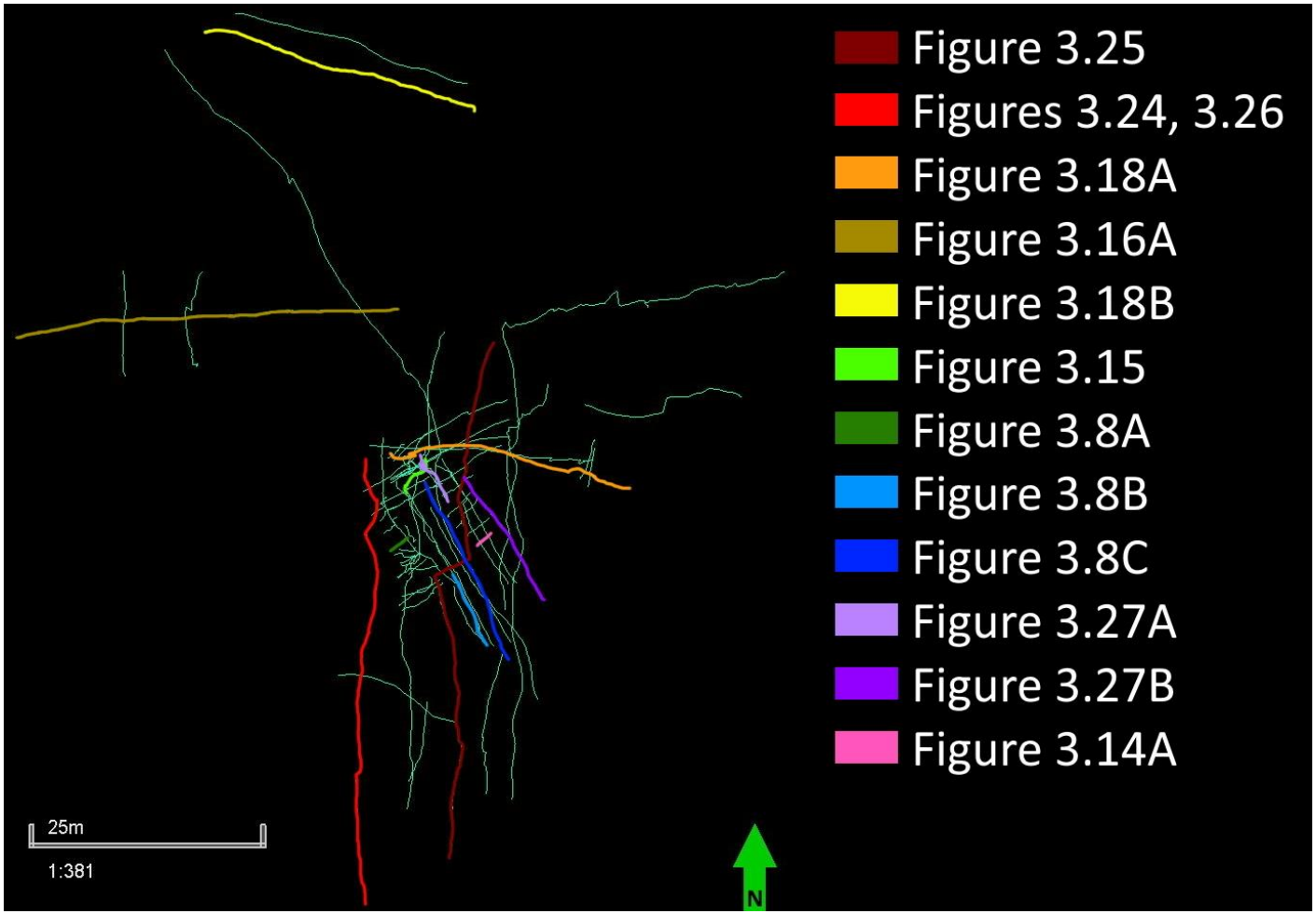

Figure 3.6: The locations of lines in figures in the results section, Middle Cemetery.

3.2.1 Features and offsets

A total of nine features (F1-F9) are interpreted in the project, where six of the features (F1-F6) are in the Upper Cemetery and three of the features (F7-F9) are in the Middle Cemetery. Features are areas with high-amplitude, continuous reflectors that have varying sizes, and are often separated by wipeouts; some features can likely be grouped together, but because a wipeout is present between them, they were interpreted separately. Figure 3.7 shows the locations of these features.

All features, except for features F3, F5 and F6, have three horizons (H1-H3) interpreted. These horizons were selected to be spread somewhat evenly through the subsurface. However, depending on the position on the slope, the top (Horizon 3 – H3) or bottom (Horizon 1 – H1) horizons can be missing. From the interpreted horizons, it is possible to see that the rock layers in the area dip at a very similar angle to the surface (Figure 3.8). In places, the difference in angle can cause the surface to erode into the topmost horizon (Figure 3.8C), in some cases the horizon reappears when the dip of the surface decreases again. A similar phenomenon happens with the base of the features, which is an arbitrary horizon bounding the continuous reflectors, and the lowest horizon, which can appear to be cut off due attenuation of the GPR signal (Figure 3.8C). Feature F3 is a special case, because of a large wipeout that disconnects two parts of the feature, shown on the right in Figure 3.8D. Because of this, the first and second horizon are separated from the main part of the feature and are called H1N and H2N. Horizon H3 can be traced through the wipeout, so this horizon is the same in both parts of F3.

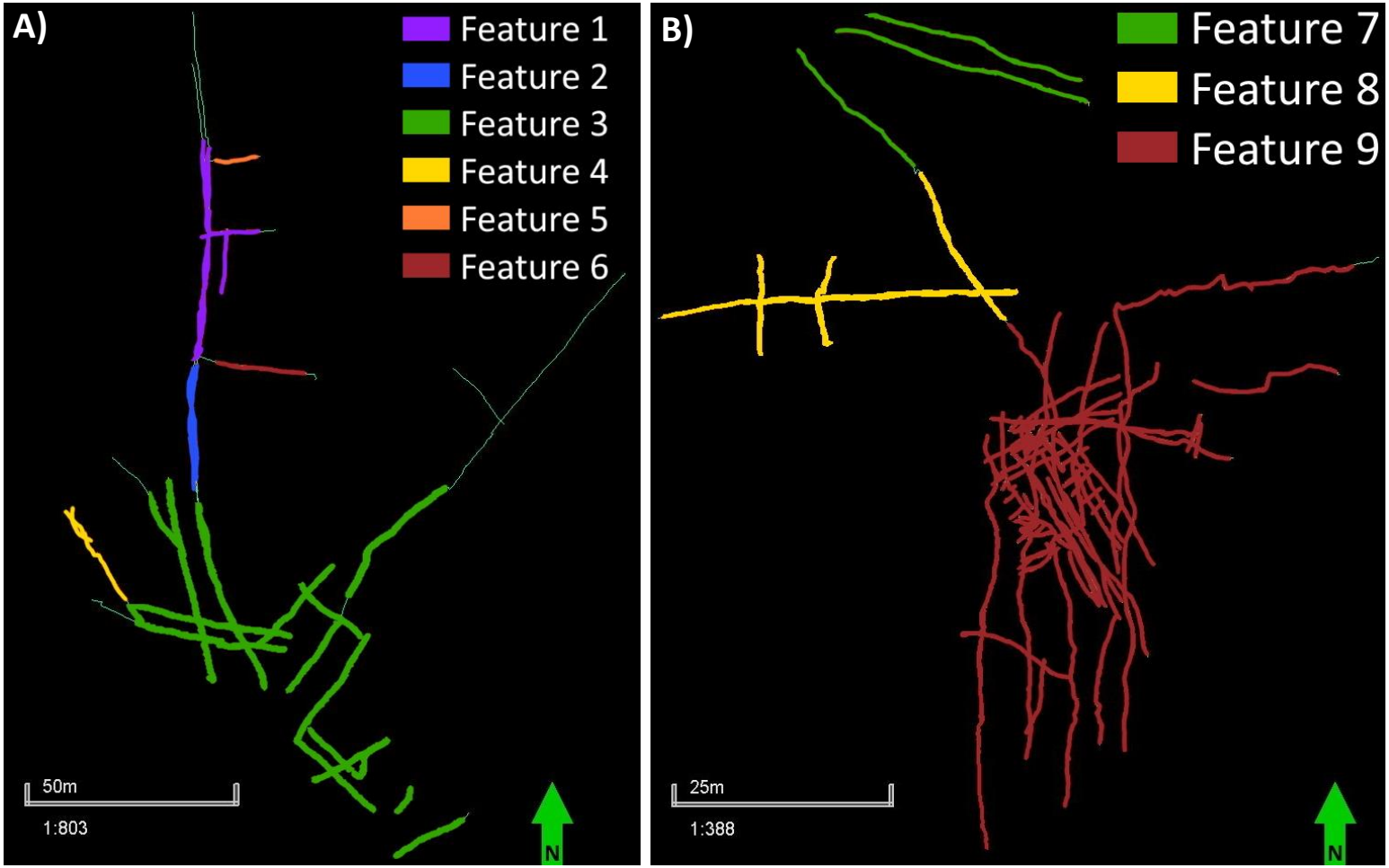

Figure 3.7: Locations of features F1-F9, divided into A) Upper Cemetery and B) Middle Cemetery.

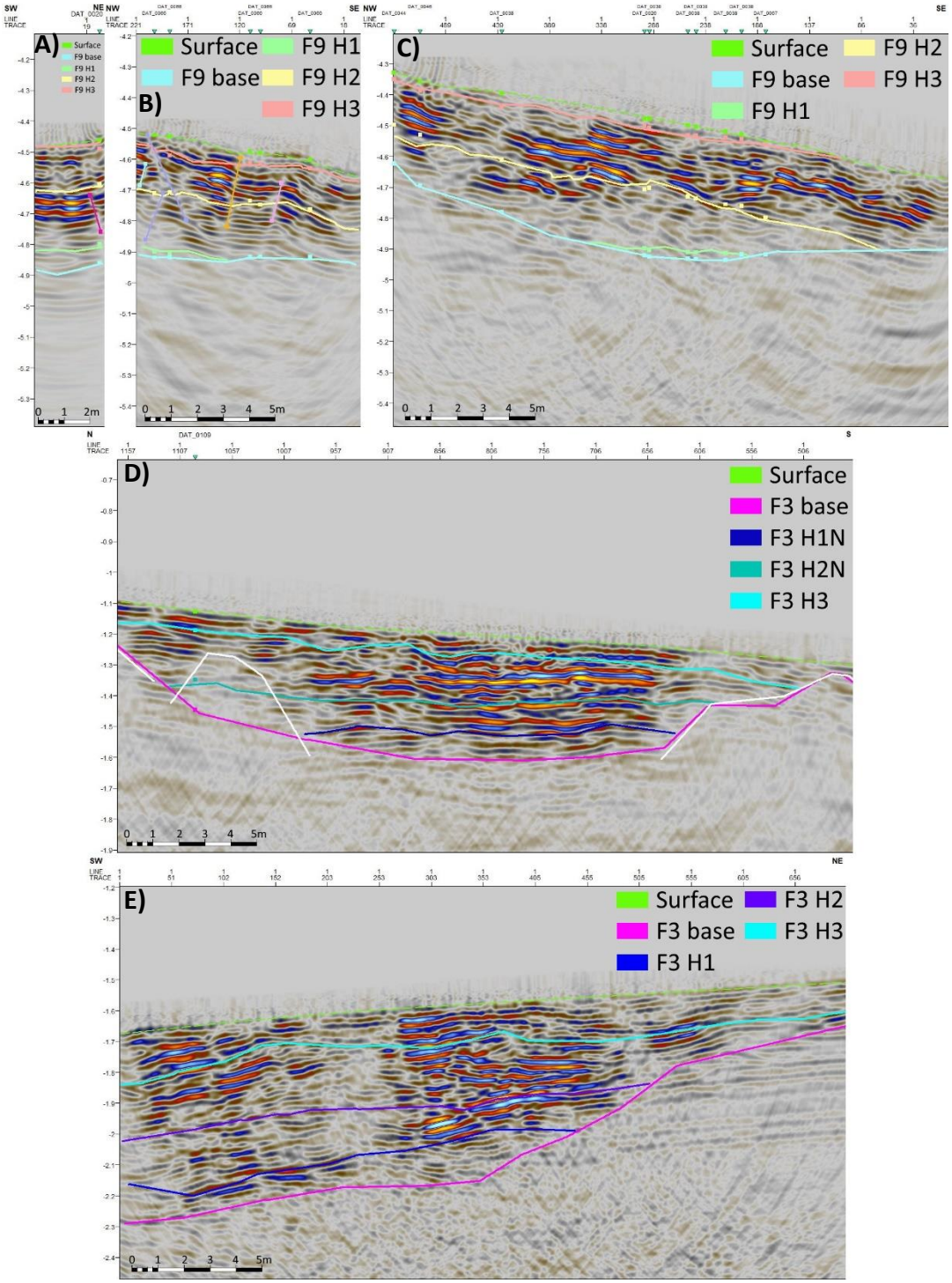

Figure 3.8: Different examples showing the general dip angle and direction of horizons as compared to the surface. A) line DAT_0052, B) line DAT_0064, C) line DAT_0068, D) line DAT_0108, and E) line DAT_0113.

Thickness maps of horizons H1-H3 were created for Feature 9. The thicknesses are less than the true thickness due to a change in velocity from acquisition to processing, in reality the thickness should be at least double. Horizon H1 shows negative thickness in some areas, which means that it is below the base of the feature at times. The average thickness for H1 is 0.05 m. Horizon H2 has two thickness maps, due to horizon H1 not covering the entire area of H2; therefore there is one thickness map in the area where H1 underlies H2 (Figure 3.10A), and one between H2 and the base of the feature (Figure 3.10B). The average thickness of H2 is approximately 0.25 m. Horizon H3 shows a relatively even thickness with an average of 0.15 m. The thickness maps can be seen in figures 3.9, 3.10, and 3.11.

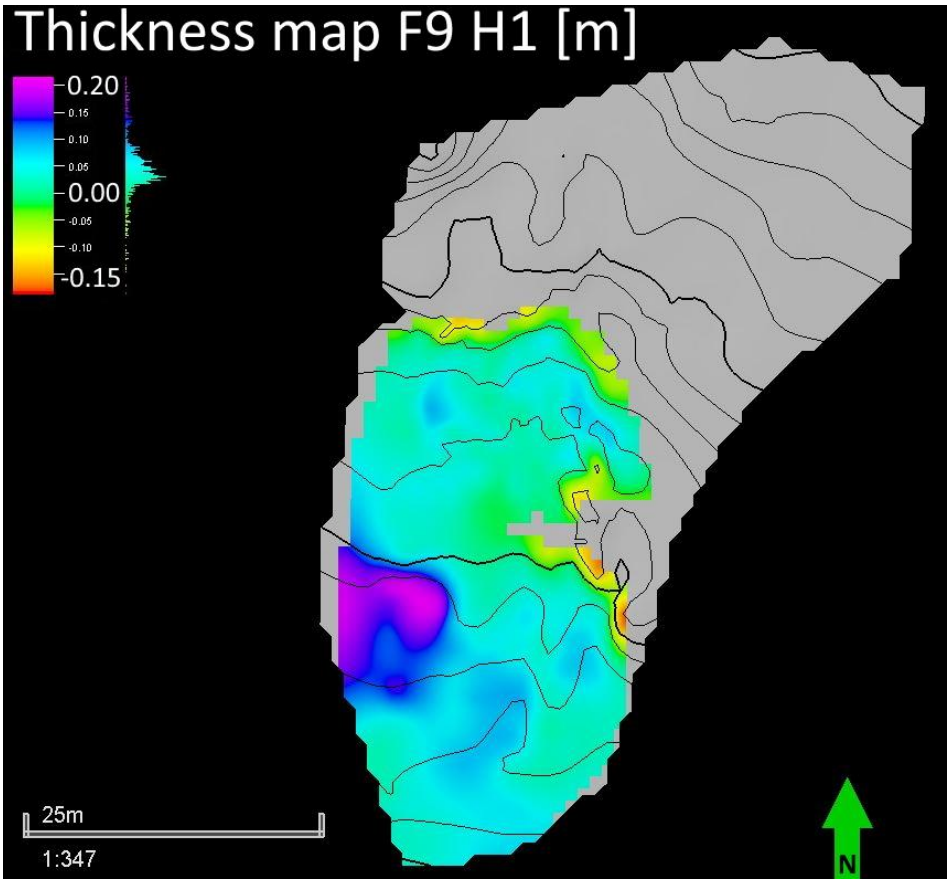

Figure 3.9: Thickness map of F9 H1.

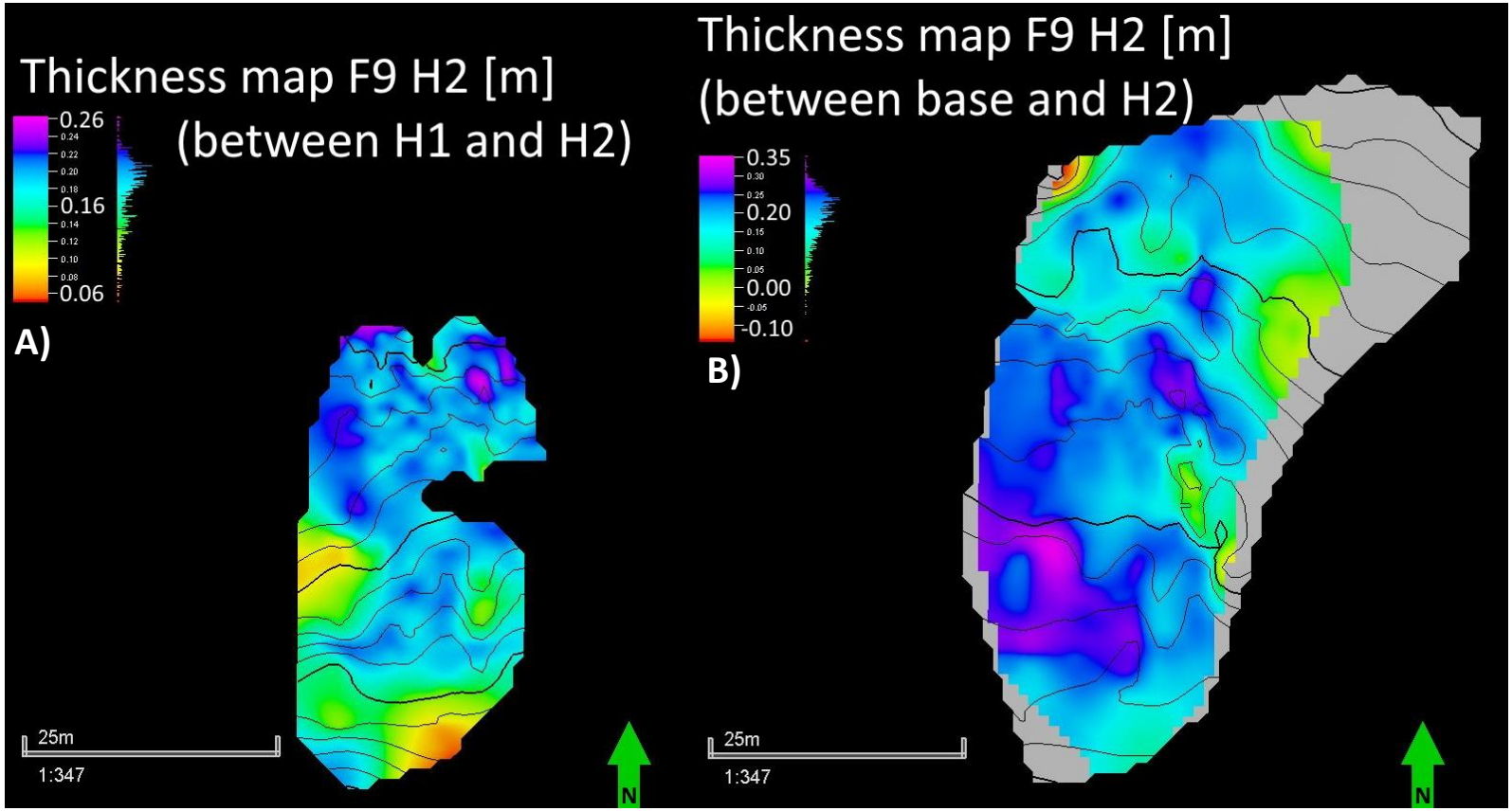

Figure 3.10: Thickness map of F9 H2. A) between H1 and B) between the base of the feature.

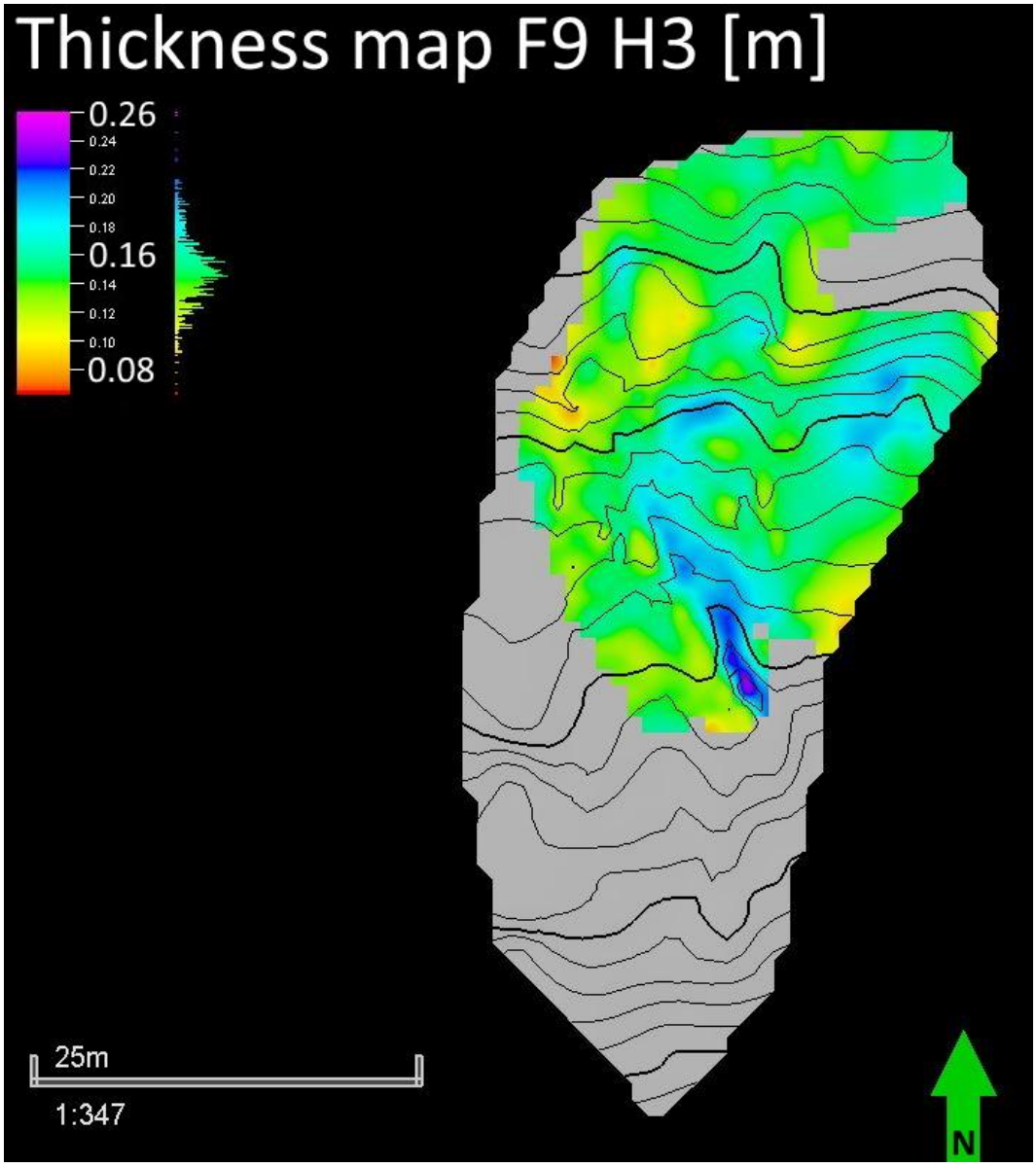

Figure 3.11: Thickness map of F9 H3.

Features F5 and F6 are different to the remaining features in that they only have one horizon interpreted. In both features, the horizon is about two to three metres below the surface and starts as a reflector that dips in the same direction as the surface. In the eastern part of the feature, however, the reflector dips to the east. This behaviour in the

subsurface indicates a change in dielectric permittivity or conductivity that increases insulation properties and gives a strong response compared to the surrounding areas, that appear to have higher conductivity. Features F5 and F6 can be seen in Figure 3.12.

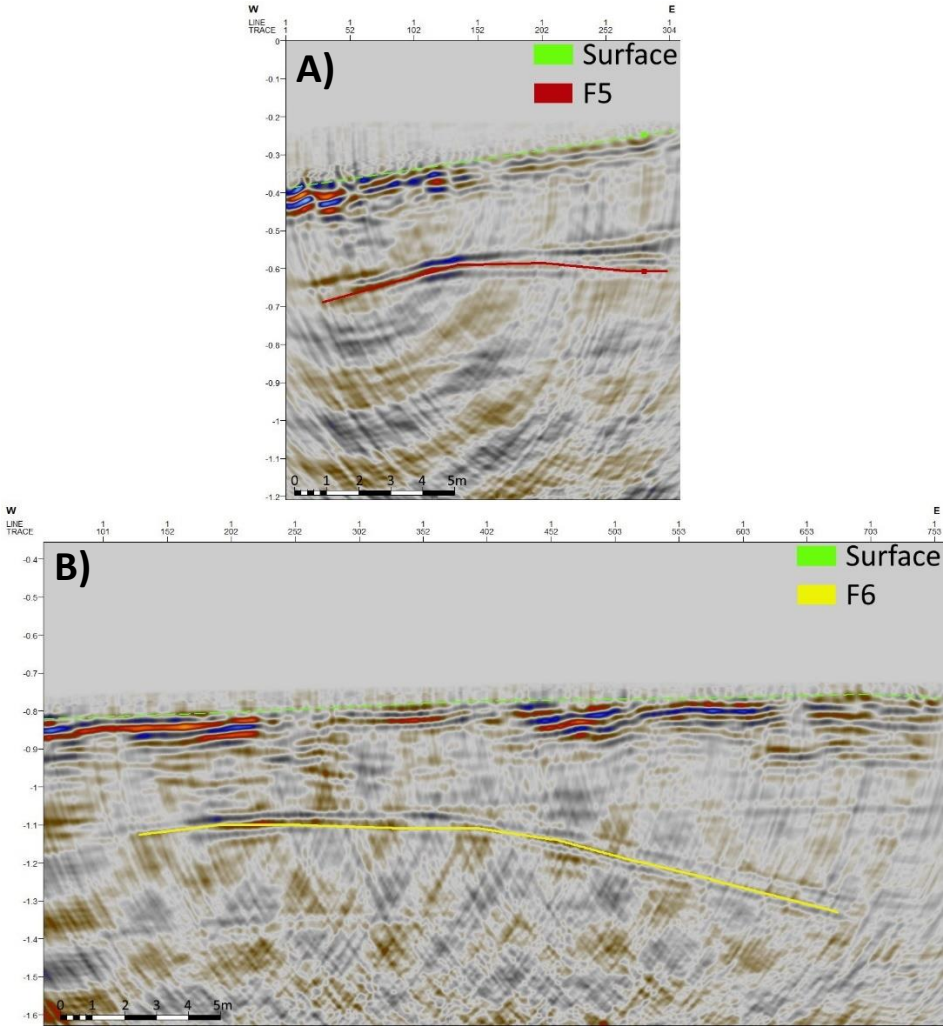

Figure 3.12: A) Feature 5 in line DAT_0124 and B) Feature 6 in line DAT_0127. Both lines are at a similar depth and both dip towards the east.

Fault-like offsets are found in almost every GPR line, except for two lines. A total of 438 offsets are interpreted in the dataset. The Middle Cemetery has 262 offsets interpreted, while the Upper Cemetery has 176 offsets. The locations of all offsets are shown in Figure

3.13. The longer lines tend to contain more offsets, with the greatest number of offsets interpreted in a single line being seventeen. Shorter lines tend to have between one and five offsets (Figure 3.14A). It is possible that multiple offsets can be interpreted as a fracture plane that spans across multiple lines, but due to the sheer number of offsets interpreted, this was not attempted. It is clear, however, that many of these offsets are very small and localised; they tend to span over two to fifteen reflectors, and the fault displacement can be less than half a reflector to maximum one and a half reflectors (Figure 3.14B). In some places, something that appears as an offset can have no movement at all, and these are assumed to be joints. The amount of joints and small-scale faults in the data proves that the Aidonia Cemetery has been affected by faulting of m- to cm-scale that is most likely connected to the larger-scale faults located in the northwest of the study area. More examples of offsets interpreted in the study area can be found in Appendix 2, figures 7.1 and 7.2.

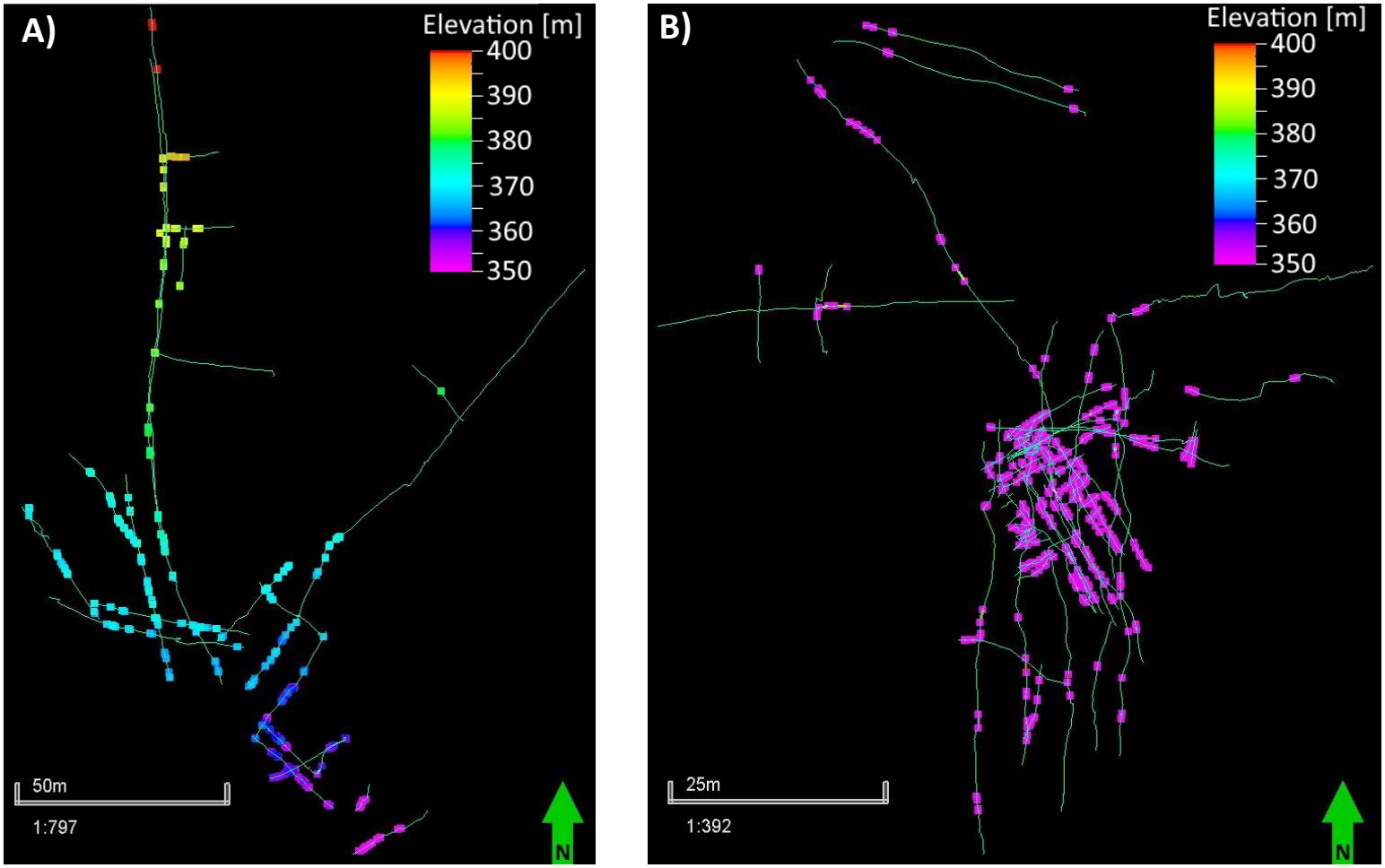

Figure 3.13: Locations of all offsets in A) the Upper Cemetery and B) the Middle Cemetery. The colours indicate the elevation of the offset.

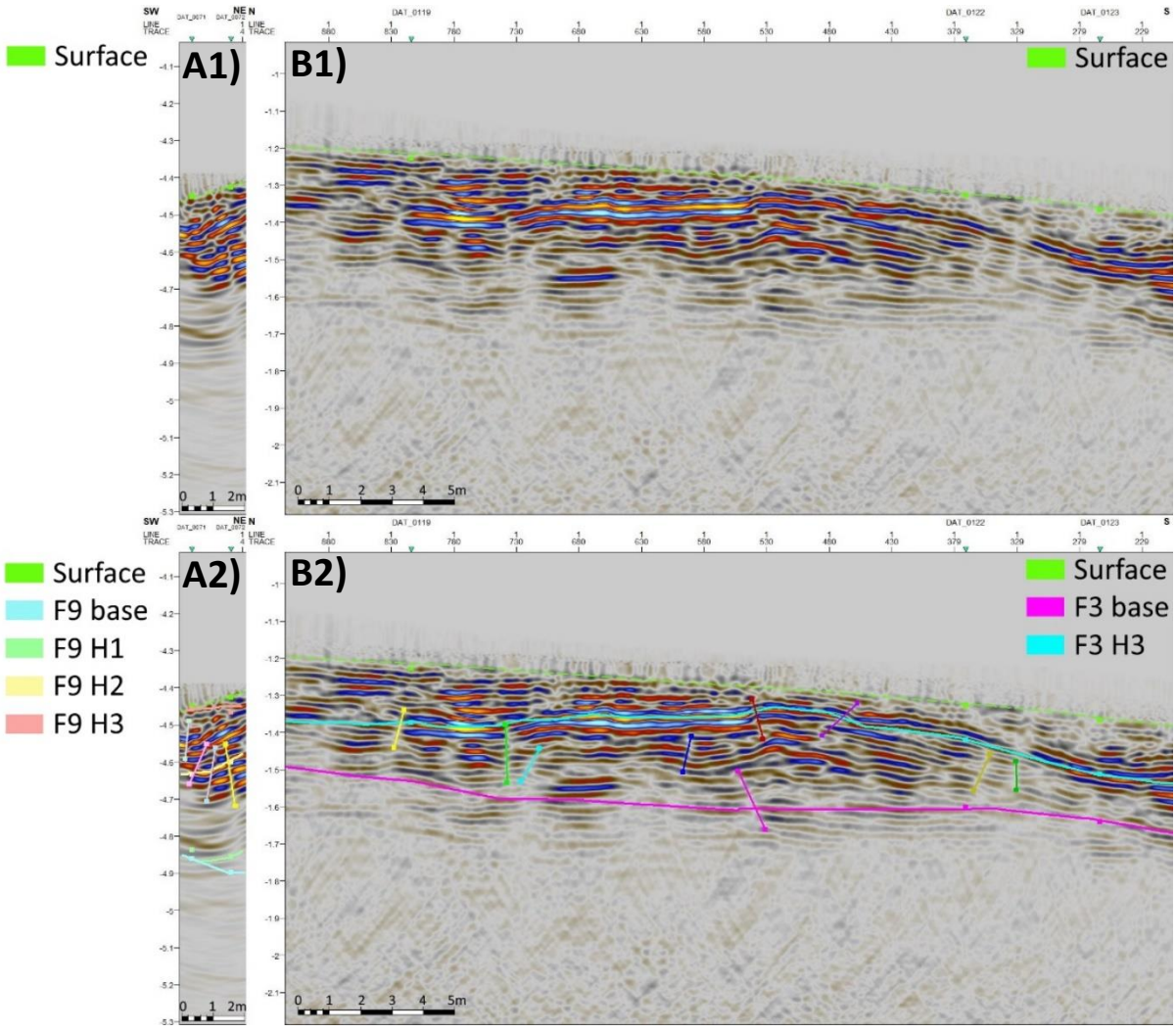

Figure 3.14: Examples of offsets. A1) shows line DAT_0095 with no interpretation, A2) shows the same line interpreted. B1) shows line DAT_0118 with no interpretation, B2) shows the same line interpreted. Offsets are at different angles and in different directions.

Offsets in the dataset can display both normal and reverse fault characteristics, and in some areas, wedges are visible. A wedge happens when a package is bounded by two faults that dip in opposite directions, where the package between them is pushed up or down to create a miniature horst or graben. Many of these were found in the dataset, and an example is shown in Figure 3.15. More examples of wedges interpreted in the study area can be found in Appendix 2, figures 7.3 and 7.4.

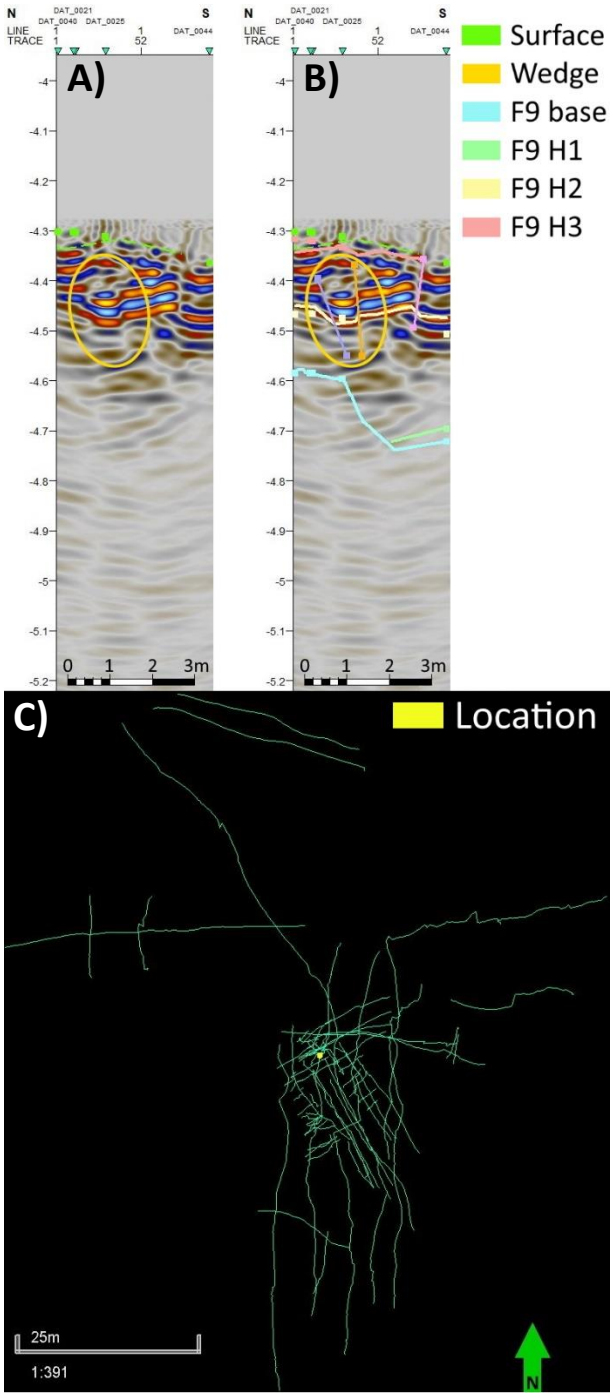

Figure 3.15: A wedge displaying graben characteristics in line DAT_0041. A) shows the uninterpreted line, B) shows the full interpretation, and C) shows the location of the wedge in the Middle Cemetery.

Pinchouts of layers and packages can be observed in areas not affected by faulting. They occur on different scales, sometimes just two reflectors that merge into one, other times thicker packages spanning over four reflectors or more pinch out into a single reflector. Some examples of this are shown in Figure 3.16. More examples of pinchouts can be found in Appendix 2, figures 7.5, 7.6, and 7.7.

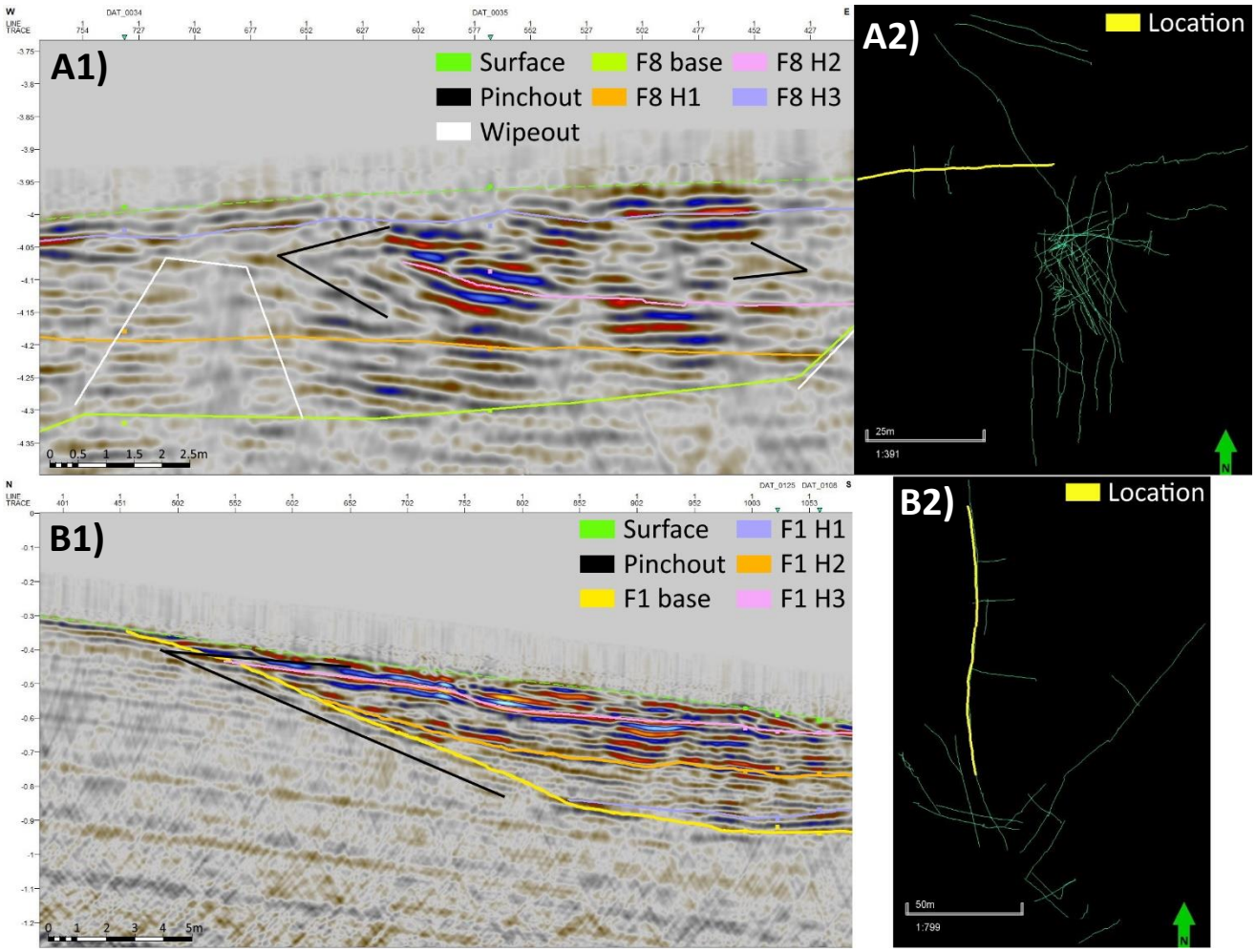

Figure 3.16: Two examples of pinchouts in the dataset. A1) shows line DAT_0033 with the location of the line in A2), while B1) shows a large-scale pinchout in the northernmost part of line DAT_0109, with the location of the line in B2).

3.2.2 Wipeouts and other artefacts

A total of 33 wipeouts are interpreted in the dataset (Figure 3.17). They are present both in the Middle and the Upper Cemetery and vary in size; in some cases, the wipeout spans through entirety of the depth of the interpreted horizons (figures 2.15 and 3.18B), while in other cases the wipeout is more localised and covers only part of the depth (Figure 3.18D). In some places, as stated previously, it is possible to trace some continuous low-amplitude reflections across the wipeouts (Figure 3.18A). In some cases, however, it is only possible to trace reflectors across using instantaneous phase or cosine of phase attributes, as shown in Figure 3.19. Wipeouts are areas of increased absorption of EM waves, and can have several causes: there could be irrigation or ground-water flow increasing the water saturation, or it could be localised excavation and infill; in both cases this could be due to natural or anthropogenic origins. More examples of wipeouts can be seen in Appendix 2, figures 7.8 and 7.9.

In the Middle Cemetery (Figure 3.17B) it is possible to see a collection of wipeouts (circled). These coincide somewhat with the position of the chamber of tomb 8 (Figure 1.3). One of these wipeouts can be seen in Figure 3.18A. This is strange behaviour, as voids tend to appear as high-amplitude reflectors with hyperbolae, indicating a difference in velocity. Perhaps this collection of voids indicates higher water saturation or an infill.

Lines DAT_0036 (figures 2.15 and 3.18B) and DAT_0037 (Figure 7.9.) both show a wipeout that is located where a chamber would be located if dromos 13 (Figure 1.3) was a completed tomb. This wipeout could indicate something like an area of high-water saturation, as the rock in this area was hard and well consolidated. It did not differ much from the surrounding area, other than an increased hardness in this specific location.

Wipeouts in the Upper Cemetery (Figure 3.18C and D) could indicate a number of things; an irrigation pipeline or ground-water flow, a change in grain size or general lithology, or even a possible infill in an undiscovered tomb. These wipeouts are worth investigating, especially if it is seen in lines perpendicular to each other.

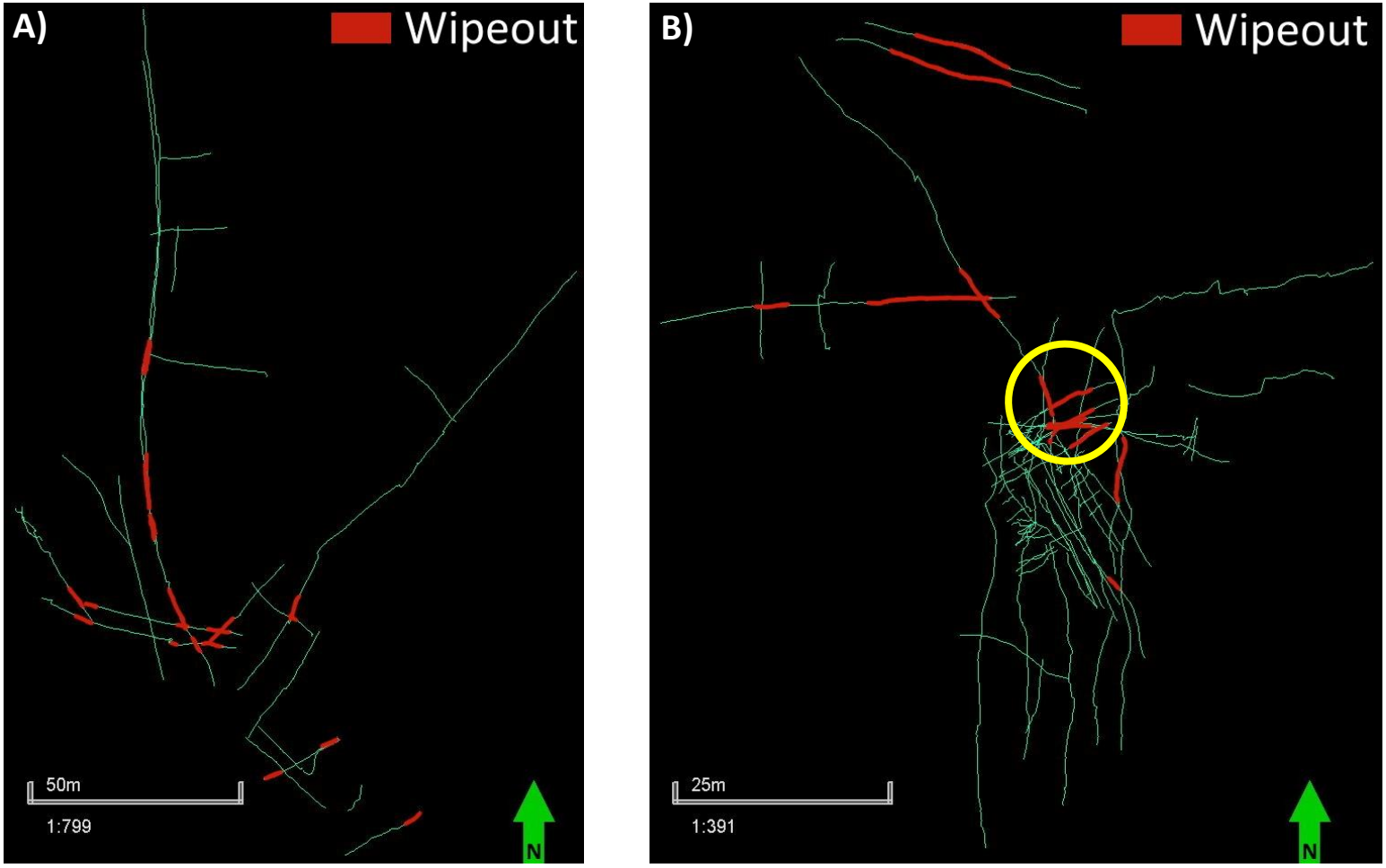

Figure 3.17: Locations of all wipeouts in A) the Upper Cemetery and B) the Middle Cemetery. It is possible to see that the same wipeout can be seen in multiple lines in some areas (circled).

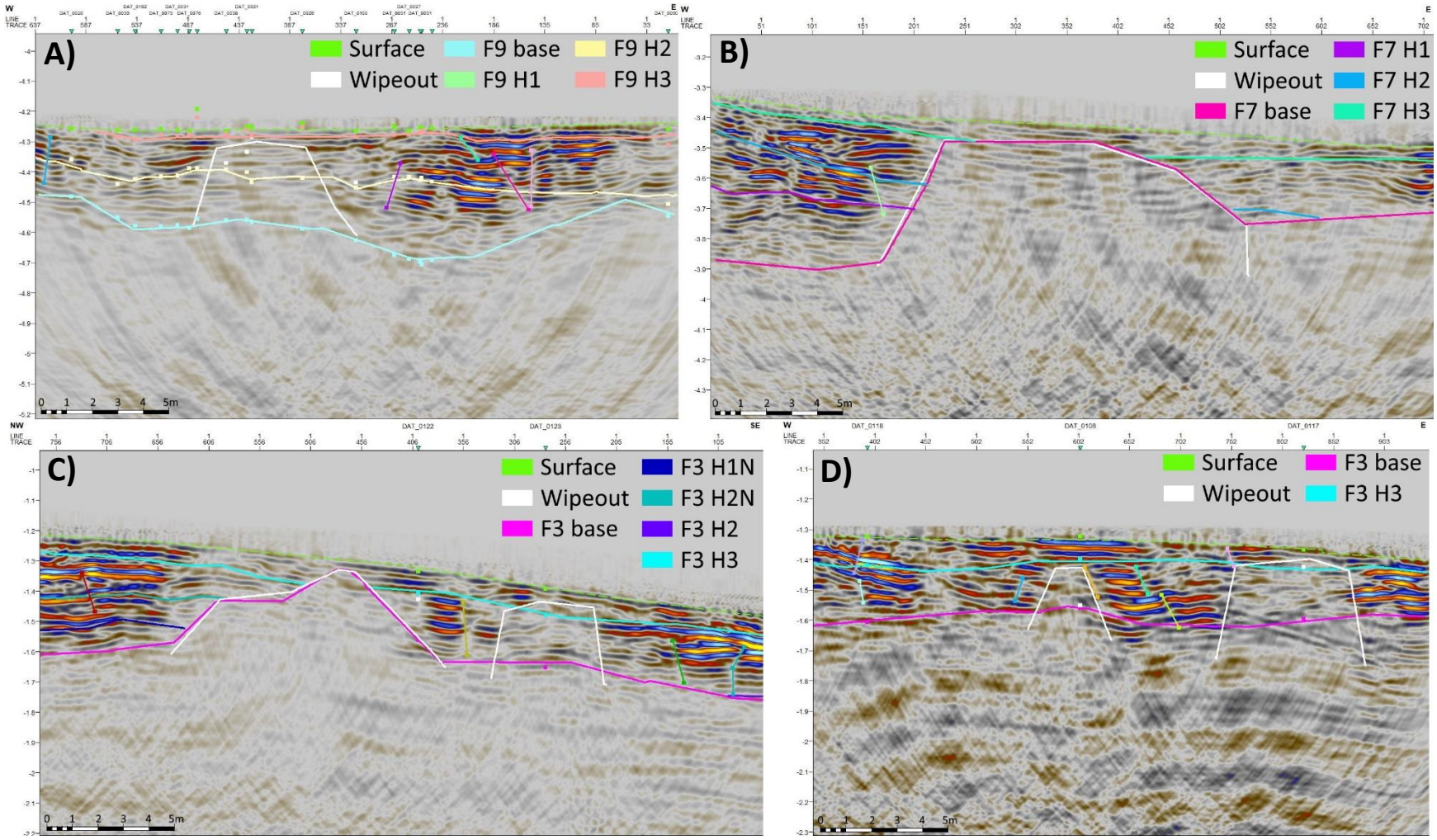

Figure 3.18: Examples of wipeouts. A) line DAT_0031, B) line DAT_0036, C) line DAT_0108, and D) line DAT_0122.

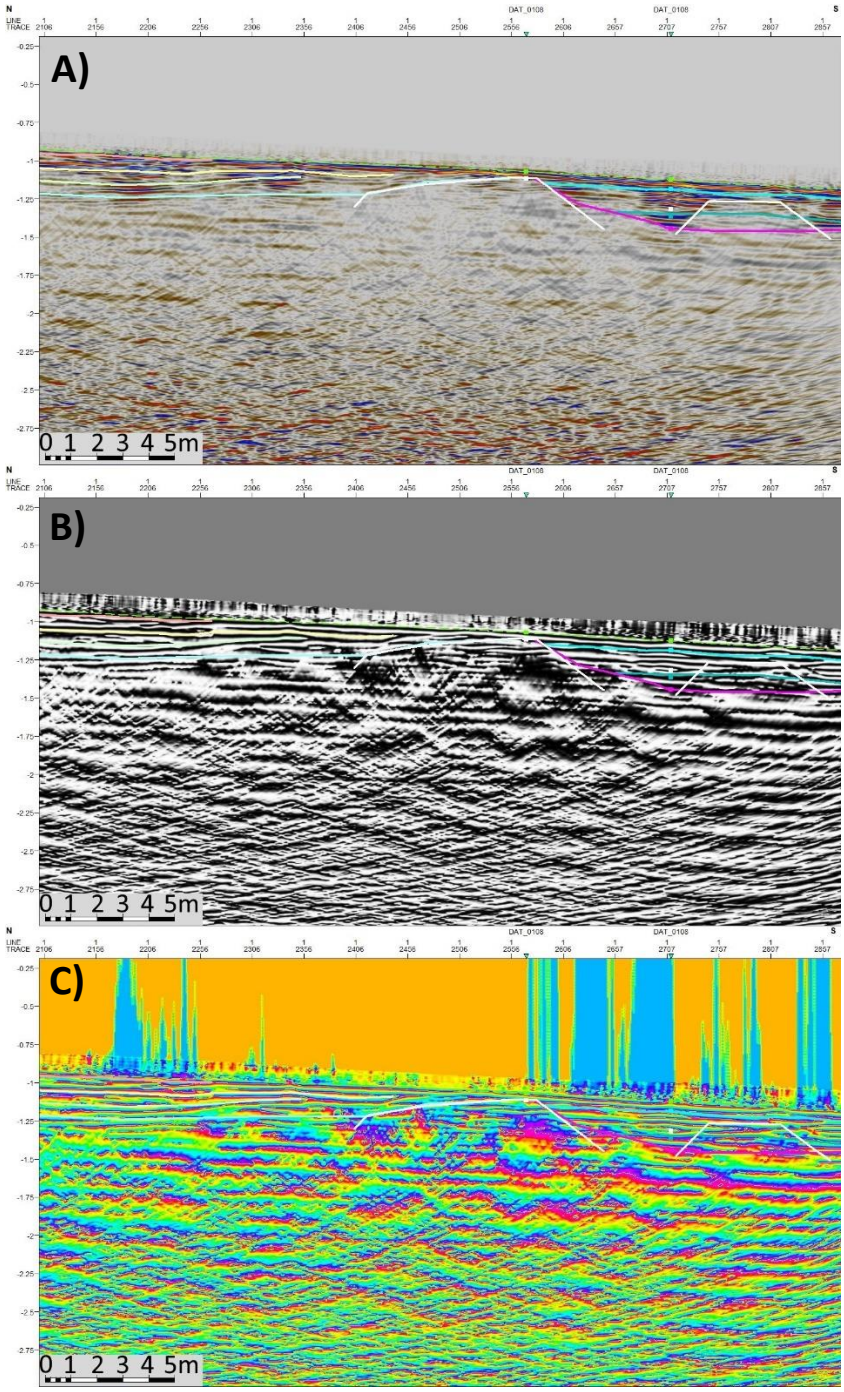

Figure 3.19: Line DAT_0109 showing wipeouts with A) no attributes, B) the cosine of phase attribute, and C) the instantaneous phase attribute. It is possible to trace reflectors across the smaller wipeout to the right, but only when using the attributes.

When overlaying wipeout locations with locations of tombs on a satellite image, it is possible to see that in the Middle Cemetery (Figure 3.20), some of the aforementioned wipeouts correlate with the location of the chamber of tomb 8, while most wipeouts are in between tombs 8, 9, and 15. In the Upper Cemetery (Figure 3.21), there is one collection of wipeouts where the two roads meet, and another to the west of the N-S road. These two locations may be of some interest for future investigation.

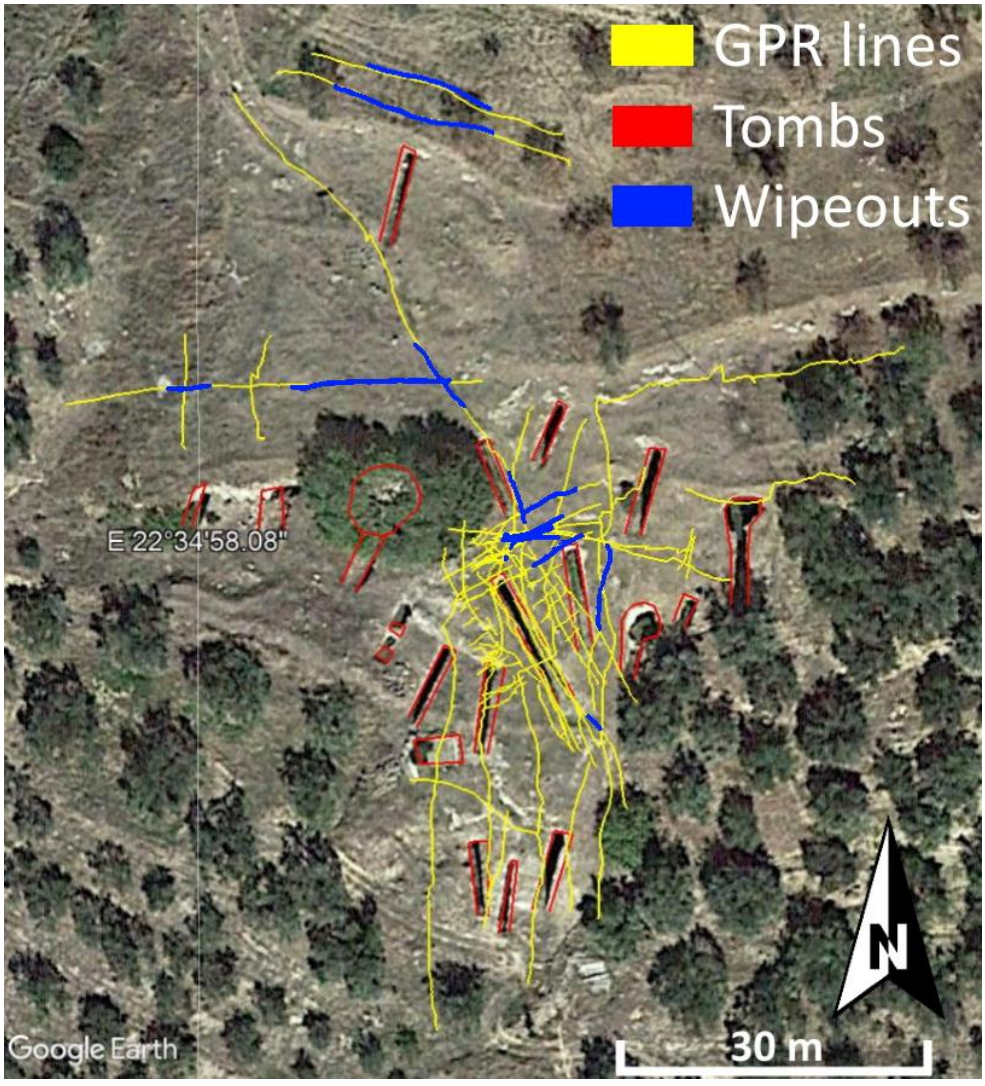

Figure 3.20: Overlay of GPR lines, tomb locations, and wipeouts in the Middle Cemetery. Satellite imagery from Google Earth, 2013.

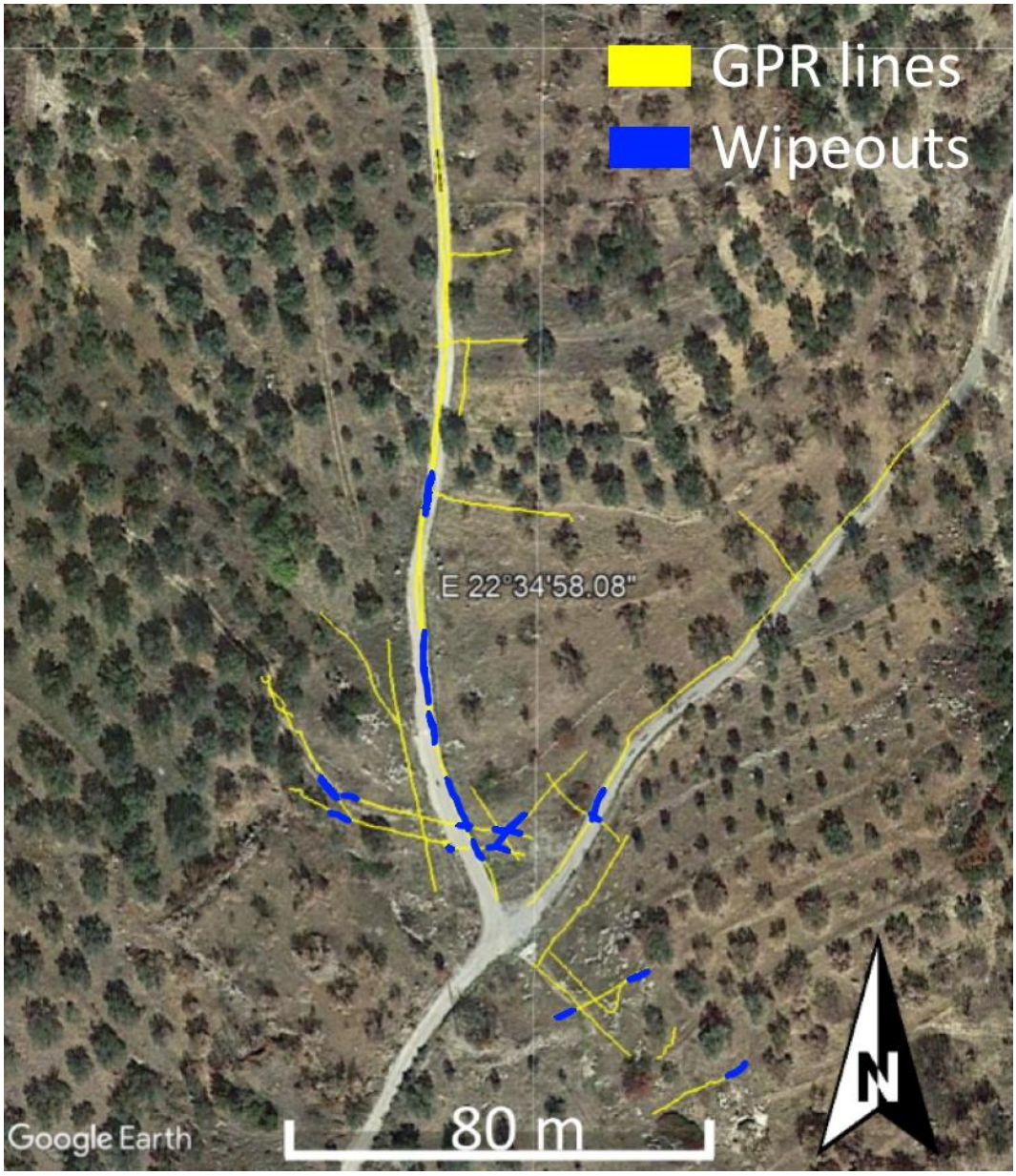

Figure 3.21: Overlay of GPR lines and wipeouts in the Upper Cemetery. Satellite imagery from Google Earth, 2013.

A very clear wipeout can be seen in line DAT_0103, which is approximately 5 metres wide (Figure 3.22A). A perpendicular line DAT_0107 was acquired, but this line shows completely different characteristics to DAT_0103. Here, in the area where the wipeout would be, an area of very strong signal is present (Figure 3.22B), with a width of approximately 2 metres. The location of this artefact is shown in Figure 3.22C. This kind of behaviour could be caused by some kind of pipe in the subsurface, or a material that blocks EM waves in one direction but amplifies them in the perpendicular direction. It is likely not a geological structure, but rather an anthropogenic artefact.

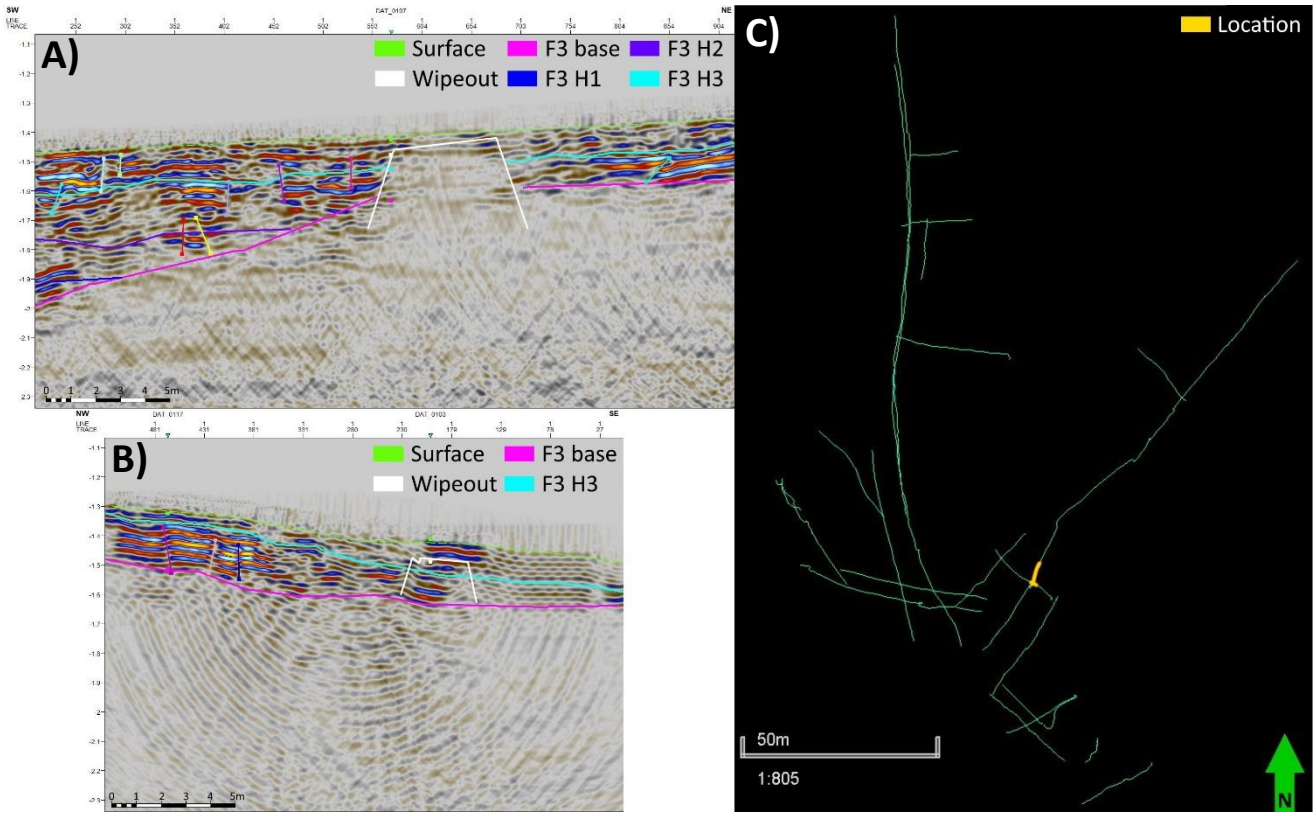

Figure 3.22: A) Wipeout in line DAT_0103, B) strong signal in line DAT_0107, and C) the location of this artefact.

There are several types of artefacts present in the data. The most prominent is migration noise that presents as “smiling” hyperbolae in the bottom of the data (Figure 3.23). Every line has this kind of noise present; however, some lines have stronger response than others. Discarded lines had especially strong response in the lower portions containing noise. In some areas, the noise happens where there is very strong signal in the continuous reflectors, like in line DAT_0107, as shown in Figure 3.23B.

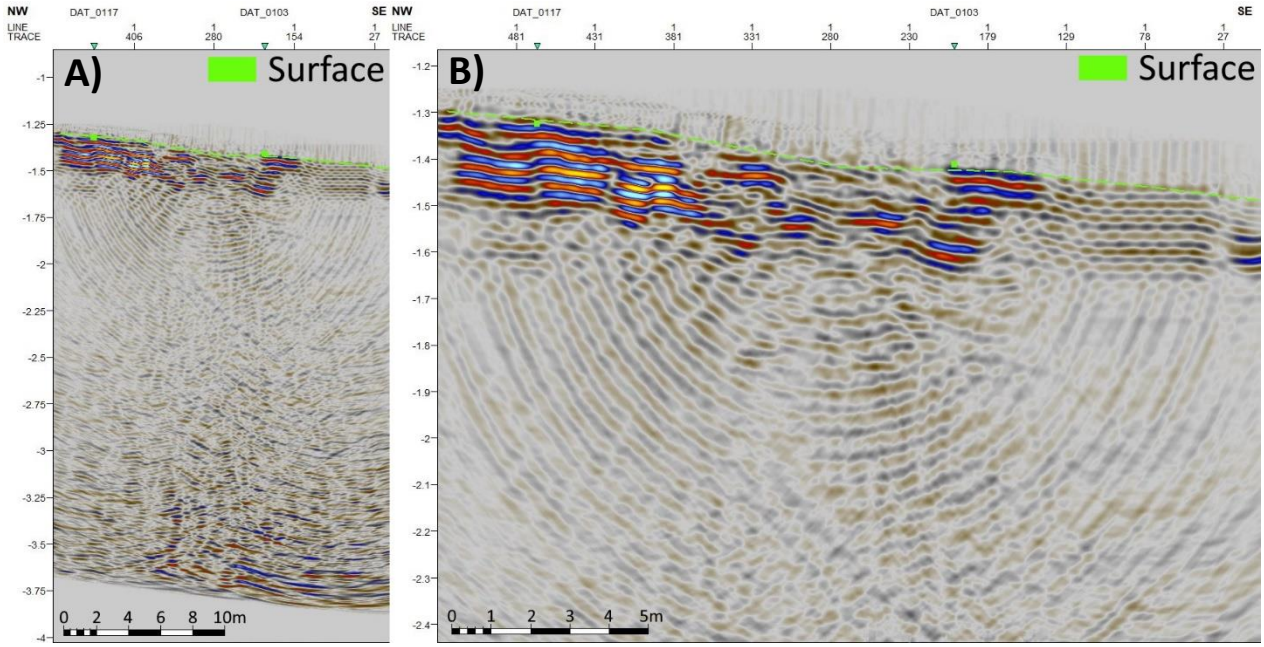

Figure 3.23: A) post-processing noise in line DAT_0107. B) a zoom to the noise caused by high amplitude.

Another kind of noise affecting the data is multiples, that happen in areas where there is especially strong signal. The strong signal is repeated deeper in the data at equal intervals, making it very apparent that it is a multiple. A great example of this is line DAT_0030, which has very prominent multiples in one portion of the line as seen in Figure 3.24. These multiples may be caused by outcropping rock, as compared to a more soily surface otherwise.

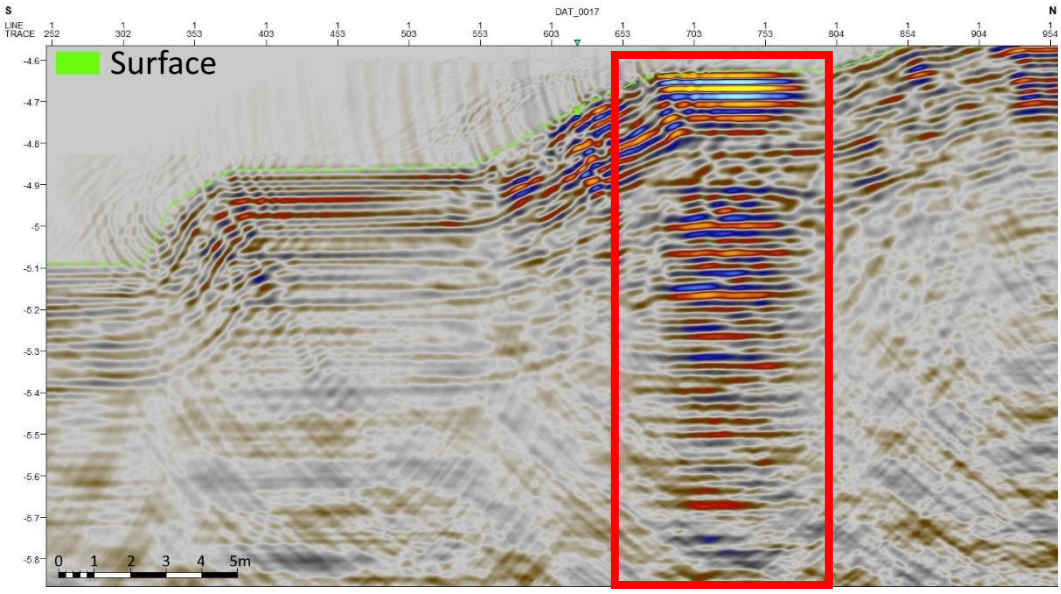

Figure 3.24: Prominent multiples shown in line DAT_0030.

Line DAT_0026 can be seen to exhibit an artefact that clearly connects to acquisition. In Figure 3.25C, it is possible to see the location of the artefact in the line, which connects it to a sudden change in the direction of acquisition. The artefact itself is shown in Figure 3.25B. This behaviour of the data could be caused during processing and affected by the inaccuracy of the internal GPS of the GPR antenna.

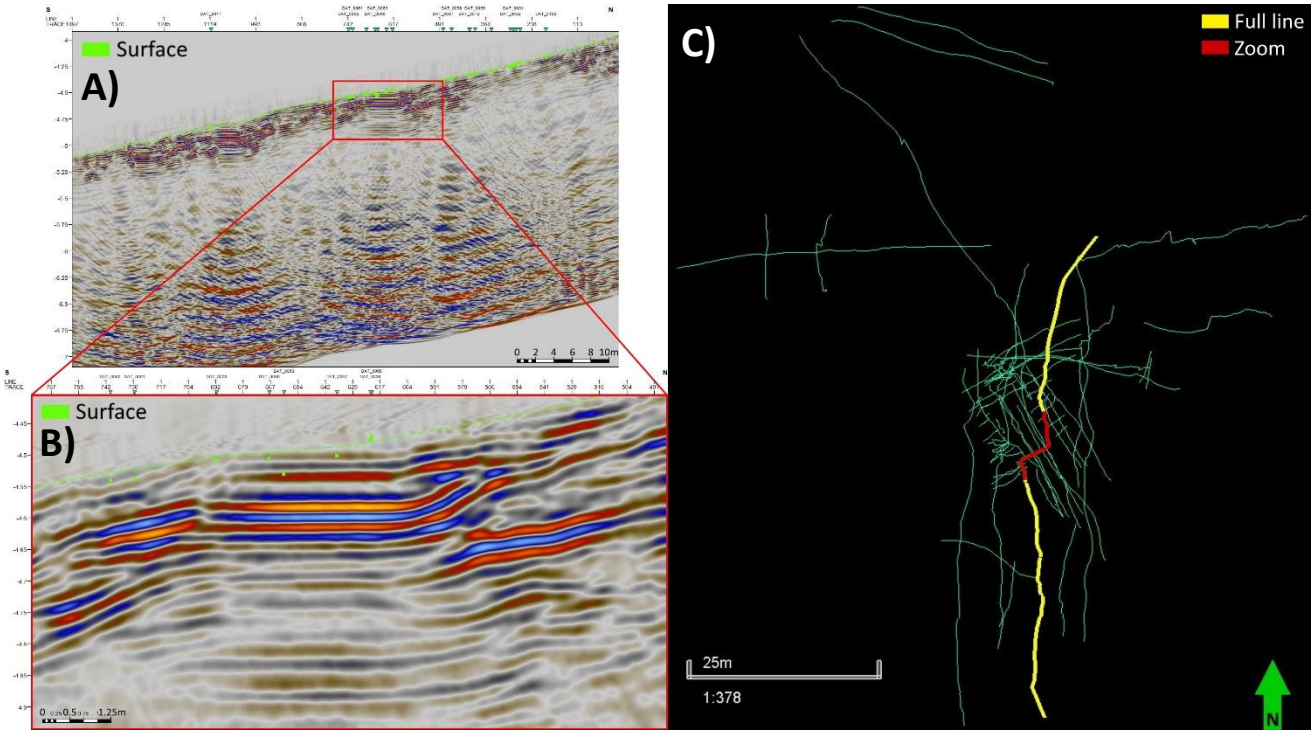

Figure 3.25: Line DAT_0026 showing an artefact related to a change of direction of acquisition. A) shows the full line, B) zooms to the artefact, and C) shows the location of the full line and zoom.

Line DAT_0030 appears to be a special case in the dataset. It contains the aforementioned multiples, while also having a strange elevation profile even using the smoothed DTM. The artefacts in elevation do not appear to be caused by other factors like a change in the direction of acquisition, as is the case with line DAT_0026. Line DAT_0030 can be seen in Figure 3.26. However, this line was collected in an area where the slope angle changed from very steep to almost flat at times, and the DTM likely reflected this, which caused the data to appear abnormal. This line also contains a high amount of migration noise in the form of “smiles” in the lower half of the line.

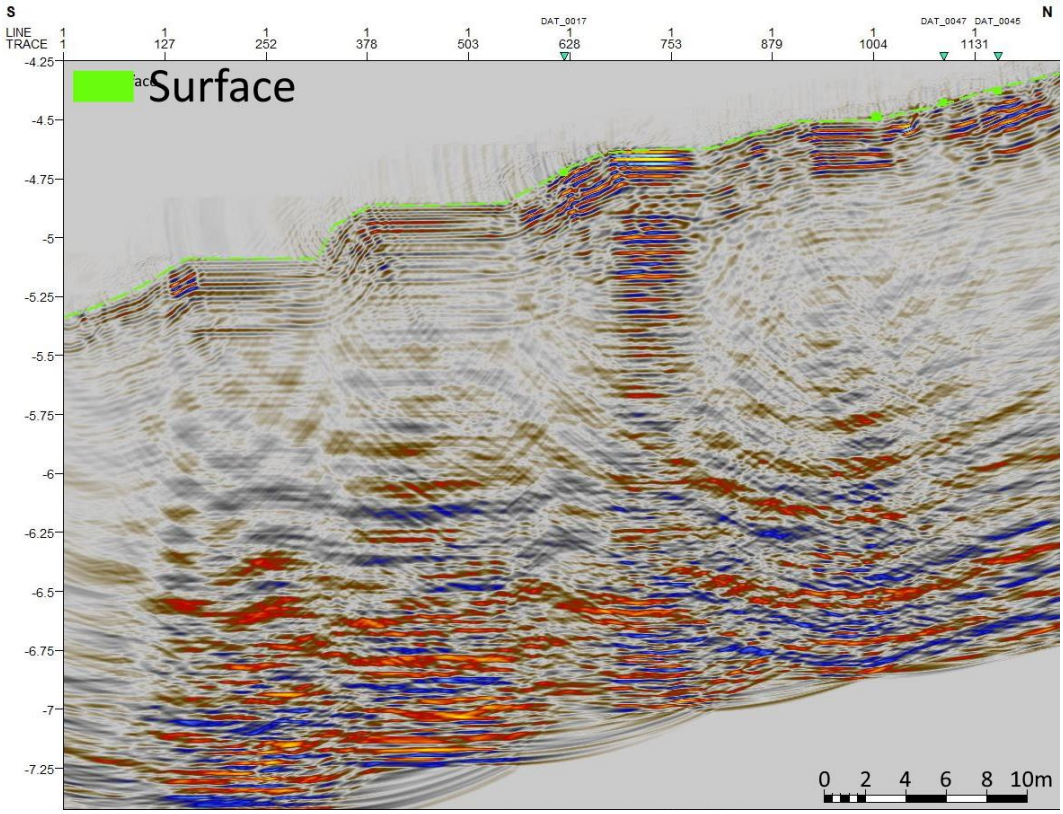

Figure 3.26: Line DAT_0030, exhibiting a strange, almost stepped elevation even post-smoothing. There are also strong multiples and a high amount of post-processing noise.

An artefact that may be either difficult to spot or can be misinterpreted as an offset, is the pause in acquisition. It is possible to distinguish pauses in acquisition to offsets as the artefact spans through the entirety of the data and is a distinct, vertical line, as seen in Figure 3.27. This could also be an artefact created during processing, as there are some lines that were paused during acquisition that do not exhibit this type of behaviour, while some lines that were not paused during acquisition appear to have been paused.

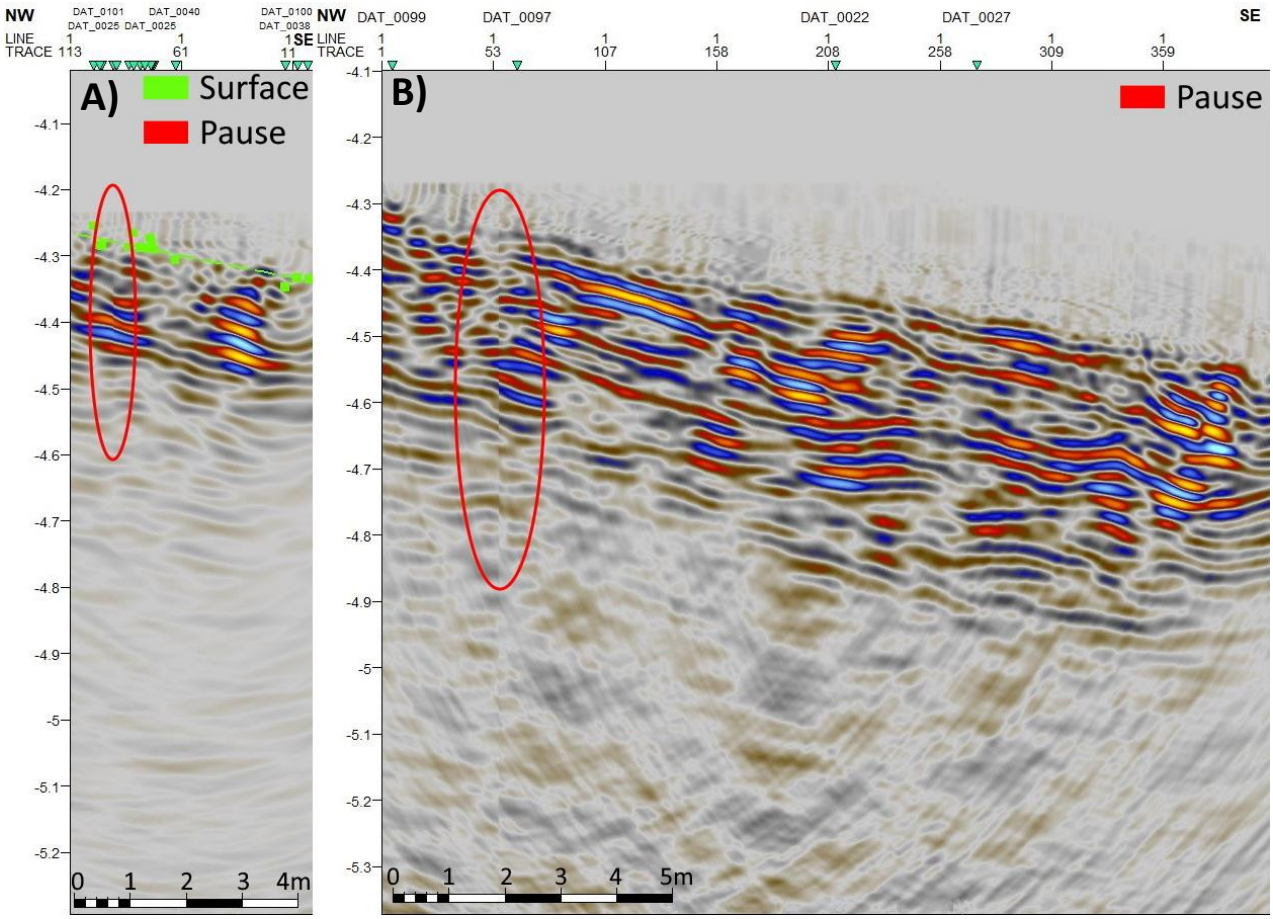

Figure 3.27: Examples of a pause in acquisition. A) shows line DAT_0069, while B) shows line DAT_0073.

An artefact that was noticed already during acquisition is a narrow area of stronger signal, which can be correlated directly to an outcropping rock amidst more soily ground. This was found in line DAT_0114 in the Upper Cemetery (Figure 3.28) and a similar artefact was also observed in line DAT_0115. It is possible that other lines in the dataset also show this type of artefact, but that was not noticed during acquisition and overlooked during interpretation.

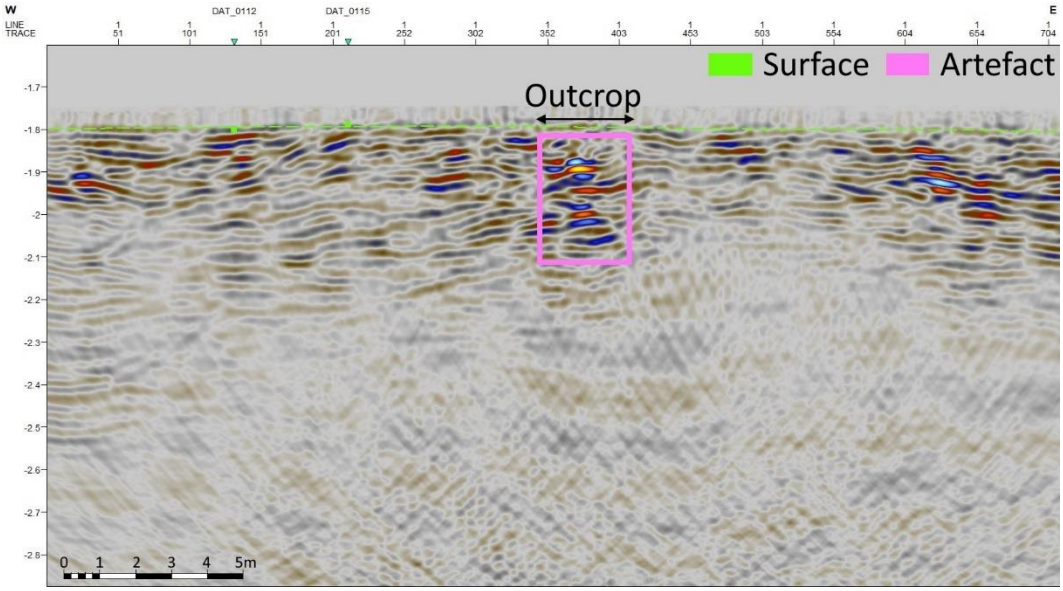

Figure 3.28: Line DAT_0114 showing an area with stronger signal that correlates with an outcropping rock in more soily ground.

4 Discussion

Thanks to the combination of geological field mapping and GPR data, it was possible to study the geology of the study area in detail. Without the use of non-invasive exploration techniques, it would be difficult to determine the geological dip angle and direction in the Aidonia Cemetery. The objective was to implement a workflow based on the use of GPR to study the subsurface in the cemetery, which was done to a certain extent. There were however many unknowns and issues that can be addressed if a similar study were to be conducted in the future.

One of these issues is that there is a lack of outcrops in the surrounding areas, mainly because of the shape of the terrain and the presence of the olive grove and other vegetation. When investigating the areas around the cemetery, there were many smaller blocks of conglomerate that did not appear to be in-situ. This, coupled with soil covering any outcrops, made it very difficult to pinpoint contacts between lithologies accurately, which means that in some areas a contact needed to be estimated between two outcrops that were located a distance from each other. In addition, the geological units in the area have not been studied in detail and there could be significant lithological differences in the area. Collecting samples in future studies would be beneficial for the understanding of the lithologies and their petrophysical properties like porosity, permeability, etc.

Another issue is the internal GPS of the GPR antenna; the z-coordinate was the most inaccurate of them all, but the elevation was possible to adjust thanks to the data provided by the Nemea Center for Classical Archaeology that was used to create a DTM. However, the x- and y-coordinates are also not accurate, as seen when displaying a shapefile of the data on a satellite image of the cemetery. This cannot be fixed in processing, so the best alternative would be to use an external GPS like an RTK GPS antenna in future studies to ensure better coordinate accuracy.

The study area lies in the outer flank of the Corinth Gulf rift, meaning that there is tectonic activity. Geological maps (Tataris et al., 1970; Paraskevopoulos et al., 1990) of areas

surrounding the study area show a multitude of large-scale faults, and investigation with GPR has revealed smaller-scale faults of different sizes, orientations, and throws. There are even miniature horsts and grabens present in the data, as seen in figures 3.15, 7.3, and 7.4. The amount of these, as well as fractures with no offset, shows that the study area was seriously affected by tectonic activity. It even is possible that multiple instances of tectonic activity have happened locally. This means that softer, less consolidated rocks in the study area can become more unstable over time as compared to the harder, more consolidated rocks. This could be one of the reasons for the collapse of the tombs in the eastern side of the Middle Cemetery. Another reason could be the softness of the rock in itself coupled with the thickness of the roof of the chambers.

A problem in this project is the high absorption of EM waves in the area. 26 lines were discarded due to very little information and a lot of noise present in the data. One of the unknowns in this issue is the velocity; a soil velocity was estimated at 130 m/µs during acquisition, but during processing it was set to 80 m/µs as this yielded best results, even in the lines that only showed the surface and noise below. During processing it is possible to implement a high-pass filter to eliminate any low frequency noise, which could be part of the problem in these lines. After using a high-pass filter it could be possible to use attributes such as cosine of phase or instantaneous phase to examine if there are in fact any continuous reflectors below the surface in these lines. Due to time constraints, this was not attempted in this project but can be attempted in the future.

In addition, the code used during processing allowed only for the use of one velocity value for migration of the data; a more accurate model could be created by using different migration velocities depending on lithology. However, this is a problem due to the limited geological knowledge of the subsurface in the study area, and it would be difficult to determine which lithology has what migration velocity when one does not know which lithology is present.

The study area is located in an olive grove. These trees are well suited to grow in dry conditions, but to yield good fruit they need to receive enough water (Thullier, 2013). This results in irrigation systems that transport water to the olive grove to allow for optimal growth. This affects the subsurface, as the irrigation systems require pipes, often metal or rubber, to transport the water. The presence of water in the subsurface affects the GPR acquisition, as water is highly conductive and creates wipeout zones like those seen in the dataset. In addition, the tombs with softer infill often collected water easier than the surrounding rock, which sometimes caused trees to grow directly above a chamber, as is the case with one of the new discoveries from 2019.

Features 5 and 6, located in lines DAT_0124 and DAT_0127 (Figure 12) respectively in the dataset exhibit unusual characteristics in comparison to the remainder of the data. There is approximately 50 metres between these two lines, yet they exhibit the same pattern: they are both at a depth of approximately 4 metres; in the west, they follow the dip of the surface, but in the east they start dipping eastward with an estimated dip of 5-10°. Because of the distance between these lines, it is possible to rule out tree roots as the cause of this behaviour. There is not a lot of data above nor below the features, which could be due to high water saturation or other properties that make for high absorption of EM waves. Because the feature is only three to four reflectors thick, it can either be an indication of another lithological layer, or possibly rubber pipes used as part of the irrigation system. In future studies, it would be beneficial to explore this area further to gain more understanding of what these features represent.

When investigating data acquired above known chambers of tombs, like tomb 8 or tomb 9, it should be possible to see the typical behaviour of EM waves in a void. This would appear as a much stronger signal, coupled with hyperbolae on the width of the void that indicate a difference in the velocity (Thitimakorn et al., 2016). However, this behaviour was not seen in the data; on the contrary, wipeout zones in multiple lines across tomb 8 were seen, correlating approximately to the location of the chamber. During acquisition, it was sometimes possible to see a low-amplitude hyperbola on the portable computer;

however, when reviewing pre-processed data on RadExplorer and MATLAB, the data does not reflect this. Processing did not improve the void detection either, but maybe this could be possible with the use of high-pass filter. A possibility could be to investigate this with a higher-frequency antenna to increase the resolution; the issue with this is the already shallow penetration depth with a lower-frequency antenna, which would mean that the high-frequency antenna would likely penetrate even shallower.

Because of both the issue with the GPS coordinate accuracy and the lack of typical behaviour for detection of voids in the GPR data, it was not possible to create a geophysical characterisation of tomb 9, which was attempted in this study. As stated previously, it could be possible to improve the GPS coordinate accuracy by using an external GPS antenna like an RTK antenna, while the resolution could be increased by using a higher-frequency GPR antenna. However, as stated earlier, the high absorption of EM waves in the area would likely restrict the penetration of the high-frequency GPR antenna. It could be beneficial to attempt this in future studies to create an accurate geophysical characterisation of tomb 9, or any other tomb where this is possible.

Lines DAT_0108 and DAT_0109 were acquired on the same stretch of road in the Upper Cemetery. However, they appear slightly different. Line DAT_0108 has much weaker signal as compared to line DAT_0109, as seen in Figure 4.1. These lines are on an incline and were acquired in opposite senses, which means one line was acquired uphill while the other was acquired downhill; because of the slope angle and the weight of the antenna, it is slower to acquire data uphill rather than downhill, meaning the speed of acquisition of these two lines was different. This could mean that there is an “ideal” speed of acquisition that gives stronger signal response, since it is known that the lines were acquired in the same area and the subsurface did not change between acquiring the data.

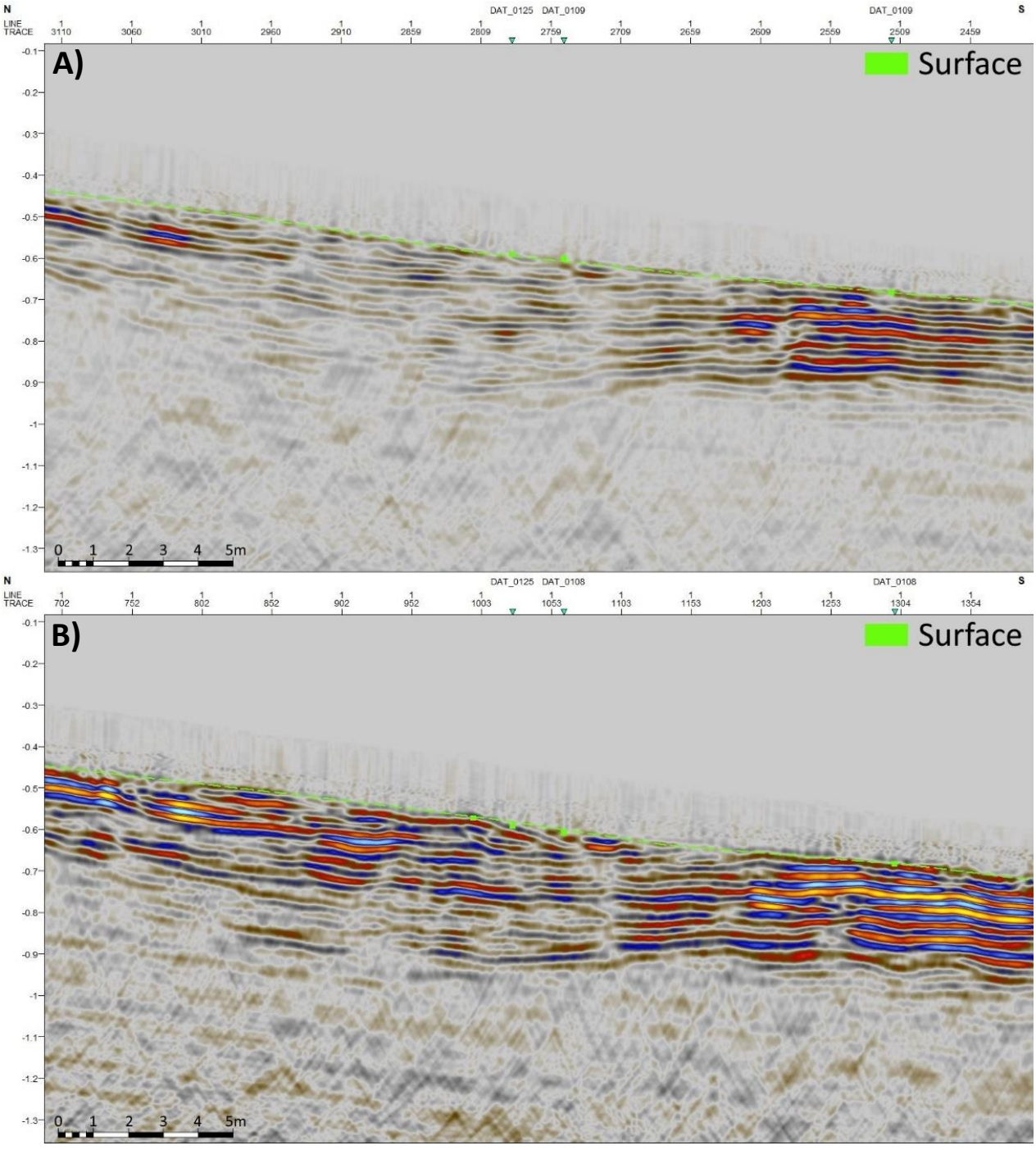

Figure 4.1: A comparison of lines DAT_0108 and DAT_0109. Both lines were acquired following the same direction (N-S), but with different senses: A) shows line DAT_0108, acquired south to north (uphill), while B) shows line DAT_0109, acquired north to south (downhill).

Thickness maps of the horizons in Feature 9 were created to gain more information about these rock layers. Because of the aforementioned differences in velocity between acquisition (130 m/μs) and processing (80 m/μs), the thicknesses are not accurate, and they should be at least doubled. Because of time constraints, thickness maps were only created for Feature 9. It would be beneficial to create these for all features to learn more about the structure of these layers in the subsurface.

Something that was noticed after interpretation was finalised, is the GPS positioning of the data. A shapefile of the GPR dataset was imported into the Petrel project, when observing the interpreted dataset and shapefile together it is possible to see that the interpreted dataset is shifted southwest from the “true” positioning of the data (Figure 4.2). The reason for this is most likely a problem in the processing code, where the GPS coordinates may be of different precision, meaning the decimal point is shifted. This would be an easy fix, where a line of code could be added to multiply the coordinates by the required value to shift the decimal point to its correct location. There is also a possibility that a different datum or ellipsoid was used during projection of coordinates.

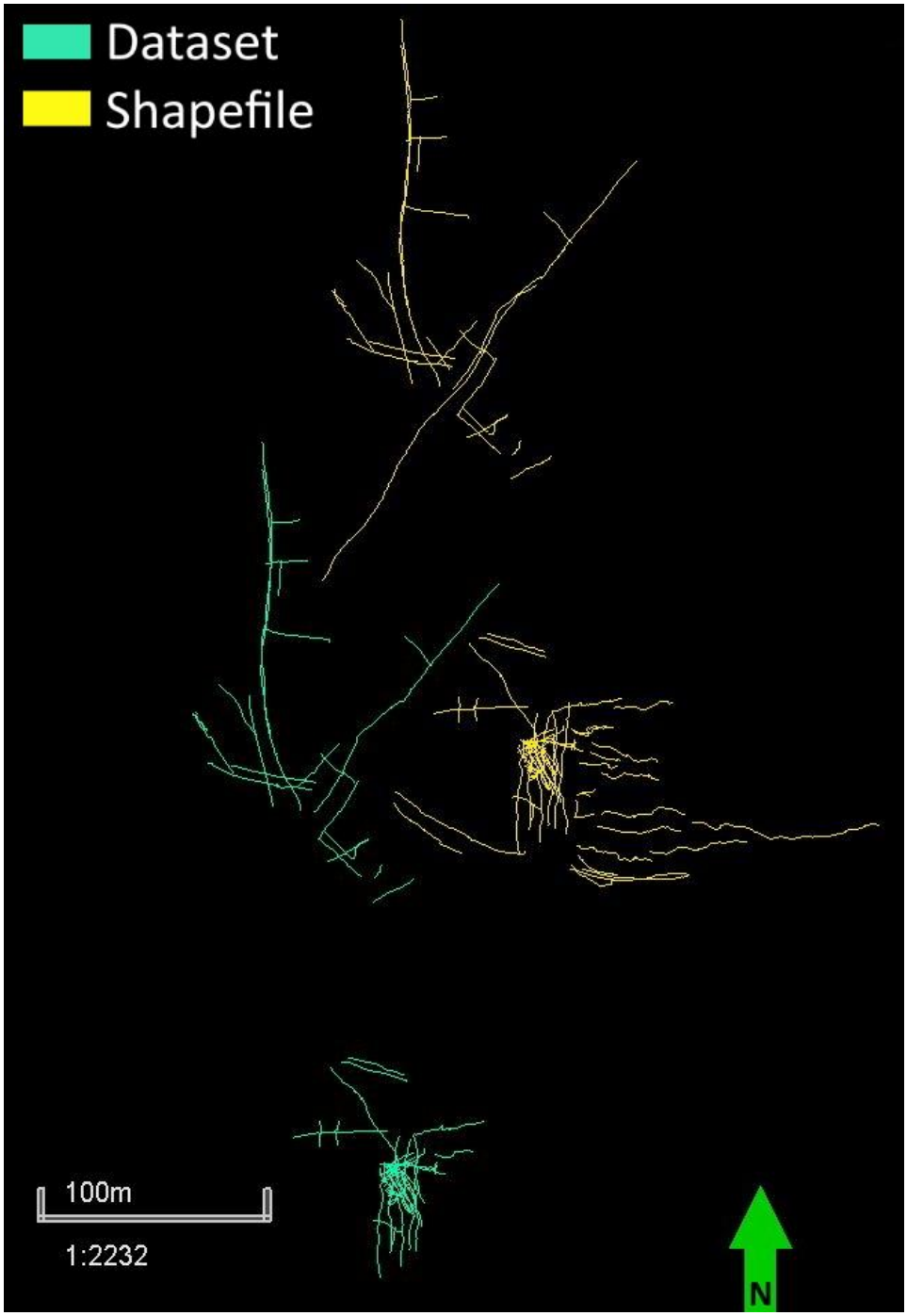

Figure 4.2: The interpreted dataset and shapefile displayed together in Petrel. It is clear that the interpreted dataset is shifted to the southwest, most likely due to a problem in the processing code.

5 Conclusion

This study was conducted in the Mycenaean Cemetery of Aidonia to investigate the subsurface using geological mapping and GPR as a non-invasive exploration method. The area, which has been excavated by archaeologists since the late 1970s, has not been studied in terms of geology prior to this study.

In addition to collecting geological data from the areas surrounding the cemetery and creating a geological field map, a GPR survey consisting of 115 lines was acquired in the Middle and Upper Cemetery. The final GPR dataset consisted of 89 lines in the Middle and Upper Cemetery, while the geological field data was collected in 36 stations and 65 control points.

The geological field map differentiated between four different units and six different lithologies, showing that diagenetic limestones are present in the cemetery as well as lacustrine marls and conglomerates. The north and northwest of the study area is a fluvial conglomerate, coming most likely from braided channels, while the southeast of the study area is covered by Quaternary alluvial deposits.

A workflow for the processing of GPR data in MATLAB was provided in this project, which was utilised instead of RadExplorer. The main reason for this was that MATLAB automated processing in all lines simultaneously, while RadExplorer required interactive processing of each individual line, which was extremely time-consuming, especially when the processing required trial and error.

The GPR data collected shows a high absorption of EM waves and a maximum penetration depth of about 8 metres. The areas with continuous reflectors in the data were interpreted as features, and the dataset contains a total of nine of these features, six of which are in the Upper Cemetery and three in the Middle Cemetery. Most features had an interpreted base, which was an arbitrary horizon marking the bottom of the interpretable data, and three horizons spread throughout the feature. The exceptions are features F3, F5, and F6; F5 and F6 were both a single horizon with unusual characteristics

compared to the rest of the dataset, while F3 had two extra horizons in an area separated by a wipeout where it was possible to trace the topmost reflector across. There were over 400 small-scale faults, or offsets, interpreted throughout the data, of which some may be connected into faults spanning across multiple lines. There was a number of artefacts observed in the data, for example wipeout zones, pauses in acquisition, a difference in signal strength depending on the speed of data acquisition, and more.

The main objective of this study was to implement a workflow based on the use of GPR to study the subsurface of the Aidonia Cemetery and distinguish shallow geological features versus archaeological artefacts. This was achieved; however, it was challenging to notice voids of known and excavated tombs, possibly due to the resolution or processing of the data.

The second objective was to observe any possible artefacts in the data and investigate if these could be undiscovered archaeological artefacts that could be investigated in the future. The focus here was the Upper Cemetery, where multiple wipeouts were interpreted. These wipeouts can indicate anything from higher water saturation to a softer infill; when the wipeout zone was seen in two lines perpendicular to each other, it is worth examining further in future studies.

A geophysical characterisation of tomb 9 was attempted in this project, however due to issues with the internal GPS of the GPR antenna and problems with void detection, this was unfortunately not possible. It would be advantageous to focus on this in the future, possibly using a higher-frequency GPR antenna for higher resolution and an external GPS antenna for higher coordinate accuracy.

For future studies in this area, it would be beneficial to further investigate the geology and apply for a permit allowing the collection of samples; these could yield useful information about the petrophysical properties of the lithologies in the area, giving a greater understanding of the subsurface. It would also be beneficial to conduct another GPR survey, as stated above, to properly characterise tomb 9 or another tomb where this

is possible. Another thing that can be attempted in future studies is the implementation of high-pass filters to eliminate low-frequency noise, which rendered many of the discarded lines uninterpretable.

6 References

Abouhamad, M., T. Dawood, A. Jabri, M. Alsharqawi, and T. Zayed, 2017, Corrosiveness mapping of bridge decks using image-based analysis of GPR data: Automation in Construction, v. 80, p. 104–117, doi:10.1016/j.autcon.2017.03.004.

Alcantara Rodriguez, M. A., 2018, Ground penetrating radar and seismic study to determine glacial deposit stratigraphy, Master's thesis: University of Stavanger, Norway, 86 p.

Anbazhagan, P., M. Bittelli, R. R. Pallepati, and P. Mahajan, 2020, Comparison of soil water content estimation equations using ground penetrating radar: Journal of Hydrology, v. 588, doi:10.1016/j.jhydrol.2020.125039.

Annan, A. P., 2002, GPR—History, Trends, and Future Developments: Subsurface Sensing Technologies and Applications, v. 3, no. 4, p. 253–270, doi:10.1023/A:1020657129590.

Annan, A. P., 2005, 11. Ground-Penetrating Radar, *in* Near-Surface Geophysics: Society of Exploration Geophysicists, Investigations in Geophysics, p. 357–438, doi:10.1190/1.9781560801719.ch11.

Archaeology Wiki, 2019, Two unplundered tombs discovered at Aidonia cemetery.

Bachrach, R., and J. Rickett, 1999, Ultra shallow seismic reflection in depth: Examples from 3D and 2D ultra shallow surveys with application to joint seismic and GPR imaging, *in* SEG Technical Program Expanded Abstracts 1999: Society of Exploration Geophysicists, SEG Technical Program Expanded Abstracts, p. 488–491, doi:10.1190/1.1821060.

Booth, A. D., A. Mercer, R. Clark, T. Murray, P. Jansson, and C. Axtell, 2013, A comparison of seismic and radar methods to establish the thickness and density

of glacier snow cover: Annals of Glaciology, v. 54, no. 64, p. 73–82, doi:10.3189/2013AoG64A044.

Borchert, O., 2019, History of Ground Penetrating Radar (GPR): <https://www.obonic.de/en/article/ground-peentrating-radar-history/> (accessed April 7, 2020).

Čermák, J., J. Hruška, M. Martinková, and A. Prax, 2000, Urban tree root systems and their survival near houses analyzed using ground penetrating radar and sap flow techniques: Plant and Soil, v. 219, no. 1–2, p. 103–116.

Chrysopoulos, P., 2018, Unlooted Ancient Tomb found in Mycenae (Photos) | GreekReporter.com.

Conyers, L. B., 2013, Ground-Penetrating Radar for Archaeology: AltaMira Press, 260 p.

Cook, J. C., 1976, Radar exploration through rock in advance of mining: Trans. Society Mining Engineers, AIME, v. 254, p. 140–146.

Coon, J. B., J. C. Fowler, and C. J. Schafers, 1981, Experimental uses of short pulse radar in coal seams: Geophysics, v. 46, no. 8, p. 1163–1168, doi:10.1190/1.1441256.

Davis, J. L., and A. P. Annan, 1989, Ground-Penetrating Radar for High-Resolution Mapping of Soil and Rock Stratigraphy: Geophysical Prospecting, v. 37, no. 5, p. 531–551, doi:10.1111/j.1365-2478.1989.tb02221.x.

Dawood, T., Z. Zhu, and T. Zayed, 2020, Deterioration mapping in subway infrastructure using sensory data of GPR: Tunnelling and Underground Space Technology, v. 103, doi:10.1016/j.tust.2020.103487.

Dolphin, L. T., W. B. Beatty, and J. D. Tanzi, 1978, Radar probing of Victorio Peak, New Mexico: Geophysics, v. 43, no. 7, p. 1441–1448, doi:10.1190/1.1440906.

Evans, S., 1963, Radio techniques for the measurement of ice thickness: Polar Record, v. 11, no. 73, p. 406–410, doi:10.1017/S0032247400053523.

Fisher, S. C., R. R. Stewart, and H. M. Jol, 1996, Ground Penetrating Radar (GPR) Data Enhancement Using Seismic Techniques: Journal of Environmental and Engineering Geophysics, v. 1, no. 2, p. 89–96, doi:10.4133/JEEG1.2.89.

Gawthorpe, R. L., M. R. Leeder, H. Kranis, E. Skourtsos, J. E. Andrews, G. A. Henstra, G. H. Mack, M. Muravchik, J. A. Turner, and M. Stamatakis, 2018, Tectono-sedimentary evolution of the Plie-Pleistocene Corinth rift, Greece: Basin Research, v. 30, p. 448–479, doi:10.1111/bre.12260.

GeoModel, 2014, What is Ground Penetrating Radar Frequently Asked Questions – GeoModel: <https://geomodel.com/methods/ground-penetrating-radar/> (accessed July 2, 2020).

Gizzi, F. T., and G. Leucci, 2018, Global Research Patterns on Ground Penetrating Radar (GPR): Surveys in Geophysics, v. 39, no. 6, p. 1039–1068, doi:10.1007/s10712-018-9475-1.

Gizzi, F. T., A. Loperte, A. Satriani, V. Lapenna, N. Masini, and M. Proto, 2010, Georadar investigations to detect cavities in a historical town damaged by an earthquake of the past, *in* Advances in Geosciences: Copernicus GmbH, p. 15–21, doi:https://doi.org/10.5194/adgeo-24-15-2010.

Goodman, D., 1994, Ground-penetrating radar simulation in engineering and archaeology: GEOPHYSICS, v. 59, no. 2, p. 224–232, doi:10.1190/1.1443584.

GTP Headlines, 2019, Nemea's Aidonia Dig Reveals Two Mycenaean Period Tombs: <https://news.gtp.gr/2019/08/21/nemeas-aidonia-dig-reveals-two-mycenaean-period-tombs/> (accessed June 30, 2020).

GuidelineGeo, 2016, Flexible GPR Solution: <https://www.guidelinegeo.com/product/mala-groundexplorer/> (accessed January 9, 2020).

GuidelineGeo, 2017, Subsurface mapping with GPR and resistivity meter: <https://www.guidelinegeo.com/solutions/case-stories/gpr-plays-important-role-unsealing-legendary-tomb-christ/> (accessed January 9, 2020).

Haaken, K., A. Furman, N. Weisbrod, and A. Kemna, 2016, Time-Lapse Electrical Imaging of Water Infiltration in the Context of Soil Aquifer Treatment: Vadose Zone Journal, v. 15, no. 11, p. vzj2016.04.0028, doi:10.2136/vzj2016.04.0028.

Holser, W. T., R. J. S. Brown, F. A. Roberts, O. A. Fredriksson, and R. R. Unterberger, 1972, Radar logging of a salt dome: Geophysics, v. 37, no. 5, p. 889–906, doi:10.1190/1.1440307.

Hruska, J., and G. Fuchs, 1999, GPR prospection in ancient Ephesos: Journal of Applied Geophysics, v. 41, no. 2–3, p. 293–312, doi:10.1016/S0926-9851(98)00048-2.

Huisman, J. A., S. S. Hubbard, J. D. Redman, and A. P. Annan, 2003, Measuring soil water content with ground penetrating radar: A review: Vadose Zone Journal, v. 2, no. 4, p. 476–491, doi:10.2113/2.4.476.

Jol, H. M., 2009, Ground Penetrating Radar Theory and Applications: Elsevier, 545 p.

Karczewski, J., Ł. Ortyl, and M. Pasternak, 2011, Zarys metody georadarowej: Kraków, Wydawnictwa AGH, 346 p.

Karkanas, P., M. K. Dabney, R. A. K. Smith, and J. C. Wright, 2012, The geoarchaeology of Mycenaean chamber tombs: Journal of Archaeological Science, v. 39, p. 2722–2732, doi:10.1016/j.jas.2012.04.016.

Kearey, P., 2002, An introduction to geophysical exploration: Oxford, Blackwell Science, viii+262 p., p. VIII, 262.

Leucci, G., L. De Giorgi, F. T. Gizzi, and R. Persico, 2017, Integrated geo-scientific surveys in the historical centre of Mesagne (Brindisi, Southern Italy): Natural Hazards, v. 86, no. 2, p. 363–383, doi:10.1007/s11069-016-2645-x.

Mustasaar, M., J. Plado, and A. Jõeleht, 2012, Determination of electromagnetic wave velocity in horizontally layered sedimentary target: A ground-penetrating radar study from Silurian limestones, Estonia: Acta Geophysica, v. 60, no. 2, p. 357–370, doi:10.2478/s11600-011-0068-3.

Paraskevopoulos, S., F. R. Lucchi, and G. G. Ori, 1990, Rilevamento e sedimentologia del bacino dell' Argolide, Plio-Pleistocene (Peloponneso): zona tra Stimfalia e Nemea (Nomos Corintos), PhD: Università degli Studi di Bologna.

Puente, I., M. Solla, S. Lagüela, and J. Sanjurjo-Pinto, 2018, Reconstructing the Roman Site "Aquis Querquennis" (Bande, Spain) from GPR, T-LiDAR and IRT Data Fusion: Remote Sensing, v. 10, no. 379, doi:10.3990/rs10030379.

Robein, E., 2010, Seismic Imaging: A Review of the Techniques, their Principles, Merits and Limitations: Houten, Netherlands, EAGE, Education Tour Series 4, 244 p.

Smith, R. A. K., M. K. Dabney, E. Pappi, S. Triantaphyllou, and J. C. Wright, 2017, Ayia Sotira : A Mycenaean Chamber Tomb Cemetery in the Nemea Valley, Greece: Philadelphia, Pennsylvania, INSTAP, Prehistory Monographs.

Steenson, B. O., 1951, Radar methods for the exploration of glaciers, PhD: California Institute of Technology, doi:Steenson, Bernard Owen (1951) Radar methods for the exploration of glaciers. Dissertation (Ph.D.), California Institute of Technology. doi:10.7907/3YY8-XC87.

https://resolver.caltech.edu/CaltechTHESIS:10092014-103732963 <https://resolver.caltech.edu/CaltechTHESIS:10092014-103732963>.

Tataris, A., N. Maragoudakis, and G. Kounis, 1970, Geological Map of Greece - Nemea Sheet, Geological Map: Institute for Geology and Subsurface Research.

Thitimakorn, T., N. Kampananon, N. Jongjaiwanichkit, and S. Kupongsak, 2016, Subsurface void detection under the road surface using ground penetrating radar (GPR), a case study in the Bangkok metropolitan area, Thailand: International Journal of Geo-Engineering, v. 7, no. 1, p. 2, doi:10.1186/s40703-016-0017-8.

Thullier, F., 2013, The irrigation of the olive tree improves fruit production, in terms of quantity and quality | Irrigazette: <https://irrigazette.com/en/news/irrigation-olive-tree-improves-fruit-production-terms-quantity-and-quality> (accessed July 12, 2020).

Wessel, P., and J. F. Luis, 2017, The GMT/MATLAB Toolbox: Geochemistry, Geophysics, Geosystems, v. 18, no. 2, p. 811–823, doi:10.1002/2016GC006723.

Xie, P., H. Wen, P. Xiao, and Y. Zhang, 2018, Evaluation of ground-penetrating radar (GPR) and geology survey for slope stability study in mantled karst region: Environmental Earth Sciences, v. 77, no. 4, p. 122, doi:10.1007/s12665-018-7306-9.

Yu, Y., A. Klotzsche, L. Weihermüller, J. A. Huisman, J. Vanderborght, H. Vereecken, and J. van der Kruk, 2020, Measuring vertical soil water content profiles by combining horizontal borehole and dispersive surface ground penetrating radar data: Near Surface Geophysics, v. 18, no. 3, p. 275–294, doi:10.1002/nsg.12099.

Zhao, W., E. Forte, M. Pipan, and G. Tian, 2013, Ground Penetrating Radar (GPR) attribute analysis for archaeological prospection: Journal of Applied Geophysics, v. 97, p. 107–117, doi:10.1016/j.jappgeo.2013.04.010.

7 Appendices

7.1 Appendix 1: MATLAB code

This appendix contains the entire code used to process the GPR dataset, which was done in MATLAB on a Linux machine.

```
clear all

close all


% Parameters:

path =
'/nfs/ier/home/public/Ivan/For_Sylwia/GPR/Fieldtrip_Aidonia_Aug20
19/MALAGS/';

listfile = [path 'list_of_files.txt'];


FID = fopen(listfile);

list = textscan(FID,'%s');

fclose(FID);

stringData = string(list{:});

nfiles = length(stringData);


DTM = load('DTM_Ivan.txt');

F=scatteredInterpolant(DTM(:,1)*100, DTM(:,2)*100, DTM(:,3));
```

```
%%
for ind=1:nfiles
      name = char(stringData(ind));
      display(name)

      dx = 4; %cm
      dz = 4; %cm
      V = 8000; %cm/microsecond
      t0 = 30;
      datum = 40015; % cm

      filename = [path name];

      ntr = rd3info(filename, 'scans');
      ntr = ntr{1};

      dt = rd3info(filename, 'frequency');
      dt = 1/dt{1}

      %%Get coordinates
```

```
call = ["awk <" filename ".cor '{print $1}' > tmp.trc"];
call = strcat(call(:,1), call(:,2), call(:,3));
status1 = system(call);

call = ["awk <" filename ".cor '{print $6, $4}' | /bin/gmt
mapproject -Ju34N/1 -C > tmp.xy"];
call = strcat(call(:,1), call(:,2), call(:,3));
status2 = system(call);

call = ["awk <" filename ".cor '{print $6, $4}' > tmp.ll"];
call = strcat(call(:,1), call(:,2), call(:,3));
status2 = system(call);

call = ["awk <" filename ".cor '{print $8}' > tmp.z"];
call = strcat(call(:,1), call(:,2), call(:,3));
status3 = system(call);

t = load('tmp.trc');
cor = load('tmp.xy');
z = smooth(F(cor(:,1), cor(:,2)), 50);
t_i = 1:ntr;
```

```
cor_i = interp1(t, cor, t_i, 'linear', 'extrap');

z_i = interp1(t, z, t_i, 'linear', 'extrap');


%%Interpolate to regular distance

dist = zeros(1,ntr);

for i=2:ntr

      stretch = sqrt((cor_i(i,1) - cor_i(i-1,1))^2 +
      (cor_i(i,2) - cor_i(i-1,2))^2);

      if(stretch == 0)

            stretch = 1e-3;

      end

      dist(i)  = dist(i-1) + stretch;

end


dist_i = 0:dx:dist(end);


cor_id = interp1(dist, cor_i, dist_i, 'linear', 'extrap');

z_id = interp1(dist, z_i, dist_i, 'linear', 'extrap');


data = loadrd3(filename);

data_id = interp1(dist, data.', dist_i, 'linear',
'extrap').';
```

```
[Nt, Nx] = size(data_id);

t0 = t0*dt;

time = (0:Nt-1)*dt - t0;

meantrc =  mean(data_id,2);

data_id = data_id -meantrc*ones(1,Nx);

scaling = (((time).').^2)*ones(1,Nx);

data_id = data_id.*scaling;


% Convert to cm

z_id = z_id*100;


cor_xyz = [cor_id (z_id).'];

cor_mig = [dist_i.' (datum-z_id).'];

cor_dat = [cor_id ones(size(z_id.'))*datum];


%%

data_redat= redat_GPR(data_id, dt, 2*Nt, 6000, cor_xyz,
cor_dat, 500);

I = zomig_GPR2D(data_id, dt, t0, Nx, 1900, dx, dz, V,
cor_mig, 1000);
```

```
% Convert from depth to vertical time
[Nz,Nx] = size(I);

td = zeros(Nz,1);
for i=2:Nz
      td(i) = td(i-1) + 2*dz/V;
end

Itime = interp1(td, I, time, 'linear', 0);

%% WRITE SEG-Y

WriteSegy('tmp.segy',I(:,:));
[Data,SegyTraceHeaders,SegyHeader]=ReadSegy('tmp.segy');
SegyHeader.DataSampleFormat=1;
SegyHeader.dt=dz;

x0 = 0;
y0 = 0;
for i=1:Nx
      SegyTraceHeaders(i).GroupX = (cor_xyz(i,1)-x0);
```

```
            SegyTraceHeaders(i).GroupY = (cor_xyz(i,2)-y0);
            SegyTraceHeaders(i).SourceX = (cor_xyz(i,1)-x0);
            SegyTraceHeaders(i).SourceY = (cor_xyz(i,2)-y0);
            SegyTraceHeaders(i).cdpX = (cor_xyz(i,1)-x0);
            SegyTraceHeaders(i).cdpY = (cor_xyz(i,2)-y0);
            SegyTraceHeaders(i).SourceGroupScalar = -100;
        end

        WriteSegyStructure([name
        '.sgy'],SegyHeader,SegyTraceHeaders,Data);

end
```

7.2 Appendix 2: Extra figures

This appendix contains more example figures from the results section. They are all screenshots from Petrel, with a scale, legend, and direction of the line.

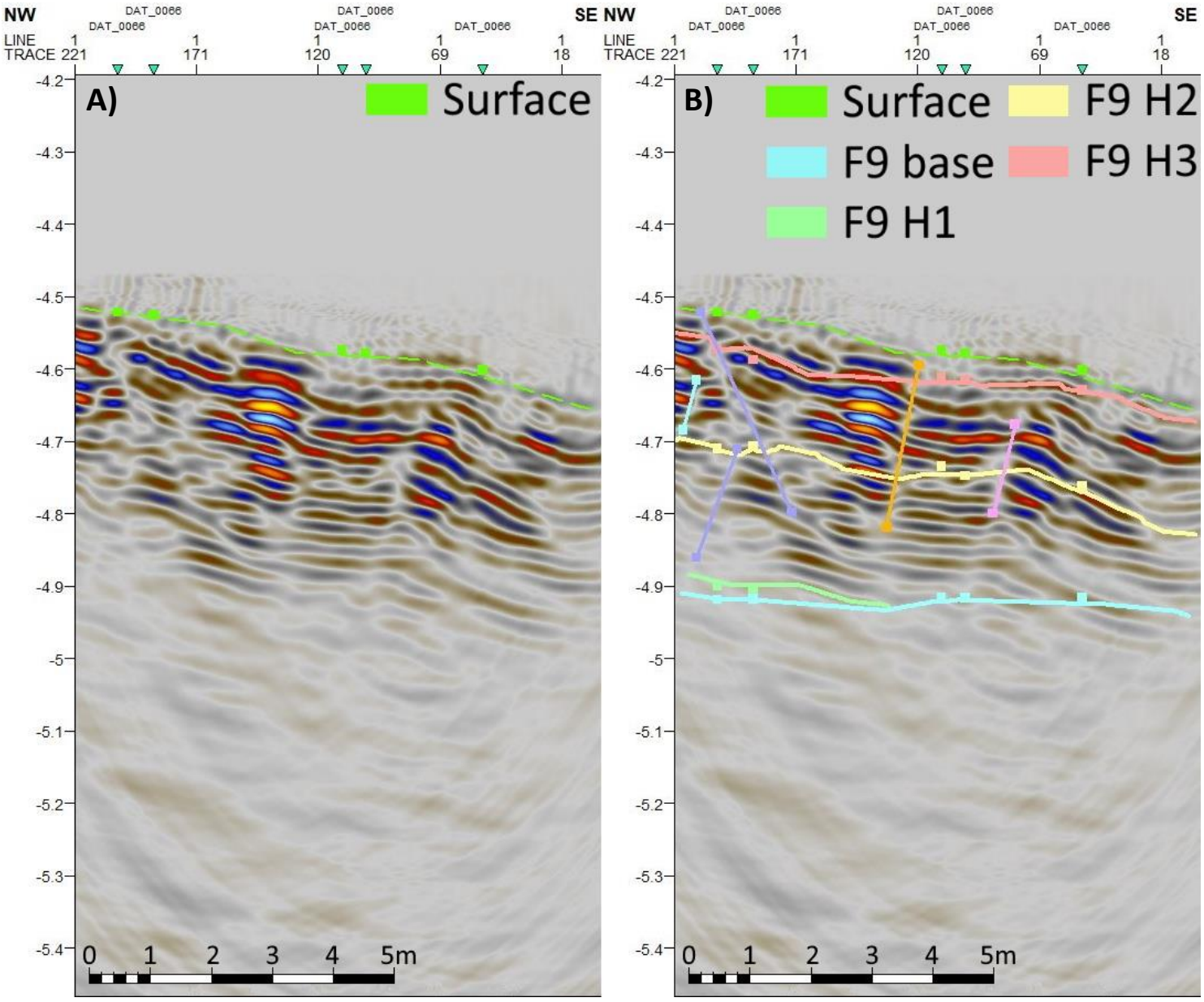

Figure 7.1: An example of offset interpretation in line DAT_0064 A) blank and B) with all interpretation.

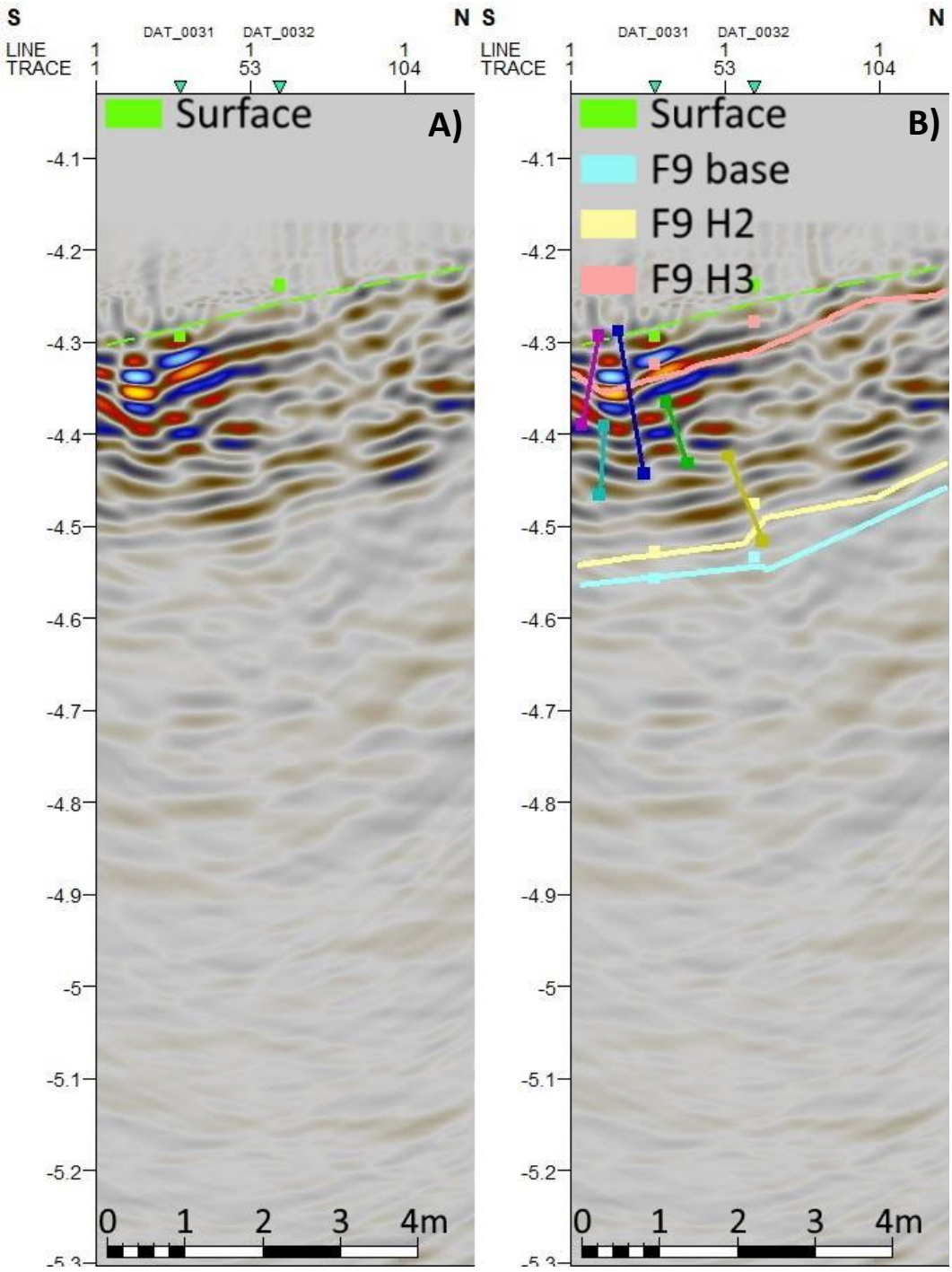

Figure 7.2: An example of offset interpretation in line DAT_0090 A) blank and B) with all interpretation.

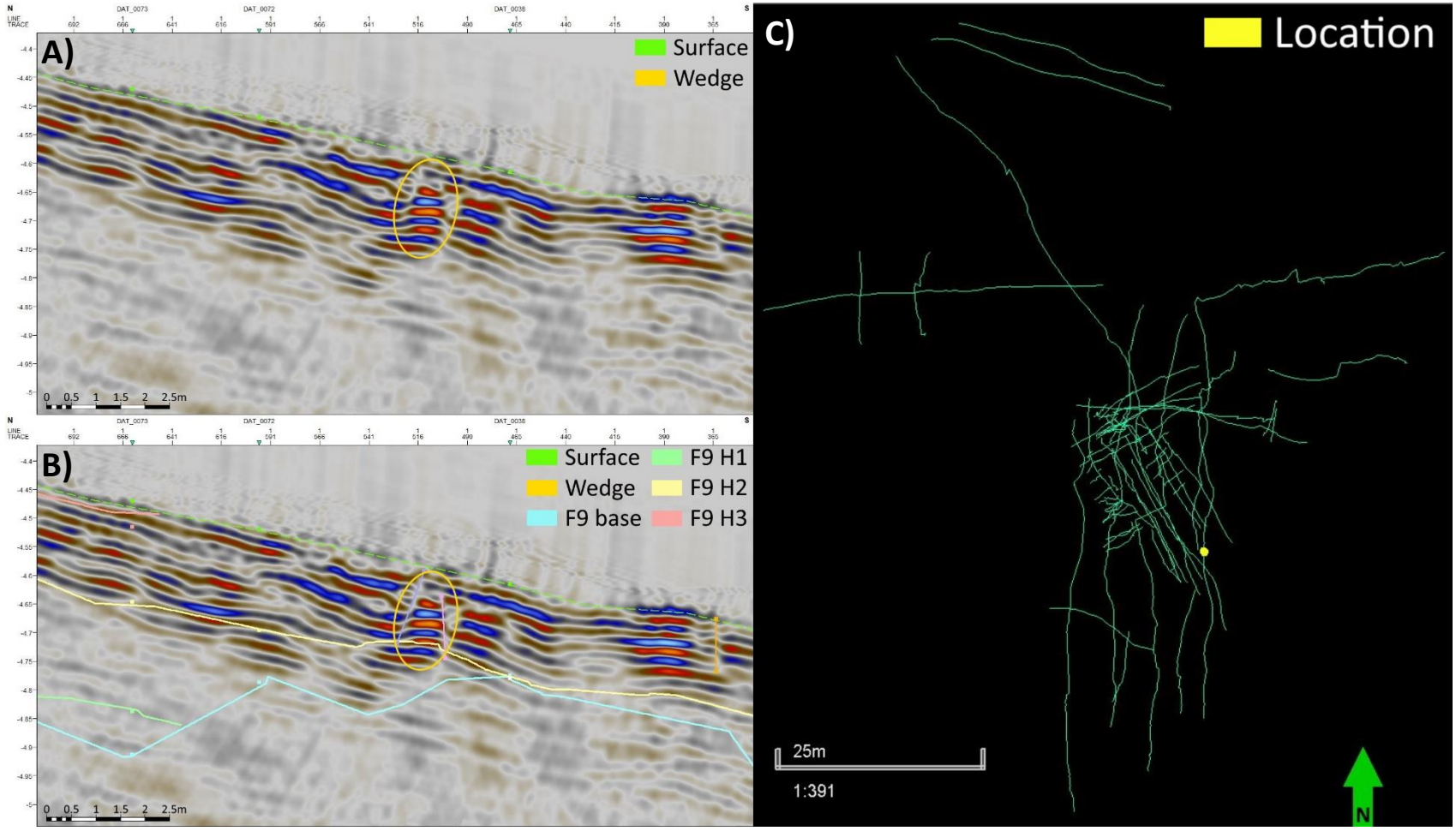

Figure 7.3: An example of a wedge in line DAT_0027. A) blank, B) interpreted, and C) location of the wedge.

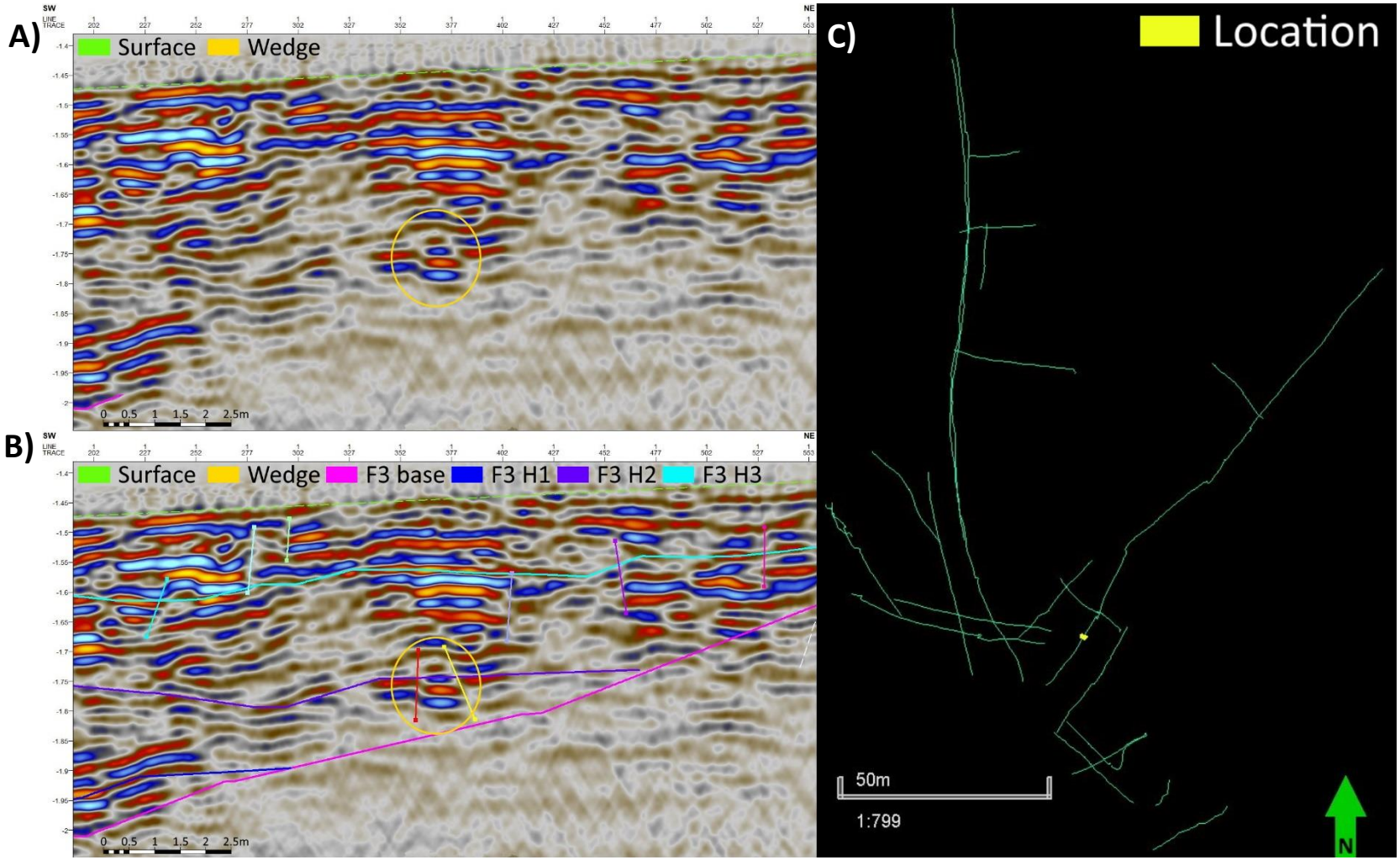

Figure 7.4: An example of a wedge in line DAT_0103. A) blank, B) interpreted, and C) the location of the wedge.

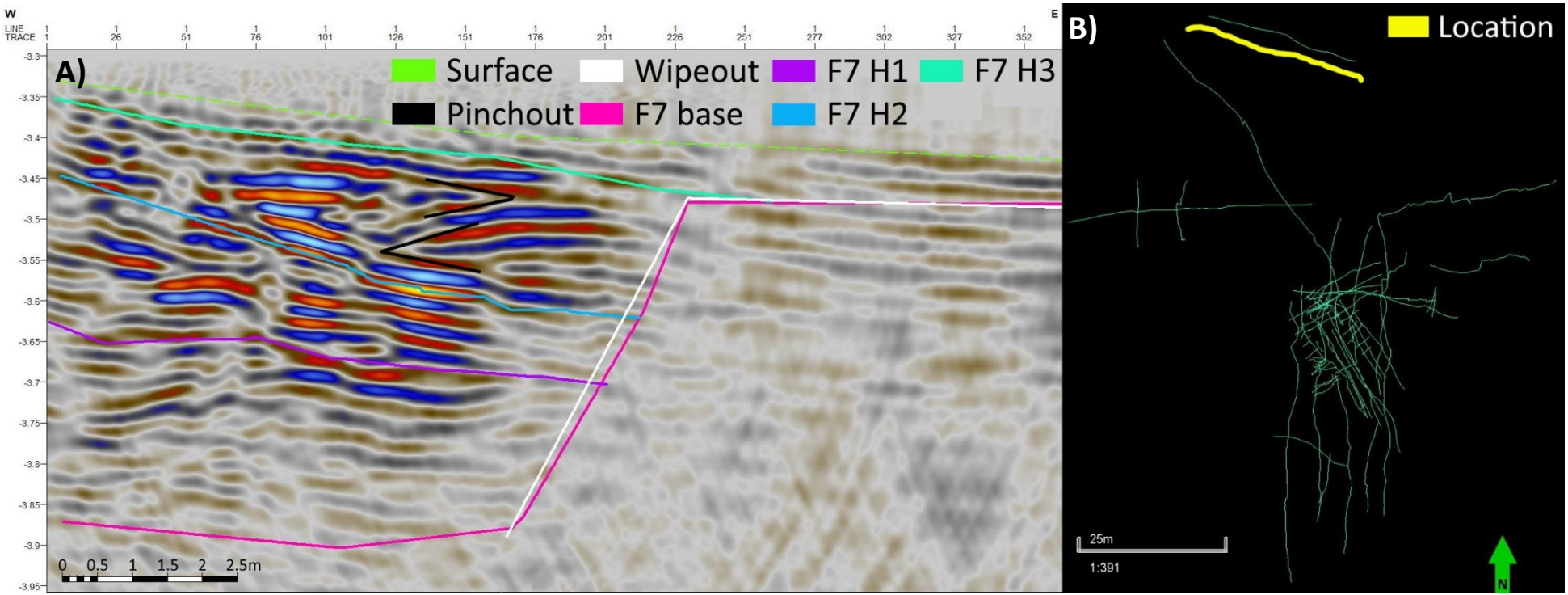

Figure 7.5: An example of two pinchouts in line DAT_0036. A) the pinchouts in black, B) the location of the line containing the pinchouts.

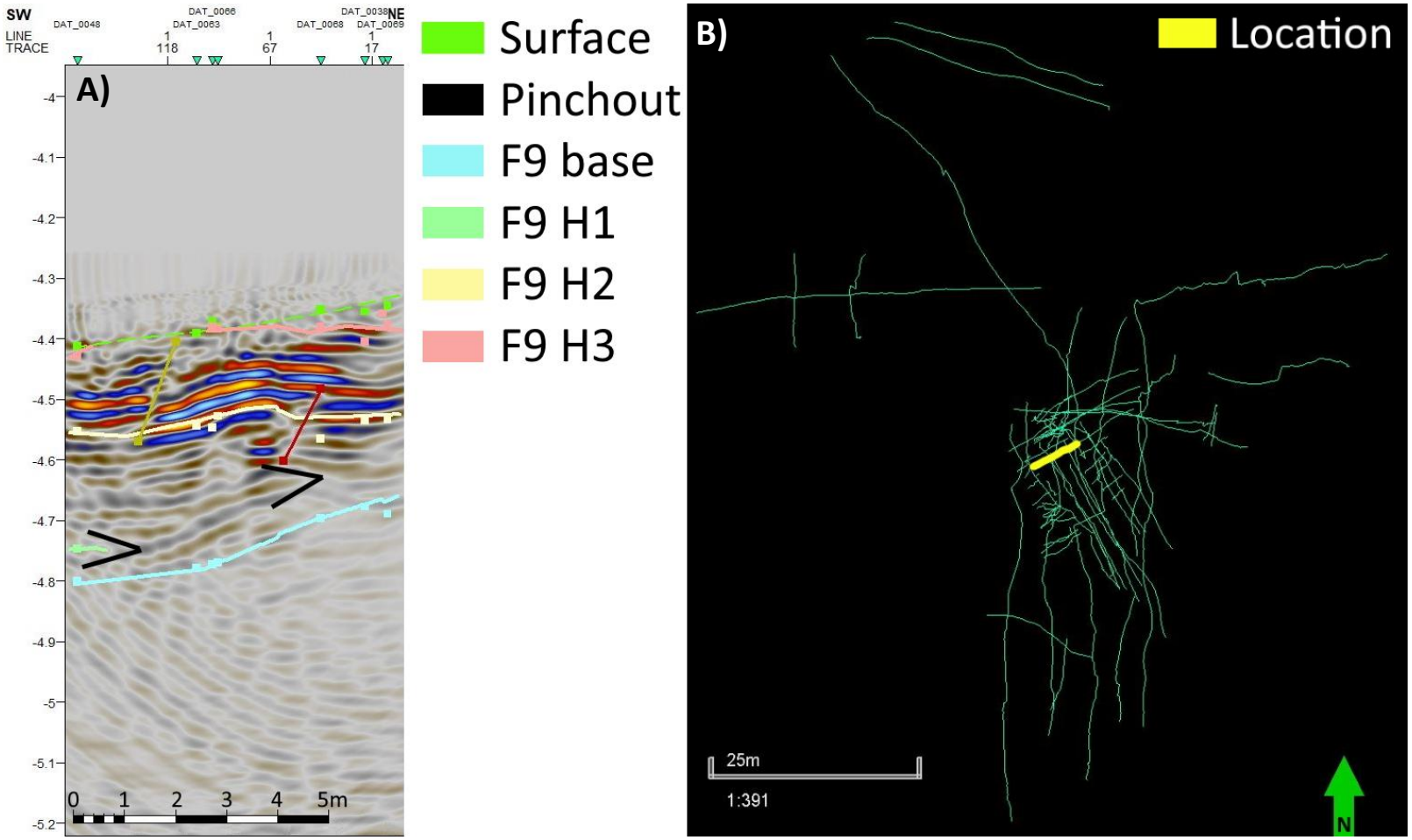

Figure 7.6: An example of two pinchouts in line DAT_0046. A) the pinchouts in black and B) the location of the line.

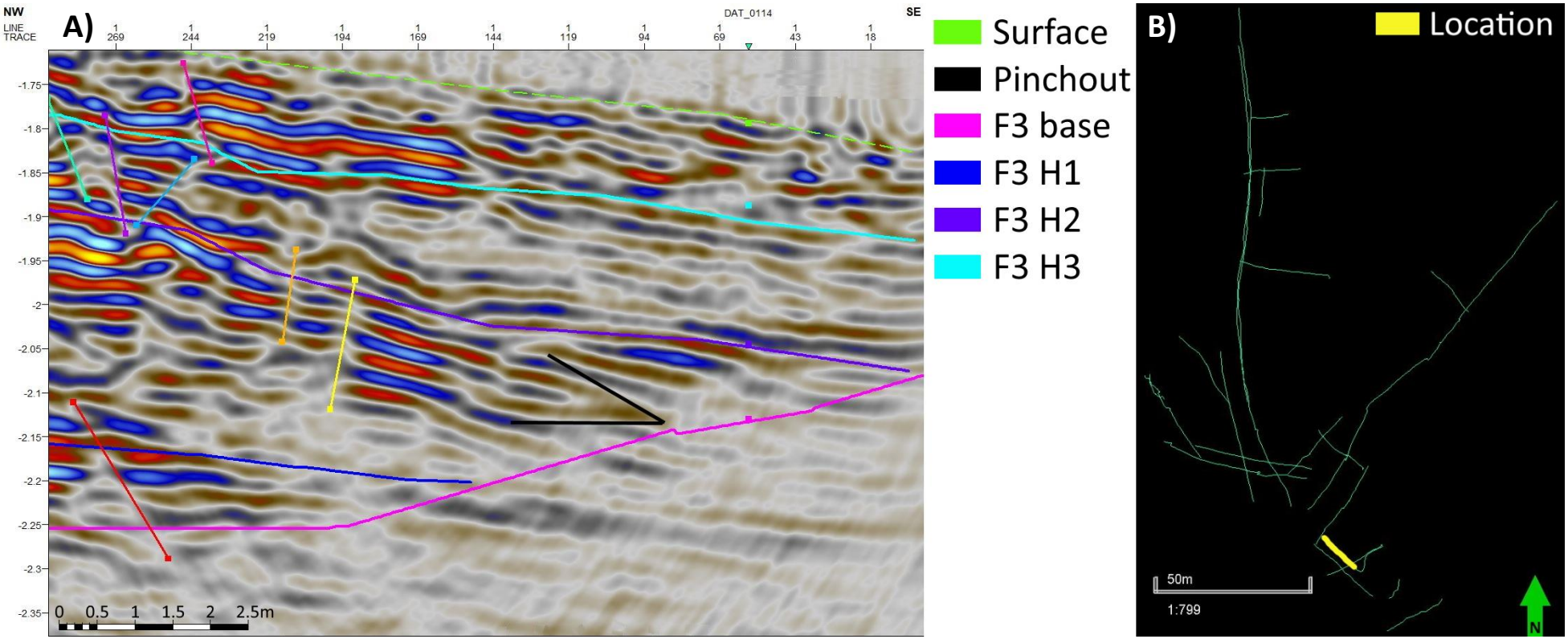

Figure 7.7: An example of a pinchout in line DAT_0115. A) the pinchout in black and B) the location of the line.

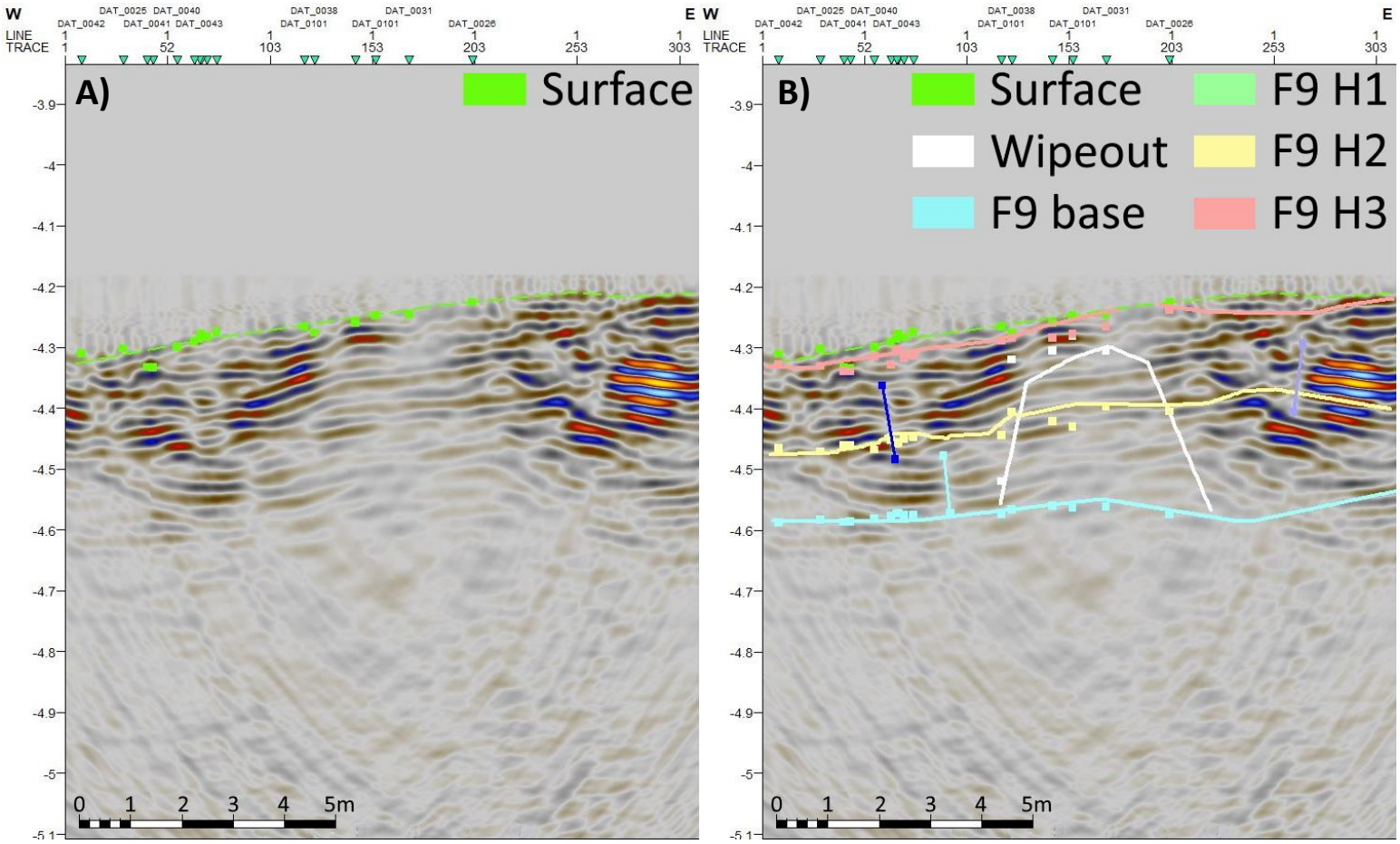

Figure 7.8: An example of wipeout interpretation in line DAT_0021. A) blank and B) the full interpretation.

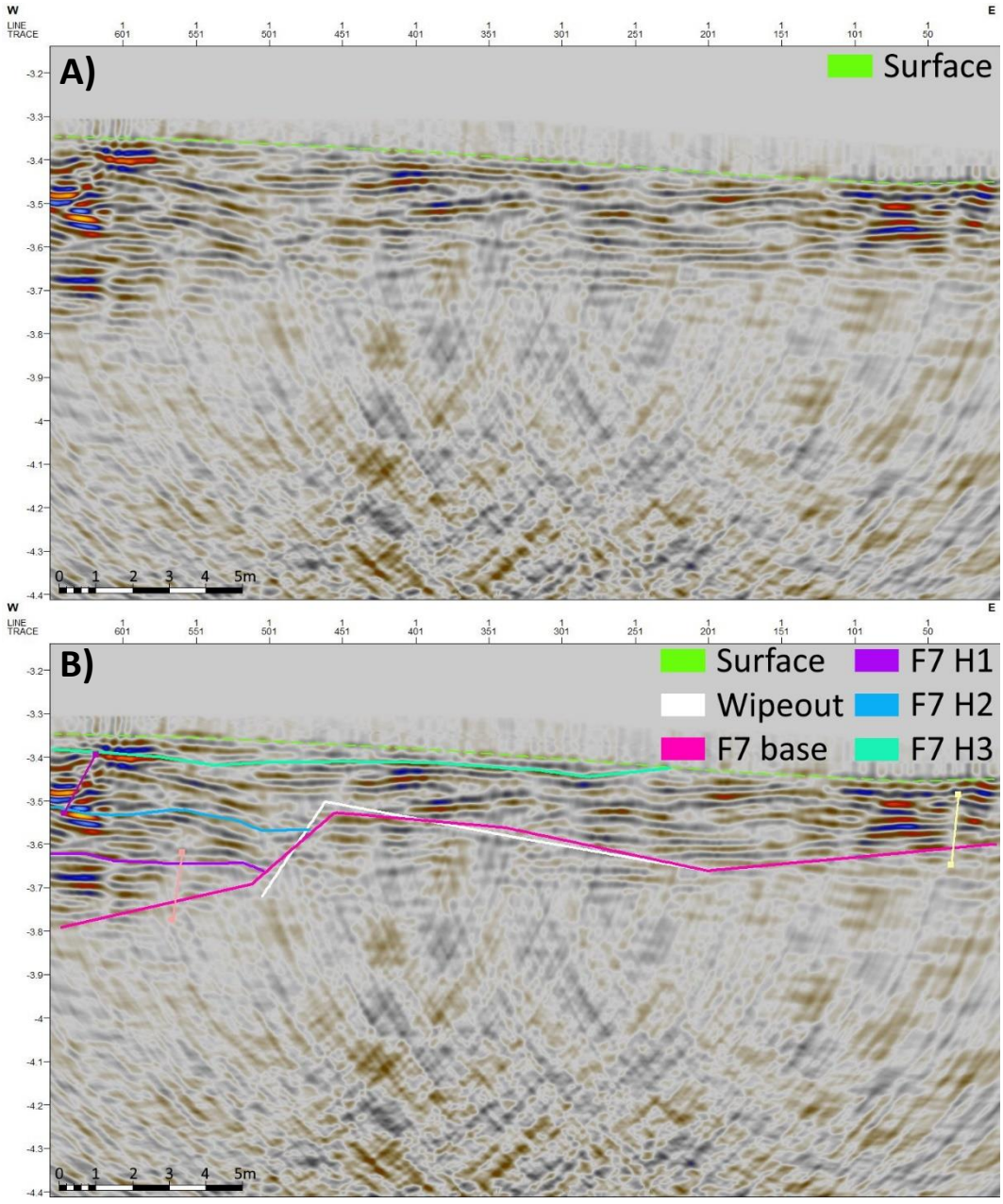

Figure 7.9: An example of wipeout interpretation in line DAT_0037. A) blank and B) the full interpretation.

Figure 7.10: Locations of lines in figures in Appendix 2, Upper Cemetery.

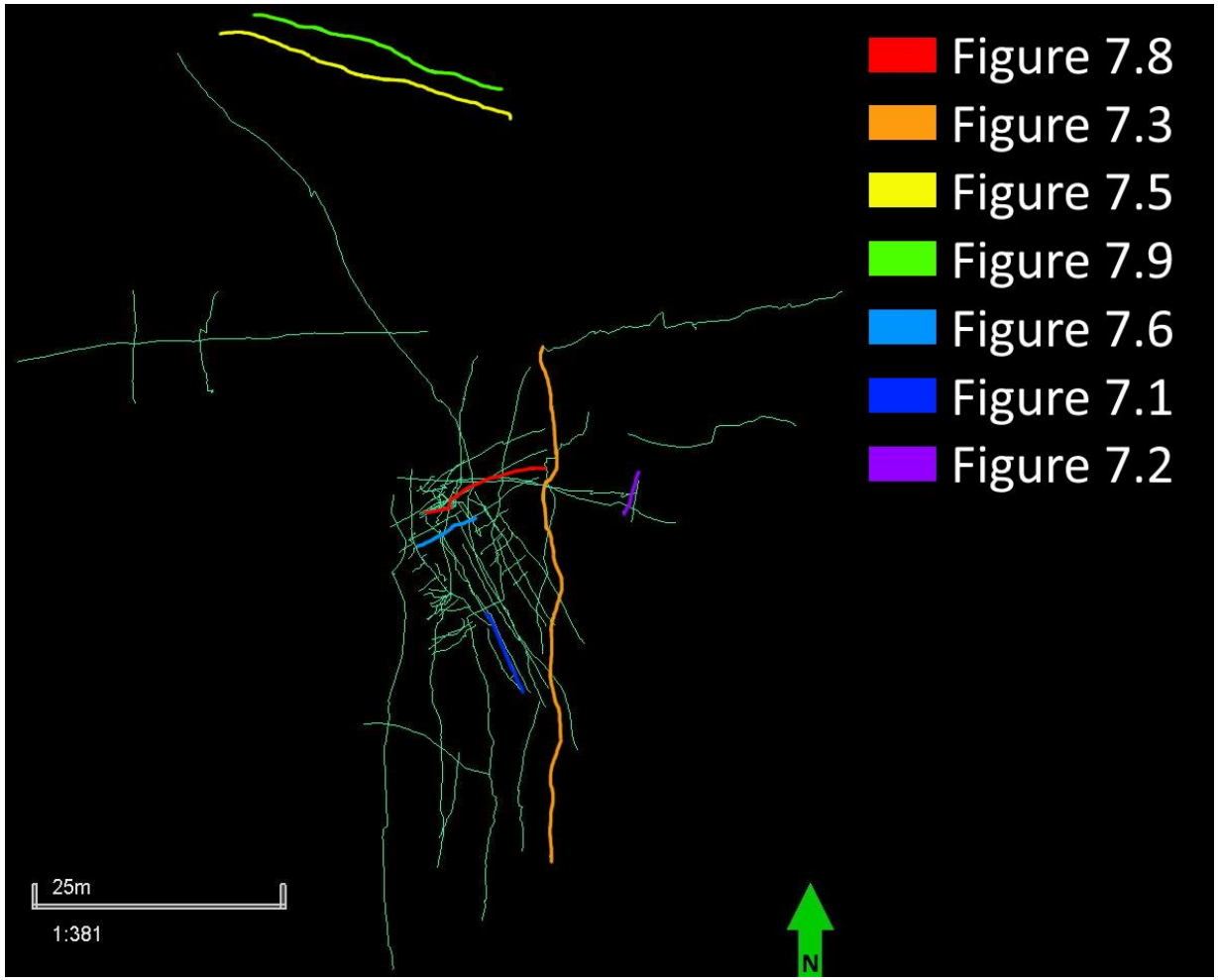

Figure 7.11: Locations of lines in figures in Appendix 2, Middle Cemetery.